

Copyright
by
Sophie Ann Goliber
2022

The Dissertation Committee for Sophie Ann Goliber
certifies that this is the approved version of the following dissertation:

**Controls on terminus change of marine terminating
glaciers in Greenland over the last 40+ years.**

Committee:

Ginny Catania, Supervisor

Timothy Goudge

Jamin Greenbaum

Patrick Heimbach

Kyle Spikes

**Controls on terminus change of marine terminating
glaciers in Greenland over the last 40+ years.**

by

Sophie Ann Goliber

DISSERTATION

Presented to the Faculty of the Graduate School of
The University of Texas at Austin
in Partial Fulfillment
of the Requirements
for the Degree of

DOCTOR OF PHILOSOPHY

THE UNIVERSITY OF TEXAS AT AUSTIN

December 2022

For Mom, Dad, Josh, Caroline, Joey, Kelly, and Bradley.

Acknowledgments

This dissertation would not exist if not for the people who helped me along the way. I have always said that science is not done in a bubble, and this is especially true for my time at the University of Texas.

First and foremost, I would like to thank my advisor, Ginny Catania. Through her mentoring, I have learned not only to be a better scientist and writer, but a better person. She has shown me how to actively make the community that surrounds me a better place, to be a compassionate and strong leader, and to stand my ground when faced with adversity. I look forward to changing the field of glaciology with her in the future. I also would like to thank my committee members, Timothy Goudge, Jamin Greenbaum, Patrick Heimbach, and Kyle Spikes, for their valuable time and energy in making my education at UT a success, as well as my collaborators Taryn Black, James Lea, Daniel Cheng, and Helene Olsen. I have had the pleasure of learning from amazing people in the realm of diversity, equity, and inclusion both in and outside of UT, including Dana Thomas, Leah Turner, and members of the CryoCommunity team. Thank you to my group mates Denis Felikson, Mason Fried, Evan Carnahan, Matthew Zeh, John Christian, Enze Zhang, Kevin Shionalyn, and the many undergraduates who have joined through the years.

Thank you to my dear and amazing graduate school friends (many of whom I lived with at one point or another in the dinky Chicon St. house), Jenny Harding, Stephen Ferenz, Evan Ramos, Chelsea Mackaman-Lofland, Sam Robbins, Scott Eckley, Grace Beaudoin, Kat and Bruce Wilson, Kelly Olsen, Grace Guyran, Tyler Meng, and Brandon Tober. There are so many more of you who made my life amazing while in Austin! Hope Miedema, Julia Zitzmann, Rachel O'Connor, Haley Parker, and Johanna Wiley- you guys were there long before graduate school and I know you will be here long after. Thanks for always being just one decade-long group chat away.

I would like to thank my parents, Michael Goliber and Cynthia Garlan, who fostered my love of the Earth and curiosity when I was very young. Thank you for supporting me through all these many years of school. Josh, Caroline, Joey, and Kelly- you guys will never know how much you mean to me- having siblings is my greatest achievement that I had nothing to do with and I am so proud to be your sister! Finally, my love, Bradley Post. I truly would not be here without your support and I can't wait to be your cheerleader next!

Controls on terminus change of marine terminating glaciers in Greenland over the last 40+ years.

Publication No. _____

Sophie Ann Goliber, Ph.D.

The University of Texas at Austin, 2022

Supervisor: Ginny Catania

Since the 1980s, the Greenland ice sheet has been losing ice mass at an increased rate. Our current understanding of the complex physical processes that control dynamic mass loss is incomplete and, therefore, leads to a wide range of possible future contributions to sea level. Ice dynamics, or changes due to changes in ice flux, is dominated by the behavior of fast-moving outlet glaciers in Greenland. These glaciers are changing through melting of the terminus face and/or calving of icebergs; the combination of these processes and ice motion determines the position of a glacier terminus. In understanding how and why outlet glacier termini change over time compared to external forcing and internal glacier dynamics, we are able to move toward a better understanding of marine-terminating glaciers. In this dissertation, I use terminus traces to observe how and why marine-terminating glaciers change in order to better understand the mechanisms behind these complex heterogeneous changes in Greenland. I develop the largest database of manually-traced

marine-terminating glacier terminus data for use in scientific and machine learning applications. These data have been collected, cleaned, assigned with appropriate metadata, including image scenes, and compiled so that they can be easily accessed by scientists. Then I use the location of the termini to identify features in the bed topography that inhibit the retreat of glaciers following the onset of ocean warming and widespread glacier retreat in the late 1990s. I find that the slope and lateral dimensions of bed features exhibit the strongest correlation to retreat and that the shape of the bed features allows different styles of terminus retreat, which may be indicative of how different ablation mechanisms are distributed across termini. Finally, I produce a time series of terminus morphological properties for four glaciers in western Greenland to identify the characteristics that are indicative of calving processes with the goal of categorizing glaciers by calving style. I find that a concave shape and low sinuosity are present at glaciers that calve via buoyant flexure, while the opposite is true at glaciers that are dominated by melt-induced calving via serac failure. I also find that glaciers do not persistently fit into single calving styles and may change over time. By studying how the terminus changes over time compared to external forcing and internal glacier dynamics, we are able to move toward a better understanding of marine-terminating glaciers.

Table of Contents

Acknowledgments	v
Abstract	vii
List of Tables	xii
List of Figures	xv
Chapter 1. Introduction	1
Chapter 2. TermPicks: A century of Greenland glacier terminus data for use in scientific and machine learning applications	11
2.1 Introduction	12
2.2 Methods	15
2.2.1 Input data	15
2.2.2 Glacier identification	17
2.2.3 Data cleaning	18
2.2.4 Metadata creation	19
2.2.5 Landsat image scene identifiers	22
2.2.6 Calculation of terminus change and variability	23
2.2.7 Error Estimation	25
2.3 Results	26
2.3.1 Terminus change and variability	27
2.3.2 Spatial and temporal bias	28
2.3.3 Error in manual digitization	30
2.4 Discussion	32
2.5 Conclusions	36
2.6 Supplemental Materials	54

Chapter 3. Bed topographic controls on heterogeneous terminus dynamics in Greenland	58
3.1 Introduction	59
3.2 Methods	62
3.2.1 Identifying Glaciers with Adequate Data	63
3.2.2 Glacier Properties	66
3.2.3 Identifying Standstills	67
3.2.4 Bed Morphology at Standstills	68
3.2.5 Characterizing Standstill Features	70
3.3 Results	73
3.3.1 Glacier and Fjord Characteristics	73
3.3.2 Bed Morphology at Standstills	74
3.3.3 Terminus Behavior at Standstills	75
3.3.4 Bed Feature Properties at Standstills	77
3.4 Discussion	79
3.5 Conclusions	84
3.6 Supplemental Materials	99
Chapter 4. Using the map-view terminus morphology to deduce ice-ocean processes	108
4.1 Introduction	109
4.2 Methods	112
4.2.1 Glaciers	113
4.2.2 Terminus Data	115
4.2.3 Terminus Morphology	116
4.2.4 Height above Buoyancy	117
4.2.5 Subglacial Hydrology	118
4.2.6 Submarine terminus melt	119
4.2.7 Cluster Analysis	120
4.3 Results	122
4.3.1 Terminus Flotation	122
4.3.2 Submarine Melt and Hydrology at Termini	123
4.3.3 Terminus Seasonality	123

4.3.4	Sinuosity	124
4.3.5	Convex Hull Area	125
4.3.6	Cluster analyses	126
4.3.7	Application to other glaciers	127
4.4	Discussion	128
4.4.1	Correlation between terminus processes and morphology	128
4.4.2	Calving Style Exceptions	130
4.4.3	Extending our Classification to Other Glaciers	132
4.4.4	Shortcomings and Future Directions	134
4.5	Conclusions	135
4.6	Supplemental Materials	153
Chapter 5. Conclusions		165
Vita		200

List of Tables

2.1	Original sources for terminus traces for the TermPicks data set. Spatial coverage describes the number of glaciers and name/region(s) of the traces. Date range are the years covered by the data set. Resolution is the temporal resolution; Annual is approximately one trace per year, sub-annual is more than one trace per year, decadal is approximately one trace every ten years, sub-decadal is more than one trace every 10 years, but not each year. Method is the tracing method used by the author to digitize the terminus. The Author key is the label given to that data set in the TermPicks data set.	51
2.2	Image sources used in this compilation of manually-traced glacier terminus trace dataset.	52
2.3	Flags assigned to output terminus trace data, created in conjunction with CALFIN (<i>Cheng et al., 2020</i>). All data in the TermPicks dataset has the prefix of X = 0.	53
2.4	Mean vertices per kilometer of trace, and mean and median of the median errors of each author compared to other authors. .	53
3.1	Glaciers with standstills defined as 'transient' for this study. Retreat estimates are the difference between 1985-2019 terminus positions derived from TermPicks and CALFIN datasets. Mean ice discharge, thickness, and velocity estimates between 2000-2019 are derived from King et al. 2020. The H_{ab} values are median values from within ~ 2 km of the terminus of the AeroDEM in 1985.	86
3.2	Glaciers with standstills defined as "persistent" for this study. Retreat estimates are the difference between the 1985-2019 terminus positions derived from the TermPicks and CALFIN datasets. Mean ice discharge, thickness, and velocity estimates between 2000-2019 are derived from King et al. (2020). The H_{ab} values are median values within ~ 2 km of the AeroDEM terminus in 1985.	87
3.3	Results of the Welch's T tests comparing the mean values of the measurements of transient and persistent standstill features.	87
3.4	Results of the Welch's T tests comparing the mean values of the measurements of transient and restablizing standstill features.	88

3.5	Summary of the mode types for transient and persistent stand-stills corresponding to the modes shown in Fig. 3.3. Mode 1) termini remain primarily on the retrograde side; Mode 2) termini remain primarily on the prograde side or; Mode 3) termini oscillate between retrograde and prograde sides of the bed peak.	88
3.6	Classification of glaciers by coverage 1-4 (determined from <i>Morlighem et al. (2017)</i>), terminus traces per year, retreat pattern, and exceptions for this study.	107
4.1	Statistics for terminus change, seasonality, H_{ab} for bulk, pre- and post-retreat time epochs for the glaciers in this study. * indicates that only one digital elevation model was available for that period of time.	136
4.2	Statistics for sinuosity, convex hull area, and submerged area for bulk, pre- and post-retreat time epochs for the glaciers in this study.	136
4.3	The TermPicks glacier ID, name abbreviation, and timing of the onset of retreat from <i>Catania et al. (2018)</i> seasonality values for the additional twelve glaciers in this study. See Figure 4.1 for the locations of each glacier.	137
4.4	Statistics for clusters 0 and 1 for the analysis of clusters from the H_{ab} , q_m and seasonality k-means cluster analysis. Cluster means are the mean values for the convex hull area and the sinuosity for all three cluster analyses. These values are used in figure 4.14.	138
4.5	DEMs used for the calculation of H_{ab} for RNK glacier. The median H_{ab} is the median of all values in the stress-coupling length defined by the terminus of the glacier in the DEM. The STD is the standard deviation of the values of H_{ab} within the stress-coupling length. The mean bed error is the mean of all error values defined in the error map of BedMachineV4 (<i>Morlighem et al., 2017</i>) within the stress-coupling length.	162
4.6	DEMs used for the calculation of H_{ab} for STR glacier. The median H_{ab} is the median of all values in the stress-coupling length defined by the terminus of the glacier in the DEM. The STD is the standard deviation of the values of H_{ab} within the stress-coupling length. The mean bed error is the mean of all error values defined in the error map of BedMachineV4 (<i>Morlighem et al., 2017</i>) within the stress-coupling length.	163

4.7	DEMs used for the calculation of H_{ab} for SIL glacier. The median H_{ab} is the median of all values in the stress-coupling length defined by the terminus of the glacier in the DEM. The STD is the standard deviation of the values of H_{ab} within the stress-coupling length. The mean bed error is the mean of all error values defined in the error map of BedMachineV4 (<i>Morlighem et al., 2017</i>) within the stress-coupling length	164
4.8	DEMs used for the calculation of H_{ab} for KAS glacier. The median H_{ab} is the median of all values in the stress-coupling length defined by the terminus of the glacier in the DEM. The STD is the standard deviation of the values of H_{ab} within the stress-coupling length. The mean bed error is the mean of all error values defined in the error map of BedMachineV4 (<i>Morlighem et al., 2017</i>) within the stress-coupling length.	164

List of Figures

1.1	Schematic of ice-ocean processes that impact marine-terminating glaciers. The colored water bodies indicate the locations of stratified ocean water found in Greenland fjords. Blue and orange arrows indicate heat exchanges as a result of both warm ocean waters and subglacial water entraining warm water in plumes.	9
1.2	Optical satellites commonly used in studies of Greenland. The bars with an arrow at the end are satellites that are currently collecting data. The satellites in this figure are listed in <i>Goliber et al. (2022)</i>	10
2.1	Flow chart showing processing pipeline for producing consistent terminus trace training data.	38
2.2	Common issues addressed in data cleaning and labeling. a) Box method glacier traces are contained within a box that is smaller than the full terminus width at Glacier 224 b) Landsat 7 ETM+ Scan Line Corrector-off image line artifacts at Glacier 291 and c) A single shapefile containing several different glaciers (IDs 27-30) that need to be split manually into separate glaciers to be consistent with the ID scheme. Additionally, all 3 images show varied levels of obstruction of the terminus in the fjord due to ice mlange. Landsat-7 and Landsat-8 images courtesy of the U.S. Geological Survey.	39
2.3	Example metadata for the TermPicks data set. Each column corresponds to the description in Section 2.4 (Metadata Creation).	40

2.4	A) Terminus trace count for glaciers in Greenland. Each circle is centered on a location of a glacier in the TermPicks ID file. The size of the circle reflects the total number of terminus traces available for that glacier. B) The same data organized by drainage basin. Circle size reflects the total number of traces for that basin. The numbers inside or adjacent to the circle represent the number of individual glaciers in each basin with terminus traces. Each basin is defined by the ESA/NASA ice sheet mass balance inter-comparison exercise 2016 (IMBIE; <i>Shepherd et al.</i>) which includes basins from <i>Rignot and Mouginot (2012)</i> and <i>Rignot et al. (2011)</i> . They are labeled by their geographic location. Region labels are NO = North, NE = North East, SE = South East, SW = South West, CW = Center West, NW = North West.	41
2.5	Heatmap of glacier traces in each regional basin from ESA/NASA ice sheet mass balance inter-comparison exercise 2016 (IMBIE; <i>Shepherd et al.</i>) in this study. Total number of traces per region can be found in Figure 2.4. The x-axis is year and the y-axis is the Basin ID. The color corresponds to the number of traces for that basin's glacier per year. 0 traces are grey.	42
2.6	Terminus positions for Glacier 152 (Kangerlussuaq Gletsjer) from 2006-08-11 for 3 authors. Bunce (pink) and Cheng (blue) traces end before the northern fjord wall while the ESA (yellow) trace ends at the northern wall. The table shows each calculated retreat amount since the 1978 position using the Interpolation method and the Centerline method. Landsat-7 image courtesy of the U.S. Geological Survey. Base image has reduced saturation to increase contrast with traces.	43
2.7	Decadal retreat patterns for available TermPicks data using the Centerline method. For each panel, the entire decade of traces were averaged to produce an average position for that decade. The 1940/1950s are an average over both decades as there are fewer traces available in the 1950s. Then the average position for the decade is differenced from average position of the previous decade. The size correlates to magnitude of terminus change, while red (negative) indicates retreat and blue (positive) indicates advance.	44
2.8	Locations of glaciers that include terminus delineations for at least three unique months, which is the minimum number of traces required to resolve seasonality, for the entire TermPicks data set and a subset of authors. The size of the blue circle indicates how many years there are enough traces to resolve seasonality, ranging between a single year to up to 40 years. .	45

2.9	Example seasonality plots for three glaciers, F. Graae Gletscher(116), Heinkel Gletsjer (109), and Humboldt Gletsjer (85). The location of each of these glaciers is noted in Figure 2.8. Each color corresponds to either the entire TermPicks data set (purple) or an individual author. Glacier 85 has no individual author data set that can resolve the seasonality.	46
2.10	A: Terminus change between 1990-2020 colored by sinuosity for Glacier 288 (Sermeq Silarleq). The dashed grey line is the start of progressive retreat as defined in <i>Catania et al.</i> (2018). B: Corresponding map-view terminus traces For Glacier 288 with every 5th trace colored by sinuosity. C: Terminus change between 1990-2020 colored by sinuosity for Glacier 291. D: Corresponding map-view terminus traces for Glacier 291 (Kangerdlugssup Sermerssua) with every 5th trace colored by sinuosity. The base map in B and D is the bed from BedMachine (<i>Morlighem et al.</i> , 2017). The black pixels in B are errors, however they do not impact the overall interpretation of the bed. The bed scalebar applies to both B and D. The white arrows indicate glacier flow direction. The red star on the inset map is the location of the glacier on the Greenland Ice Sheet.	47
2.11	Examples of Landsat image availability (gray) versus termini traced (orange) for (a) Kangilliup Sermia (Rink Isbræ; 1), a relatively well-traced glacier, (b) Qeqertaarsuusarsuup Sermia (Tracy Gletsjer; 73), a glacier representative of the average number of total traces for this dataset, (c) Sermeq Silarleq (288), the glacier with the highest percentage of available Landsat images that have been traced in this dataset, and (d) an unnamed glacier (251), representative of the average percentage of available Landsat images that have been traced in this dataset. . .	48
2.12	Median error between pairs of authors, for instances where those authors have duplicated a glacier trace on a given date. No color indicates two authors have no duplicated traces between them.	49
2.13	Example terminus change for Glacier 116 (F. Graae Gletscher). Color and symbol correspond to different authors for each pick.	50
2.14	Heatmap of glacier traces for glaciers 1 to 102. The x-axis is year and the y-axis is the Glacier ID. The color corresponds to the number of traces for that basin's glacier per year, between 1 and $\sqrt{25}$. 0 traces are grey.	55
2.15	Heatmap of glacier traces for glaciers 103 to 205. The x-axis is year and the y-axis is the Glacier ID. The color corresponds to the number of traces for that basin's glacier per year, between 1 and $\sqrt{25}$. 0 traces are grey.	56

2.16	Heatmap of glacier traces for glaciers 206 to 291. The x-axis is year and the y-axis is the Glacier ID. The color corresponds to the number of traces for that basin's glacier per year, between 1 and 25. 0 traces are grey.	57
3.1	A, D, G: Terminus traces colorized by retreat (red dashed line), standstills (blue dashed line) for Glacier 2, 7, and 229. Black dashed lines indicate times when there was not enough data to define a retreat or standstill. The solid black line delineates the standstill feature. B,E,H: Directional slope for each glacier. The solid black line delineates the standstill feature (same as A, D, G) The green circle is the location of the bed peak, and the green line is the location of the split between the prograde and retrograde slope defined by the 0-slope contour. C,F,I: The solid black line delineates the standstill feature (same as A, D, G). The blue lines correspond to the transects shown in Fig. 3.2. The base map for all figures labeled A, C, D, F, G, H, I is BedMachine V4.	89
3.2	Bed features along and across the fjord transects for Glaciers 2, 7, and 229 to demonstrate the different types of features identified. Each transect corresponds to the same location as noted in figures 3.1 B, E, H. The vertical lines in the figures on the right are every fifth terminus colorized by standstill(blue) or active retreat (red). The green dot corresponds to the apex location.	90
3.3	Examples of the distance between the terminus (centroid) and the peak of the bed feature compared to the mean directional slope at the terminus for six glaciers. When the centroid distance is negative (orange), the centroid is on the down-glacier side of the peak. When the centroid distance is positive (purple), the centroid is located on the up-glacier side of the peak. The slope is saturated at -10 and 10 to compare the figures.	91
3.4	Overview of the locations of the standstill features defined in this study. Each map corresponds to the locations of the transient, persistent, and restabilizing standstill features. The pie chart is the distribution of types for the transient and persistent standstill features in this study. The numbers that offshoot from the maps are locations of some glaciers noted in the text.	92
3.5	Ice discharge, thickness, and median height above buoyancy (H_{ab}) for glaciers with transient and persistent standstills in this study. Ice discharge and thickness data are from <i>King et al.</i> (2020). The H_{ab} is derived from AeroDEM (<i>Korsgaard et al.</i> , 2016) and BedMachineV4 (<i>Morlighem et al.</i> , 2017). The t-test values are also reported in Table 3.3	93

3.6	Top: Distribution of the lithology by transient and stabilizing standstill features and feature type. Bottom: Distribution of the presence of contact at features by transient and stabilizing standstill features and feature type	94
3.7	Overview of the distribution of the type of feature and mean slopes for the transient, stabilizing, and restabilizing standstill features. Pie charts correspond to the distribution of feature types, whereas box plots show the mean prograde and retrograde slopes for each type. The black dots in the box plots are the raw data used to produce the plots.	95
3.8	The mean distance from the terminus centroid to the peak of a bed feature for different standstill types. For transient standstills, this is the mean distance from the peak before the onset of retreat. For persistent standstills, this is the mean distance over the study period.	96
3.9	Left: Distribution of feature types according to the presence of swinging door retreat. Right: Examples of swinging door retreat at glacier #65 and non-swinging door retreat at glacier #3.	97
3.10	Box plots comparing transient, stabilizing, and restabilizing standstill features. The black dots in the plot are the raw data used to produce the plots.	98
4.1	Locations of the four glaciers used in this study to develop morphological relationships (colors). Teal colored basins correspond to the basins used to determine runoff from <i>Mankoff et al.</i> (2020a). Locations of the supplemental glaciers (white) used to test the proxy developed in this study.	139
4.2	Examples of how piece-wise sinuosity and convexity are calculated. a) We compute piece-wise sinuosity for each terminus (red dashed lines) along 1 km segments and then take the mean of all of these to get mean sinuosity. b) Convex hull area is computed to identify termini that are either convex (green) or concave (purple).	140
4.3	Map-view of both a selected PGC digital elevation model and the AeroDEM in 1985 for RNK. Left are hillshade with 4x vertical exaggeration with elevation data overlain and the right is the H_{ab} for the corresponding digital elevation model. The pink arrow points to the location of the flexure zones. The mapped plume locations are represented by the blue heat maps located on the terminus.	141

4.4	Map-view of both a selected PGC digital elevation model and the AeroDEM in 1985 for KAS. Left are hillshade with 4x vertical exaggeration with elevation data overlain and the right is the H_{ab} for the corresponding digital elevation model. The mapped plume locations are represented by the blue heat maps located on the terminus.	142
4.5	Map-view of both a selected PGC digital elevation model and the AeroDEM in 1985 for STR. Left are hillshade with 4x vertical exaggeration with elevation data overlain and the right is the H_{ab} for the corresponding digital elevation model. The mapped plume locations are represented by the blue heat maps located on the terminus.	143
4.6	Map-view of both a selected PGC digital elevation model and the AeroDEM in 1985 for SIL. Left are hillshade with 4x vertical exaggeration and the right is the H_{ab} for the corresponding digital elevation model. The pink arrow points to the location of the flexure zone in 2014. The mapped plume locations are represented by the blue heat maps located on the terminus. . .	144
4.7	Map-view changes in sinuosity for every summertime terminus pick colored by piece-wise sinuosity for glaciers A) RNK, B) SIL, C) STR, and D) KAS. Blue heat maps on the terminus are occurrences of sediment plumes that have breached the surface between 1985-2021. The blue lines on the bed data below the terminus traces is the estimated locations of subglacial channels calculated using the hydraulic potential. The bed is BedMachineV4.	145
4.8	Seasonality (red lines) compared to terminus change (black line), parameterized submarine melting (teal line), height above buoyancy (H_{ab} ; blue line) for the four main glaciers used in this study. The H_{ab} value of 50 m reflects the local ellipsoid height. Thus, values above 50 m are interpreted as grounded and values below 50 m are interpreted as floating. Seasonality values for each year are given in red. For glaciers with a retreating terminus, we delineate the onset of retreat (black vertical dashed lines) and an acceleration in retreat for SIL (gray vertical dashed line).	146

4.9	Sinuosity (orange lines/dots) compared to terminus change (black line) parameterized submarine melting (teal line), height above buoyancy (H_{ab} ; blue dots/line) for the four main glaciers used in this study. The H_{ab} value of 50 m reflects the local ellipsoid height. Thus, values above 50 m are interpreted as grounded and values below 50 m are interpreted as floating. Sinuosity values for each terminus trace are given as orange dots and the long-term smoothed sinuosity is provided as the solid orange line. Values closer to/further from 1 represent smooth/crenulated terminus morphologies. For glaciers with a retreating terminus, we delineate the onset of retreat (black vertical dashed lines) and an acceleration in retreat for SIL (gray vertical dashed line).	147
4.10	Convex hull area (green lines/dots) compared to terminus change (black line), parameterized submarine melting (teal line), height above buoyancy (H_{ab} ; blue line) for the four main glaciers used in this study. The H_{ab} value of 50 m reflects the local ellipsoid height. Thus, values above 50 m are interpreted as grounded and values below 50 m are interpreted as floating. convex values for each terminus trace are given as green dots and the long-term smoothed convex is provided as the solid green line. Positive/negative convex values represent convex/concave terminus morphologies. For glaciers with a retreating terminus, we delineate the onset of retreat (black vertical dashed lines) and an acceleration in retreat for SIL (gray vertical dashed line).	148
4.11	Top: 3D Results from the k-means clustering analysis for H_{ab} , convex hull area, and sinuosity. Top Left: Data points colored by assigned clusters 0 and 1. Top right: Data points colored by Glacier. Middle: Convex hull area and sinuosity vs. H_{ab} colored by clusters assigned from 3D cluster analysis. Bottom: Terminus change over time colored by assigned cluster for each glacier used in this study.	149
4.12	Top: 3D Results from the k-means clustering analysis for q_m , convex hull area, and sinuosity. Top Left: Data points colored by assigned clusters 0 and 1. Top right: Data points colored by Glacier. Middle: Convex hull area and sinuosity vs. q_m colored by clusters assigned from 3D cluster analysis. Bottom: Terminus change over time colored by assigned cluster for each glacier used in this study.	150

4.13	Top: 3D Results from the k-means clustering analysis for seasonality, convex hull area, and sinuosity. Top Left: Data points colored by assigned clusters 0 and 1. Top right: Data points colored by Glacier. Middle: Convex hull area and sinuosity vs. H_{ab} colorized by clusters assigned from 3D cluster analysis. Bottom: Terminus change over time colorized by assigned cluster for each glacier used in this study.	151
4.14	Convex Hull area vs. Sinuosity the supplemental glaciers and the original four glaciers used in the morphology analysis. The blue/orange shading are the mean ranges for Convex hull area and Sinuosity for cluster 0/1 determined from from all three cluster analyses. The blue/orange stars are the mean values for cluster 1/2 from all three cluster analyses(see Table 4.4). . . .	152
4.15	Select transects (~ 1 per year) for RNK Glacier.	153
4.16	Select transects (~ 1 per year) for STR Glacier.	153
4.17	Select transects (~ 1 per year) for SIL Glacier.	154
4.18	Select transects (~ 1 per year) for KAS Glacier.	154
4.19	Thermal forcing (TF) from <i>Wood et al. (2021a)</i> , subglacial discharge from <i>Mankoff et al. (2021)</i> , Terminus depth from (<i>Morlighem et al., 2017</i>), and calculated Q_m for RNK glacier.	155
4.20	Thermal forcing (TF) from <i>Wood et al. (2021a)</i> , subglacial discharge from <i>Mankoff et al. (2021)</i> , Terminus depth from (<i>Morlighem et al., 2017</i>), and calculated Q_m for STR glacier.	156
4.21	Thermal forcing (TF) from <i>Wood et al. (2021a)</i> , subglacial discharge from <i>Mankoff et al. (2021)</i> , Terminus depth from (<i>Morlighem et al., 2017</i>), and calculated Q_m for SIL glacier.	157
4.22	Thermal forcing (TF) from <i>Wood et al. (2021a)</i> , subglacial discharge from <i>Mankoff et al. (2021)</i> , Terminus depth from (<i>Morlighem et al., 2017</i>), and calculated Q_m for KAS glacier.	158
4.23	Within Cluster Sum of Squares (WCSS) for values 1-11 of k for our k-means clustering of convex hull area, sinuosity, and H_{ab} . A lower value indicates less variance within each cluster and better clustering of the data. We used the elbow method to choose our optimal cluster (black dashed line).	159
4.24	Within Cluster Sum of Squares (WCSS) for values 1-11 of k for our k-means clustering of convex hull area, sinuosity, and q_m . A lower value indicates less variance within each cluster and better clustering of the data. We used the elbow method to choose our optimal cluster (black dashed line).	160

4.25 Within Cluster Sum of Squares (WCSS) for values 1-11 of k for our k-means clustering of convex hull area, sinuosity, and seasonality. A lower value indicates less variance within each cluster and better clustering of the data. We used the elbow method to choose our optimal cluster (black dashed line). . . . 161

Chapter 1

Introduction

Background and motivation

Since the 1980s, the Greenland ice sheet has been losing ice mass at an increased rate, raising sea level by 13.7 mm since 1972, with projected increases in sea level that range from 5 to 33 cm by 2100 (*Mouginot et al.*, 2019; *Aschwanden et al.*, 2019; *Goelzer et al.*, 2020). This large range in possible future sea level contributions is due to uncertainties in future greenhouse gas concentrations (*Meinshausen et al.*, 2011), as well as poor understanding of the physical processes driving ice sheet mass loss. The ice sheet loses mass through both surface mass balance and ice dynamics. Surface mass balance is the change in ice mass through melting, accumulation, sublimation, and refreezing at the surface of the ice sheet. Ice dynamics changes arise from changes in ice flux. In Greenland, ice dynamics are dominated by the behavior of fast-moving outlet glaciers, the majority of which are marine-terminating. The contributions of surface mass balance and dynamic mass loss have increased over the last few decades in Greenland due to atmospheric and ocean warming (*Fettweis et al.*, 2017; *Noel et al.*, 2017; *Broeke et al.*, 2016; *Mouginot et al.*, 2019; *Straneo and Heimbach*, 2013; *Enderlin et al.*, 2014). However, 66% of the mass loss over the last 46 years in Greenland can be attributed to

changes in dynamics (*Mouginot et al.*, 2019), which is predicted to continue to contribute to $\sim 50\%$ of ice loss in the next 100 years (*Choi et al.*, 2021). Furthermore, changes at the terminus can propagate upstream into the ice sheet, affecting the inland thinning of ice (*Felikson et al.*, 2017, 2021). Although the outlet glaciers in Greenland exhibit loss on long time scales, there is significant heterogeneity in dynamic thinning (*Csatho et al.*, 2014; *Felikson et al.*, 2017), velocity (*Moon et al.*, 2020), and magnitude and duration of terminus retreat for individual glaciers (*Murray et al.*, 2015a; *Catania et al.*, 2018; *Bunce et al.*, 2018; *Black and Joughin*), making it difficult to predict the future behavior of glaciers and therefore accurately represent how they will affect future mass loss of the ice sheet. In part, this is because marine-terminating glaciers sit at the intersection of the ice sheet, ocean, atmosphere, and sedimentary environments and are therefore influenced by a complex set of processes that act on them (Fig. 1.1). With more than 300 marine-terminating glaciers in Greenland, understanding how they will each respond to a warming climate is vital to validating and calibrating ice sheet models to estimate how the ocean impacts glacier termini and, in turn, how mass changes in glaciers may impact the ocean.

Frontal ablation processes, or the melting of the glacier terminus or the calving of icebergs, strongly impact the position and shape of the glacier terminus. Terminus melt is caused by both ambient melting from ocean waters and plume-induced melt from freshwater discharge from the glacier itself. The North Atlantic current brings warm and salty Atlantic waters that enter

the fjords that house Greenland’s glaciers and melt the front of the glacier directly (*Straneo and Heimbach, 2013; Straneo and Cenedese, 2015*). Submarine melting at the face of the glacier can occur via ambient melting, or free convection, due to ocean heat transferred to the terminus. This type of melt is often considered to occur at a constant rate across the entire face of the glacier (*Chauch et al., 2014; Schild et al., 2018*). Alternatively, glacier surface melt, which reaches the base of the glacier through moulins and crevasses, brings this water to the terminus at the grounding line (*Smith et al., 2015*) where it emerges in local, vigorous plumes that rise buoyantly, entraining warm water within the fjord and can contribute significant localized melt to the front of the glacier (*Jenkins, 2011; Carroll et al., 2016*). It has been understood that plume-induced melting has a greater effect on the terminus and fjord circulation than ambient melt alone, however direct observations of glacier termini has shown that ambient melting may be 100x larger than those predicted by theory and models (*Sutherland et al., 2019*). Plumes can also drive the circulation throughout the fjord after mixing with this ambient seawater (*Schild et al., 2018*) and this increases the melt across the face of the terminus and can effectively double the ambient melt rate at the front (*Slater et al., 2018*). The impact of ambient and plume-enhanced melt depends highly on fjord geometry, as this will impact the circulation of warm water to the front (*Wood et al., 2021a; Slater et al., 2022*). Calving is the mechanical loss of ice by which the terminus of a glacier becomes unstable and breaks off into icebergs. A number of processes are expected to affect the rates, amounts, and types

of calving. Longitudinal strain (stretching and compressing) in ice as it flows controls the formation, location, and depth of crevasses (*van der Veen, 1996; Benn et al., 2007*). Basal crevasses dominate in regions floating/near floating ice, and the propagation of basal crevasses tend to create large calving events characterized by large, tabular icebergs (*James et al., 2014; Murray et al., 2015a*). Melt-undercutting from subglacial discharge plumes can thin and weaken the overlying ice, which also promotes calving in smaller, localized blocks (*O’Leary and Christoffersen, 2013; Slater et al., 2017; Fried et al., 2018*) often called serac failure. The processes by which frontal ablation occur may be seen in the shape of the terminus, such as more crenulated, irregularly shaped terminus for melt-dominated systems (*Chauch et al., 2014; Fried et al., 2018, 2019*); and smooth termini that retreat in a step-wise fashion for systems that calve due to buoyant flexure (*Fried et al., 2018; James et al., 2014*).

The combination of frontal ablation and ice motion determines the position of a glacier terminus, with the ice motion being governed in part by the bed topography. Several studies have shown that the bed topography of a glacier imparts a first order control on the amount of retreat that glaciers experience (*Catania et al., 2018; Hill et al., 2018; Bunce et al., 2018*), with overdeepenings in the bed topography leading to faster rates of retreat (*Carr et al., 2015; Lthi et al., 2016; Catania et al., 2018*). Furthermore, the degree to which glacier termini are exposed to warm ocean waters is established by the depth of the terminus below ~ 200 m, (*Carroll et al., 2016; Wood et al., 2021a*), and the general topography of the fjord even kilometers downstream

of the glacier terminus can influence the degree to which warm ocean waters can enter a fjord closer to the terminus (*Christoffersen et al.*, 2011; *Rignot et al.*, 2016b; *Slater et al.*, 2022). Other studies have shown that glaciers are stable or can re-stabilize at “pinning points” where the glacier retreats to a shallow ridge or bump in the fjord (*Warren*, 1991; *Schoof*, 2007). In addition to pinning points beneath a glacier, narrowing of fjord walls also acts as a stabilization point for glaciers (*Meier and Post*, 1987; *McNabb and Hock*, 2014; *Enderlin et al.*, 2013). Frontal ablation processes, calving and melting, occur in all marine glacial systems, but the degree to which each of these processes dominates in a particular fjord is likely to vary from glacier to glacier because they depend on regional climate, ice thickness, and fjord-specific geometry. This variability likely causes the observed variability in ice dynamics (*Bevan et al.*, 2012; *Moon et al.*, 2015; *Motyka et al.*, 2017) and makes it difficult to apply uniform calving or terminus melt “laws” that can be applied uniformly to all systems (e.g., *Amaral et al.*, 2019). By quantifying this variability, we may be able to understand how these processes vary in space and time, which could lead to an improved representation of such processes in ice sheet models (e.g., *Aschwanden et al.*, 2019).

Glacier terminus positions have long been used to observe the health of the Greenland Ice Sheet, in fact, numerous studies have used terminus positions to evaluate the stability of glaciers in concert with the environmental and geometric controls on frontal ablation discussed above (*Warren and Glasser*, 1992; *Warren*, 1991; *McNabb and Hock*, 2014; *Moon et al.*, 2015; *Cook et al.*,

2005; *Howat et al.*, 2008; *Howat and Eddy*, 2011; *Goliber et al.*, 2022). Because terminus positions are observed in satellite imagery, terminus position data is quickly becoming one of the most densely sampled glacier records for Greenland (Fig. 1.2). The bulk of satellite data used to delineate the glacier termini of the Greenland outlet comes from NASA's Landsat mission. Landsat provides a record of free, multi-spectral (optical, near, shortwave, and thermal infrared) satellite imagery for the last 45 years. Pre-Landsat data that can provide longer term context for terminus change is sparse, with the bulk of satellite data acquisition beginning in the early 2000s for Greenland (*Wulder et al.*, 2016). This is, unfortunately, when most outlet glaciers began their retreat that is ongoing today (*Catania et al.*, 2018; *Murray et al.*, 2015a). Other data sets, such as aerial photos (*Bjørk et al.*, 2012), provide long-term context, although sparse temporally. Furthermore, the launch of Sentinel 1/2 in 2014 provides new synthetic aperture radar (SAR) imagery for Greenland and can provide winter terminus data, which is not possible in optical imagery, thus expanding the temporal resolution of terminus data (*Zhang et al.*, 2021). In 2022, if using only Landsat and Sentinel optical imagery, one could obtain approximately ~ 160 images per year for a single glacier (*Goliber et al.*, 2022). These data have yet to be fully utilized and more data are still being collected, thus we must design analyses that can handle the large volume of data available to make inferences about glacier processes that might be controlling mass loss.

Chapter Structure

In this dissertation, I use terminus traces to observe how and why marine-terminating glaciers change in order to better understand the mechanisms behind these complex heterogeneous changes in Greenland. I use terminus traces compiled from numerous manual and machine-learning datasets, primarily from the Landsat archive.

In Chapter 2, I develop the largest database of manually-traced marine-terminating glacier terminus data for use in scientific and machine learning applications. In Greenland, numerous authors have produced terminus traces; however, these are often done in isolation with no coordination in picking particular locations, rates, time periods, or using particular methods. This results in heterogeneity in the data quality, and uneven availability of data for the more general scientific population. I present my methodology for collecting, cleaning, and associating traces with original satellite data, including analysis of regional concentrations of traces, inter-author error, and examinations on the usefulness of a compiled data set. This chapter is published as a highlight paper in *The Cryosphere* under the title “TermPicks: A century of Greenland glacier terminus data for use in scientific machine learning applications”. It is available at <https://tc.copernicus.org/articles/16/3215/2022/>. This chapter is the main source of data for Chapters 3 and 4.

In Chapter 3, I focus on using the location of termini to identify features in the bed topography that inhibit the retreat of glaciers following the onset of ocean warming and widespread glacier retreat in the late 1990s. By identifying

periods of terminus standstill in the long-term terminus record, I am able to identify features in the bed topography at these locations and compare feature geometry across populations of glaciers that have remained stable to glaciers that have undergone extensive retreat. I find that the slope and lateral dimensions of bed features exhibit the strongest correlation to retreat, and that the shape of the bed features permits different styles of terminus retreat, which may be indicative of how different ablation mechanisms are distributed across termini.

In Chapter 4, I use the terminus record defined in Chapter 1, in addition to new machine-learned traces that include wintertime terminus data from Sentinel data, to produce a time series of terminus morphological properties for four glaciers in western Greenland. By distilling the terminus into various morphological properties, we can explore how the shape of the terminus may reflect the processes that act on it in the absence of environmental data, which is much more difficult to obtain. I find that a concave shape, low sinuosity, and high seasonality are present at glaciers that calve via buoyant flexure, while the opposite is true at glaciers that are dominated by melt-induced calving via serac failure. I also find that glaciers do not persistently fit into these two end members, and may switch calving styles over time. This work highlights the usefulness of full-width terminus trace data to understand terminus processes and the need for such observations to improve parameterization of calving in ice sheet models.

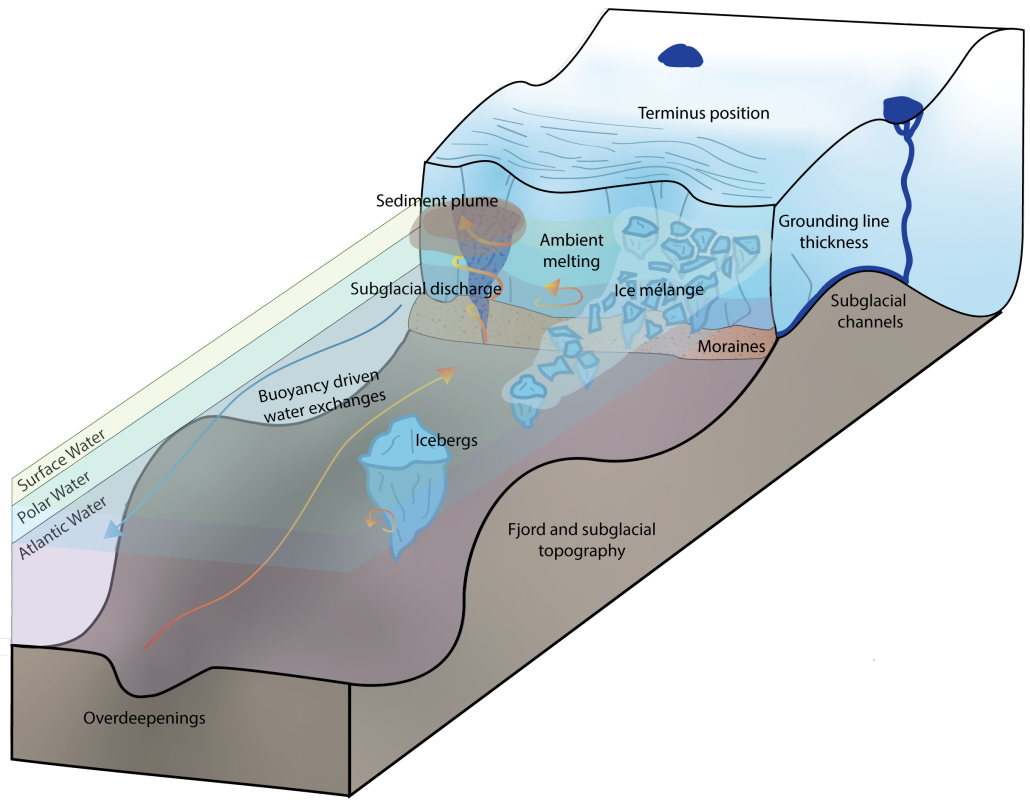


Figure 1.1: Schematic of ice-ocean processes that impact marine-terminating glaciers. The colored water bodies indicate the locations of stratified ocean water found in Greenland fjords. Blue and orange arrows indicate heat exchanges as a result of both warm ocean waters and subglacial water entraining warm water in plumes.

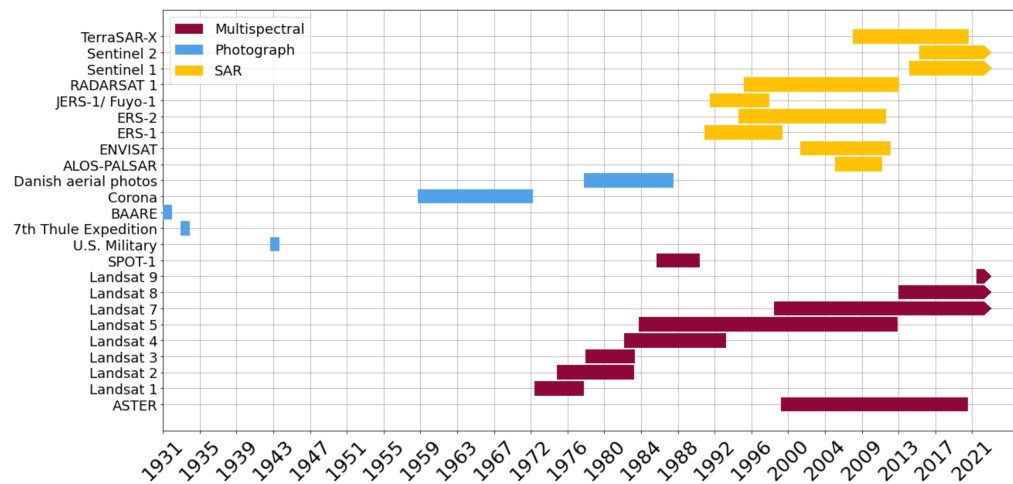


Figure 1.2: Optical satellites commonly used in studies of Greenland. The bars with an arrow at the end are satellites that are currently collecting data. The satellites in this figure are listed in *Goliber et al. (2022)*.

Chapter 2

TermPicks: A century of Greenland glacier terminus data for use in scientific and machine learning applications¹

Abstract

Marine-terminating outlet glacier terminus traces, mapped from satellite and aerial imagery, have been used extensively in understanding how outlet glaciers adjust to climate change variability over a range of time scales. Numerous studies have digitized termini manually, but this process is labor intensive, and no consistent approach exists. A lack of coordination leads to duplication of efforts, particularly for Greenland, which is a major scientific research focus. At the same time, machine learning techniques are rapidly making progress in their ability to automate accurate extraction of glacier termini, with promising developments across a number of optical and SAR satellite sensors. These techniques rely on high quality, manually digitized terminus traces to be used as training data for robust automatic traces. Here we present a database of manually digitized terminus traces for machine learning and scientific applications. These data have been collected, cleaned, assigned with appropriate

¹This chapter has been published in the journal *The Cryosphere*. It is available at <https://tc.copernicus.org/articles/16/3215/2022/>

metadata including image scenes, and compiled so they can be easily accessed by scientists. The TermPicks data set includes 39,060 individual terminus traces for 278 glaciers with a mean of 136 ± 190 and median of 93 of traces per glacier. Across all glaciers, 32,567 dates have been digitized, of which 4,467 have traces from more than one author and there is a duplication rate of 17%. We find a median error of ~ 100 m among manually-traced termini. Most traces are obtained after 1999, when Landsat 7 was launched. We also provide an overview of an updated version of The Google Earth Engine Digitization Tool (GEEDiT), which has been developed specifically for future manual picking of the Greenland Ice Sheet.

2.1 Introduction

Since the 1980s, the Greenland Ice Sheet has been in negative mass balance due to increased surface melt and ice discharge (*Mouginot et al.*, 2019; *Enderlin et al.*, 2014) with projected increases in sea level of 5 to 33 cm by 2100 from Greenland alone (*Aschwanden et al.*, 2019; *Goelzer et al.*, 2020). Long-term historical trends in ice sheet mass loss show that approximately 50% of the total mass loss since the ~ 1990 s is from ice dynamics alone, via fast-moving outlet glaciers that drain into to the ocean (*Enderlin et al.*, 2014; *Mouginot et al.*, 2019; *King et al.*, 2020). In part, this acceleration in dynamic loss may have been triggered by a warming climate (atmosphere and ocean) that induces sudden rapid retreat of outlet glacier termini (*Wood et al.*, 2021a; *King et al.*, 2020). Observations of glacier retreat, however, show a high de-

gree of heterogeneity in the magnitude, timing, and temporal patterns of this retreat across the ice sheet (*Moon and Joughin, 2008; Catania et al., 2018; Murray et al., 2015a; Carr et al., 2017; Fahrner et al., 2021*), which complicates our understanding of future mass change from outlet glaciers. This suggests that knowledge of past terminus change, and the potential for future terminus change, is critical for accurate forecasting of the Greenland Ice Sheet’s contribution to sea level rise (*e.g. Felikson et al., 2017; Aschwanden et al., 2019; Slater et al., 2019*).

Glacier termini have long been an indicator of climate change and terminus change data have been used to understand a range of processes over multiple time scales (*e.g. Warren and Glasser, 1992; Warren, 1991; McNabb and Hock, 2014; Moon et al., 2015; Cook et al., 2005; Howat et al., 2008; Howat and Eddy, 2011*). On the long-term (>annual), terminus records are used to inform the timing of, regional patterns within, and climate controls on marine-terminating glacier retreat (*Murray et al., 2015b; Catania et al., 2018; Hill et al., 2018; Bunce et al., 2018; Howat and Eddy, 2011; Wood et al., 2021a; King et al., 2020; Fahrner et al., 2021*). Outlet glaciers can also change at sub-annual timescales and examination of terminus change on shorter time scales (\sim seasonal) aids interpretation of the specific environmental and glaciological processes that influence glaciers (*Fried et al., 2018; Moon et al., 2015; Schild and Hamilton, 2013; Cassotto et al., 2015; Ritchie et al., 2008; Howat et al., 2010; Carr et al., 2014; Moon et al., 2014, 2015; Brough et al., 2019; Kehrl et al., 2017; Bevan et al., 2019*). Such studies are valuable because glacier

termini respond to a diverse set of mechanisms related to the geometry of the glacier-fjord system, inland ice dynamics, and the strength of climate forcing (*Moon and Joughin, 2008; Carr et al., 2017; Catania et al., 2018; Bunce et al., 2018; Porter et al., 2018*). However, determining the variables controlling seasonal variations can be difficult because changes in the climate system occur simultaneously (e.g. *Cowton et al., 2018; Fahrner et al., 2021; Wood et al., 2021a*). Recent work suggests that the shape of the terminus trace and how it evolves over time may provide additional information about the nature of processes dominating any given glacier (*Fried et al., 2018; Chauch et al., 2014*). Such studies demonstrate the need for detailed tracing of the full terminus width (in map-view) at as high a temporal resolution as possible.

Numerous studies have digitized termini manually (Table 2.1) for use in interpreting glacier dynamics in response to climate variability; however, the lack of coordination across these studies has resulted in duplicated data and heterogeneity in terms of format, quality, method, location, temporal coverage, and availability. Such factors limit the utility of terminus data to future researchers. In addition, manually picking glacier termini is a laborious process. For example, the data set from *Catania et al. (2018)* used the entire Landsat record to digitize 15 glaciers in central West Greenland and the authors estimate that it took 3 undergraduate researchers nearly 2 summers working 15 hours a week each to download imagery and digitize the full width of the terminus, or approximately 48 hours per glacier. Rapidly replacing manual-picking are machine learning techniques, which have recently

been developed for automated extraction of glacier termini across a number of satellite sensors (*e.g.* Mohajerani *et al.*, 2019; Baumhoer *et al.*, 2019; Cheng *et al.*, 2020; Zhang *et al.*, 2021). Manually-digitized data are still needed for validation of machine learning methods and as training data. For example, methods using over 1500 training data inputs result in classification in $\sim 94\%$ of detectable images, under ideal conditions (Cheng *et al.*, 2020). Further, machine learning methods fail in images where ice conditions do not permit easy delineation of the terminus (*e.g.* mélange-choked fjords, shadowed termini, etc.) and therefore manually-digitized termini will still be needed until machine learning algorithms improve. Importantly, future satellite missions imaging the polar regions are expected to continue for the foreseeable future, suggesting an ongoing need to coordinate terminus data in addition to other important glaciological observations that are highly coordinated (*e.g.* velocity and elevation). Here we present the most complete set of manually digitized terminus data for Greenland’s outlet glaciers, re-processed for use in machine learning methods and scientific analysis. Data have been cleaned, associated with appropriate metadata where possible, and the metadata normalized so they can be easily accessed by scientists.

2.2 Methods

2.2.1 Input data

Terminus traces were collected through email requests to authors who had published papers that made use of such data, or taken from publicly

available online databases (Table 2.1). Since there was no open call for data submission, there may be other sources of terminus trace data that are available and/or unpublished. Authors used a range of image sources (Table 2.2), but the bulk ($\sim 70\%$) of terminus traces originate from Landsat images. Collectively, we refer to these collected data as input data to differentiate these data from the output (cleaned, reformatted) training data generated.

All data were provided in ESRI shapefile format (Figure 2.1) with the bulk of data provided as polylines and a smaller volume of data provided as polygons or polygon-boxes. In these latter cases, the polygons were cropped at the terminus and converted into polylines. All glacier terminus traces were exported into a single ESRI line shapefile format consistent with file formats typically used in machine learning techniques. All shapefiles were re-projected into NSIDC Sea Ice Polar Stereographic North (EPSG:3413).

Glacier termini were commonly traced by importing geographically-rectified images into GIS software (*e.g.* ArcGIS, ENVI, and QGIS) and manually-digitizing the ice-ocean boundary (terminus). Authors used a range of methods for tracing termini including picking the full width or variations on the Box methods. Box methods consist of using a fix-width rectilinear or curvilinear box along the length of a fjord tracing the terminus within those bounds (for a description of these methods see *Lea et al.*, 2014). For consistency in data format, we excluded termini that were identified with only a center point (*e.g.* *King et al.*, 2020) because these data do not cover the entire width of termini. Individual terminus trace files are largely indistinguishable between authors,

with the exception of those who used the box method for picking the terminus, since this method often produces terminus traces that are truncated before they reach the fjord wall. Across all authors, terminus traces have an average of 23 vertices per kilometer with a median of 10 vertices per kilometer.

2.2.2 Glacier identification

As the Greenland Ice Sheet has several hundred marine-terminating glaciers, proper identification of glaciers is important for data management. Several prior authors have produced identification files (ID files) for Greenland Ice Sheet glaciers including *Moon and Joughin (2008)* (Moon IDs) who created a glacier ID file by identifying all non-stagnant glaciers that terminate in the ocean with terminus widths of roughly 1.5 km or greater. The Moon IDs identify 239 glaciers that are assigned a numerical ID, including 6 ice cap glaciers that are marine-terminating. We received terminus traces for 278 glaciers but subsequently identified 282 glaciers by including all glaciers with a Moon and Joughin (2008) ID and additional glaciers with the following criteria; 1) surface speeds >50 m/yr, 2) grounding lines below sea-level as determined from the BedMachineV3 bed topographic product (*Morlighem et al., 2017*), and 3) termini greater than or equal to 1 km in width. We excluded terminus traces where only one pick was available for the glacier over all authors as well as land-terminating glaciers (*Mouginot et al., 2019*). Using this new ID system, here termed TermPicks ID, we assigned glacier IDs to each glacier in our database (Figure 2.1).

Our TermPicks ID file maintains consistency with the Moon IDs by including the corresponding Moon ID with the TermPicks ID file. We also include other information in the TermPicks ID file relevant for wide community use, including outlet glacier flux gates identified by *Mankoff et al.* (2019) and glacier naming schemes catalogued by *Bjørk et al.* (2015) in an ESRI multipoint shapefile so the data can be easily referenced with other data sets.

2.2.3 Data cleaning

The number of terminus traces included in an input shapefile varied across the input data. Some authors represented multiple dates per glacier within each shapefile while others included single dates per glacier for each shapefile. Our output data merged all terminus traces for all dates together into one shapefile and so input data were re-processed to fit into this format. Some authors included multiple glaciers per date for a shapefile, particularly when glaciers were adjacent to one another. Where possible, these shapefiles were manually split into traces representing separate glaciers, consistent with our output data format (Figure 2.2c). This was accomplished using the MEASURES Greenland Ice Mapping Project (GrIMP) 2000 Image Mosaic (*Howat et al.*, 2014; *Howat*, 2018) for glaciers to be properly sorted along fjord wall boundaries or ice stream where appropriate. Traces were also clipped using the GrIMP ice mask in order to remove fjord wall traces (*Howat et al.*, 2014). The mask was extended where it did not intersect earlier traces.

Traces that were digitized using the box methods were not interpolated

to the fjord wall. In many cases, the box spans nearly the entire width of the fjord, but several datasets use boxes that are much smaller than the width of the fjord (Figure 2.2a). The lack of data at the edges of glacier termini may lead to differences in total retreat using these data compared to other data (Lea *et al.*, 2014). Thus, terminus traces digitized using the box method are flagged in the metadata (Table 2.3).

2.2.4 Metadata creation

Consistent and uniform metadata are critical to the use of training data in machine learning and scientific studies. Feature extraction using image segmentation techniques rely on accurate attribution of training data to the correct time, location and satellite image used for terminus tracing. Input data used for TermPicks suffered from a lack of consistency in the metadata, such as date format, author and satellite identification, image ID, and digitization techniques. Here we describe the metadata format for the output TermPicks data set (Figure 2.1). The TermPicks metadata format was chosen to be consistent with the largest archive of machine-digitized terminus traces from Cheng *et al.* (2020), known as CALFIN. For example, CALFIN includes the date, quality flags, satellite sensor and image ID, all of which are important for machine learning. Figure 2.3 shows examples of the metadata structure for the data.

Date columns: The Date column represents the acquisition time for the im-

age used to digitize the terminus for that trace. There are 4 additional columns for year, month, day and decimal date. The Date column is a string and the format is "YYYY-MM-DD". Year, month, and day are integers. If a trace included only year information, the date column format is "YYYY-00-00".

Satellite: Satellite refers to the original sensor or satellite that produce an image used to digitize the terminus. This information was taken from existing attribute tables or file names from the input data and was used to determine the image ID where possible. The names used are in listed in Table 2.2.

Author: All people contributing traces have been listed as authors in this paper. Included in the metadata is the Author identifier connected to a specific citation using the data provided. We also provide a code block in the code repository to produce citations for the authors of terminus traces that are used in data downloads. This allows for proper attribution to the correct author depending on the location and time span of data downloaded. In the data set, the author 'TermPicks' refers to terminus traces produced with TermPicks GEEDiT, but are not published elsewhere.

Image ID: Image ID refers to the image scene identifiers for the original image used to digitize the individual glacier trace. This corresponds directly to the sensor. For example, a Landsat Product ID is an example of an image ID. Certain images (*e.g.* some aerial images) were used to digitize multiple traces.

The image ID includes information on the date and location for the original image. This may be listed as a file name that the original author used and may store locally (Figure 2.3; Glacier 291) or an image ID from a different satellite (*e.g.* Sentinel-1 product folder name). If an author included an image ID, the text was kept the same in case users need to contact the original author for image access.

Glacier IDs: The Glacier ID refers to the TermPicks glacier ID scheme that was created for this project (described in section 2.2).

Center X and Y: A centroid point was created for each trace in WGS 84 (EPSG:4326) so that the TermPicks data can be easily referenced with other data sets.

Quality flag: Quality flagging is used to identify and classify traces that may have issues leading to sources of error. This quality flagging scheme was created in conjunction with *Cheng et al.* (2020) to enable data synthesis between our data and machine-generated terminus traces. We assign a prefix 'X' for all data defining whether the trace was created automatically or manually, with X=0 for TermPicks data and X=1 for CALFIN data, or any machine-generated terminus traces that may be included in the future. In addition, traces can have multiple quality flags. We follow the quality flag scheme in Table 2.3. In this scheme, flags are assigned if there are no issues with the

terminus trace (X0), if there is uncertainty in the trace due to environmental or image issues, for example clouds partially obscuring the terminus (X1), if the trace was supplemented (two images were used to digitize the terminus) (X2), if the trace was digitized with the Landsat 7 sensor when the Scan Line Corrector was off (X3), if the trace was digitized using the box method and is thus incomplete (X4), if the image ID was automatically assigned because of lack of information provided in the input metadata (X5). The X1 and X2 flags are only used if the trace author indicated this information, and so many traces will not include these flags. If there are multiple flags, they are separated by commas (Figure 2.3; Glacier 278).

2.2.5 Landsat image scene identifiers

Satellite image scene identifiers (Image IDs) are useful to find the original image from which a glacier terminus was digitized, which is a requirement for these data to be useful for machine learning. Including image IDs is also useful in cases where scientists want to explore other features in the scene at the time of a terminus trace (*e.g.* iceberg distribution, sediment plume occurrence). These were provided in very few of the input data sets. Where no image ID was available, Landsat scene identification is assigned to terminus traces that were originally digitized using Landsat data. Scenes were assigned by geolocating a Path/Row from the Worldwide Reference Systems (WRS-1 for Landsat 1-3; WRS-2 for Landsat 4 onward) that is closest to the termi-

terminus trace, then searching by date using Google Cloud Services. As Landsat scenes are freely available for Level-1 data on Google Cloud Services and most ($\sim 70\%$) of the data are derived from Landsat images, only terminus traces that were known to be digitized with Landsat data are assigned IDs (Figure 2.1). Some glaciers share multiple overlapping Landsat Path/Row combinations resulting in some terminus traces having two scenes assigned. In these cases, both image IDs are appended to the metadata. Glaciers with automatically assigned image IDs have the quality flag of 05 (Figure 2.3; Glacier 3). Further, some terminus traces did not have dates that corresponded to an image ID from Google Cloud Services and were not assigned an image ID.

2.2.6 Calculation of terminus change and variability

In addition to providing manually-digitized terminus traces for glaciers in Greenland, we also computed terminus position change. As many previous studies have already published on terminus change over time, we provide these estimates largely as a check on our data set. We compute terminus position in two ways. First, we calculate terminus position using a method developed in *Catania et al.* (2018) where equally-spaced points along each terminus trace are projected to the nearest location along the glacier centerline. The average position of all projected points on the centerline thus becomes the average position of the glacier terminus for that date of the terminus trace. We call this the Interpolation Method. The Interpolation Method is most accurate when the glacier traces are all approximately the same length (*i.e.* not a mixture

of full-width and box-method termini). Second, we calculate the fluctuation in terminus position simply by taking the point where the terminus intersects the centerline of each glacier following *King et al. (2020)*, here named the Centerline Method. Traces that were missing day and month information were assumed to have a timing of mid-year. Retreat rates were then calculated by taking the distance between each of these terminus positions over time. We use centerlines from *Murray et al. (2015a)* where available for the glaciers in our database. Remaining centerlines were manually mapped from the MEaSURES Greenland Ice Mapping Project (GrIMP) 2000 Image Mosaic (*Howat et al., 2014; Howat, 2018*) through the center of the glacier and the terminus traces.

We also computed the terminus seasonality as a measure of the total variation in the terminus position over the annual cycle. This is quantified using the standard deviation of the difference between raw terminus position data and smoothed terminus position data from the centerline following *Catania et al. (2018)*. We estimated seasonality for glaciers in years where there are terminus traces in at least three unique months.

Finally, we calculated the terminus sinuosity as a way to characterize the shape of the terminus, as the sinuosity quantifies how much the terminus deviates from a straight line. Sinuosity is classically used in river morphology to describe map-view morphological changes in river channel patterns and is the ratio of along-channel length to valley length (*Schumm; Bierman et al., 2016*). Here, terminus sinuosity is measured as the length of the terminus divided by the straight line distance between the terminus end points. Sinuosity

of rivers depends on river valley geology with typical values between 1 and 3 (*Schumm*), however, we do not expect glacier termini to exceed a sinuosity of 2 (*i.e.* the terminus will be less than twice the length of the distance across the fjord) because calving will likely occur for the parts of the terminus that are extremely anomalous. Increased sinuosity of glacier termini may be associated with crenulated terminus morphology that is thought to result from localized terminus melt as a result of buoyancy-driven plumes (*Chauch et al.*, 2014; *Fried et al.*, 2018); however, a smooth but highly concave terminus may also have a high sinuosity. Low sinuosity termini may be associated with glaciers that calve via full-thickness calving events, causing fjord-width step changes in the terminus position with each calving event (*Fried et al.*, 2018; *James et al.*, 2014). While additional metrics of the geometry (*e.g.*, curvature) may be necessary to completely describe the morphology of glacier termini, the change in sinuosity in time may reveal differences in processes affecting a single glacier.

2.2.7 Error Estimation

Terminus traces from different authors on the same date do not necessarily align with each other, and so we quantified the difference between these traces. As a metric of error between data sets, we calculated the Hausdorff distance (commonly used in pattern recognition), the greatest minimum distance between two lines (*Huttenlocher et al.*, 1993). A larger Hausdorff distance indicates two lines are less similar to each other; however, large Hausdorff distances could also indicate that two otherwise identical lines have different endpoints

(different lengths). To avoid this latter issue, we trimmed each terminus trace to a glacier reference box, modified from those used by *Moon and Joughin* (2008), before computing Hausdorff distances. We also excluded traces that did not span the width of these glacier boxes. Excluding short traces reduced the dataset to 25,355 (65% of the original TermPicks dataset). Then, we calculated the Hausdorff distance between every pair of traces for traces that were digitized at the same glacier and on the same date by multiple authors. We identify 2,671 individual instances where multiple authors digitized a glacier on the same date (sometimes more than two authors). This resulted in a total of 5,748 duplicated traces.

2.3 Results

The TermPicks data set includes 39,060 individual terminus traces for 278 glaciers with a mean and median number of traces per glacier of 136 ± 190 and 93, respectively. However, trace count varies depending on author interest in a specific glacier or region of glaciers (Figure 2.4). Across all glaciers, 32,567 dates have been digitized, of which 4,467 have traces from more than one author. This represents duplicated efforts of $\sim 17\%$ of the input data. Traces extend back to 1916 for a small number of glaciers but the greatest number of traces are obtained between 2000 and 2017 (Figure 2.5). See supplemental material for information on individual glacier coverage and statistics (Supp. Figs. 2.14-2.16) as well as access to a kmz file that can be viewed in Google Earth that produces a quick look at location and coverage for each glacier.

2.3.1 Terminus change and variability

The retreat time-series using the Interpolation method reveals small errors that are present as anomalous spikes in the retreat record, possibly due to traces that have different endpoints (*e.g.*, Fig. 2.6). Centerline retreat as an average over each decade of the observational record (1940-2010 where sufficient data permit) shows regional patterns of retreat before 1990 and more ubiquitous retreat after 1990 (Fig. 2.7). Glacier terminus seasonality varies over time and space. Out of the 19 authors in our data set, 10 are able to resolve a seasonal signal for at least one glacier for at least one year (Fig. 2.8). The Catania data are able to resolve seasonal signals across the longest time period (1985-2019), however this is only for 15 glaciers. The Murray data set resolves seasonality for 199 glaciers but only between 2000-2009. In contrast, the TermPicks data set resolves seasonality for the most glaciers ($n = 221$) at different levels of completeness over the longest period of time (1985-2019). For example, Glacier 116 has traces from 7 authors (Fig. 2.9), allowing us to examine changes in seasonality from over ~ 35 years between 1986 and 2017. In contrast, the data from Murray only resolve seasonality for Glacier 116 for 8 years between 2000 and 2008. Finally, we find increases in the amplitude of terminus seasonality during periods of terminus retreat for all three of our example glaciers (Fig. 2.9).

We calculate the sinuosity of Kangerdlugssup Sermerssua (Glacier 291) and Sermeq Silarleq (Glacier 288) between 1990 and 2020, as there is the highest density of traces after 1990 (Fig. 2.10). Terminus sinuosity is found to

vary generally between values of 1 (straight across) to 2 (highly sinuous). We examine two examples with different retreat histories. Glacier 291 is a stable glacier over the observational time period and has a similarly stable sinuosity with a mean of 1.43 ± 0.12 between 1990-2020 (Fig. 2.10). In contrast, Glacier 288 undergoes a two-stage retreat beginning in 1998 with a slower paced stage of retreat until ~ 2010 when retreat accelerated through to today. This glacier has a mean sinuosity of 1.35 ± 0.17 , however, we observe that the slower period of retreat is tied to a period of increased terminus sinuosity of 1.41 ± 0.18 , (Fig. 2.10), while the period of more rapid retreat experiences a decrease in terminus sinuosity to values of 1.29 ± 0.13 (Fig. 2.10).

2.3.2 Spatial and temporal bias

Heatmaps of the output data demonstrate the temporal coverage and frequency of the data. We present heatmaps for both regional groups of glaciers (Fig. 2.5) and individually for each glacier (Supp. Figs. 2.14-2.16). These figures demonstrate that terminus data availability is intimately tied to Landsat image acquisition. A combination of U.S.-centric acquisition strategies, ground station coverage, and limitations on data transmission and duty cycles meant that much of the world did not have regular repeat Landsat coverage until 2013 with the launch of Landsat 8, which follows a continental acquisition strategy (*Wulder et al.*, 2016). Further, the failure of Landsat 6 upon launch in October of 1993 meant that imagery was only obtained in a limited capacity (via extension of the Landsat 5 satellite) until the successful launch

of Landsat 7 in 1999, when we observe an increase in terminus trace data (Fig. 2.5). We further compute the percentage of terminus traces for a given glacier compared to all available Landsat images that cover any particular glacier (see Fig. 2.11 for four examples) in order to examine the completeness of the terminus data for all glaciers. All glaciers have an individual coverage Fig. that is contained in our Google Earth file (Supplementary Information). From this analysis we find that Sermeq Silarleq (ID 288) has traces from 33.1% of all available Landsat images (including cloudy images), the most of any glacier in our data set. However, on average only 5.8% of available Landsat images have been manually traced per glacier.

Regional differences in data availability also exist (Figs. 2.4 and 2.5). Higher latitude glaciers experience more frequent coverage by satellite image sensors than lower latitude glaciers due to increased scene overlap at high latitudes (*e.g.*, Fig. 2.11b after 2013). In Southwest Greenland, there are fewer traces simply due to the lack of marine-terminating glaciers in this region, which is primarily drained through land-terminating ice. There are also fewer overall traces in North and Northeast Greenland than Central West Greenland, a region with a similar number of glaciers, potentially due to less interest in tracing in North and Northeast Greenland (Fig. 2.4). The densest coverage is in Central West and Northwest Greenland (IDs 279 to 3) where nearly every available image from Landsat and other sensors were traced (*Catania et al.*, 2018) to create as complete a record as possible of regional glacier change. Other glaciers of interest include Helheim, Kangerlussuaq, and Sermeq

Kujalleq (Jakobshavn; IDs 181, 152, and 278), which also have dense coverage.

2.3.3 Error in manual digitization

The overall median error between pairs in this reduced dataset is 107 m, which is comparable to that obtained in most machine learning studies when comparing machine-traced termini to manually-traced termini (*Cheng et al.*, 2020). The median error between any given pair of authors varies with the greatest median error (7,350 m) between Cheng and Hill, and the least median error (58.6 m) between Fahrner and TermPicks (Fig. 2.12). The magnitude of errors are not necessarily due to inaccurate digitisation by authors, but can be explained by Hill and other authors focusing on northern glaciers (which can be difficult to trace due to the presence of near-terminus crevasses), and Fahrner focusing on late summer observations where the glacier margin is often most clear. The mean and median of the median errors for each author are presented in Table 2.4, and there was no clear distinction in error based on methodology used (box vs. full-width tracing). Traces with >500 m error between traces were manually checked for errors (220 traces). If two traces were on the same date but the trace was not equivalent (*e.g.* the trace did not appear to be from the same front), then the trace with more complete metadata (*e.g.* includes the original image ID) was kept. If a trace had 3 authors and one was not equivalent, it was removed. Only 0.4% of total traces were removed from the data set through this manual checking. In some cases, there are glaciers that have higher errors than other glaciers (*e.g.* IDs 39, 73,

86, 99, 100, 101) due to the fact that they appear to have highly fractured ice tongues and they develop long, linear cracks that authors may or may not trace in their entirety.

Termini traced with different methods or widths of the glacier may have some systemic differences in terminus retreat over time (*Lea et al.*, 2014). For example, figure 2.6 shows Glacier 152 (Kangerlussuaq Gletsjer) on 8/11/2006. This date was digitized by 3 separate authors (Bunce, Cheng, and ESA) at different extents of the glacier front. When the Interpolation method is used, there is a 0.5 km difference in terminus position change because the end points for each trace are different. Bunce and Cheng will show a higher retreat compared to ESA because the Interpolation method accounts for the entire width of the glacier. Therefore the mean positions of the Bunce and Cheng traces will be further up-glacier as they do not include the lateral tails seen in the ESA trace. While there is no large scale difference between retreats calculated from the box method versus full width traces, users of these data should be aware of this potential misfit between traces based on end points. For example, Bunce traces use the box method while Cheng traces uses the full width method; however, they both end before the fjord wall. Glacier 152 has dead ice on its northern margin and, as shown in the image, the scan line errors in the Landsat 7 imagery block some of the ice, so some authors may or may not digitize the entire front for numerous reasons.

2.4 Discussion

This is the first published study of manually-traced Greenland-specific marine terminating glacier traces with consistent metadata and formatting across multiple data sets from different authors. Glacier terminus traces have been a staple indicator of glacier change for decades (*e.g.* Weidick, 1958; Higgins, 1990; Warren and Glasser, 1992; Murray *et al.*, 2015a). From this paper alone, 22 sources have digitized and interpreted terminus positions in Greenland, with many more using these data to aid interpretation of Greenland Ice Sheet change. However, all of these efforts have happened independently, with duplicate efforts and lack of consistency across data format and accessibility. For example, figure 2.13 shows a time-series of Glacier 116 (F. Graae Gletscher) with author labels for each trace. This figure demonstrates the utility of combining data sources, which enables a more complete view of terminus change at this glacier than any previously-published individual study. We find similar ice-sheet wide retreat patterns as previously published sources. For example, total retreat for 2000-2010 is ~ 252 km in 225 glaciers (Fig. 2.7), which is comparable to Murray *et al.* (2015a) who found ~ 267 km in 199 glaciers. We find the greatest retreats occur from 1990-2010 (Fig. 2.7) similar to Wood *et al.* (2021a) and Fahrner *et al.* (2021). Finally, we find a rapid increase in retreat beginning in 1990s-2000s (Fig. 2.7), similar to Carr *et al.* (2017), King *et al.* (2020) and Fahrner *et al.* (2021). While we recognize that not every glacier has a complete time series or the ability to resolve seasonal changes in terminus position over all years and there remain limitations in drawing large

scale conclusions on retreat patterns with these data alone, we find increases in the amplitude of terminus seasonality during periods of terminus retreat (Fig. 2.9). This may be related to the changes in fjord geometry that glaciers experience as the terminus retreats through overdeepenings.

An additional value of the TermPicks data set is that it provides map-view trace data, not just centerline data, thus informing on morphological changes to the terminus over time. We explore the value of this through examination of the terminus sinuosity, but other measures (*e.g.*, terminus curvature) may also be valuable in contextualizing terminus morphology. While the mean sinuosity for Glaciers 288 and 291 (Fig. 2.10), are similar, we find variations in sinuosity for the glacier that experienced large scale retreat (Glacier 288) compared to the one that has remained stable over the observational period (Glacier 291). Glacier 291 is known to have a terminus that is dominated by plume-driven melting (*Fried et al.*, 2015, 2018; *Jackson et al.*, 2017), and so we might anticipate increased sinuosity related to local melting associated with these plumes (*Chauch et al.*, 2014; *Fried et al.*, 2018). In contrast to this, the terminus of Glacier 288 begins with a relatively low sinuosity, then during the period of slow retreat (1998-2010) experiences an increase in sinuosity (Fig. 2.10) suggesting that this glacier may also have experienced enhance terminus melting due to subglacial discharge plumes during this time. Subsequently, Glacier 288 experiences a period of more rapid retreat as the glacier terminus moves into an overdeepened portion of the bed. Here, sinuosity decreases and terminus change is dominated by full-thickness calving (*Fried et al.*, 2018).

Although machine-enabled terminus tracing has made great strides in the past few years, there will be a continued need for manually-tracing glacier termini. This is because certain environmental conditions, such as heavy shadows, cloud cover, ice mlang, and low solar illumination, make it difficult for current machine learning algorithms to accurately trace all available images. The data provided here will aid improvements in machine learning that will ultimately reduce the need for future manual tracing. Ideally, machine and manual-tracing efforts would work in concert, with data gaps or large errors reported by machine learning quickly identifying where need is the greatest for the manual-tracing team. For example, both the data presented here and the data in CALFIN (*Cheng et al.*, 2020) are not extended beyond 2020 and there is no funding in place to provide continued coordinated (between machine- and manual-traced authors) updates to terminus positions in the future. Coordinated effort between machine- and manual-tracing teams is warranted to ensure regular delivery of future data, given its importance to the wider scientific community.

Until fully-automated, frequently-updated and publicly available terminus traces are available for Greenland and elsewhere, we anticipate that authors will continue to manually-trace in studies that are spatially or temporally limited. Ideally, future efforts would occur in conjunction with our work, producing data with similar format, metadata, and visibility. To that end, we recommend the use of a bespoke version of the Google Earth Engine Digitisation Tool (GEEDiT; *Lea* (2018)) within Google Earth Engines (GEE) API

(Gorelick *et al.*, 2017). This GEEDiT-TermPicks version builds substantially on the original GEEDiT, with improvements made to both the digitisation interface, metadata options, sensor availability, and image accessibility. A major advantage of GEEDiT-TermPicks over traditional repository download and visualization approaches is that it accesses the archive of Landsat, Sentinel-1 and Sentinel-2 and ASTER images on the Google Cloud servers within a standard web browser. It therefore allows for much faster access to imagery compared to the alternative of downloading, extracting, and processing each individual image. This is combined with an interface for easy digitisation of margins that now uses GEEs DrawingTools functions to improve both speed and flexibility of digitisation for users.

To ensure that future data generated using this tool will be consistent with our dataset, the GEEDiT-TermPicks interface visualises the TermPicks ID locations, allowing the user to easily identify the glaciers present and access relevant imagery. Once a glacier is chosen, GEEDiT-TermPicks provides rapid access to all available satellite images of that glacier, which can be pre-filtered by date and satellite. If the image is clear, the termini can be extracted by simply clicking on the screen along the glacier margin. Images with glacier termini that are low in quality can be compared with previous or subsequent images that are nearby in date to help better determine the location of the terminus for a specific date/time. If this is done, it will automatically be flagged in the image metadata, though this (and other) image quality flag options can be manually selected, including options to provide a written note

as to why the image is inadequate. Data exported from GEEDiT-TermPicks will therefore include as standard all metadata required for easy inclusion into future TermPicks data releases.

Finally, we recommend a minimum of 11 vertices per km of trace for quality that is consistent with this database. We also recommend tracing across the entire width of the glacier terminus as previous studies have shown that information about mass loss processes can be obtained from studying the map-view change in trace morphology at high levels of detail (*Fried et al.*, 2018; *Chauch et al.*, 2014).

2.5 Conclusions

We present a new compilation of outlet glacier terminus traces for the Greenland Ice Sheet spanning a time period from 1916 to 2020 obtained through manual tracing of the ice-ocean boundary. Data were cleaned, reformatted, assigned to image IDs, and quality controlled for use in machine learning algorithms that will enable semi-automated terminus tracing. Termini are provided in the same format and with similar metadata to ongoing machine learning-based terminus tracing. We have combined TermPicks data with that from CALFIN (*Cheng et al.*, 2020) in our data repository. We find errors in TermPicks on the order of ~ 100 m, similar to machine-identified termini. We find biases in terms of data coverage with well-studied glaciers with high coverage of terminus trace data, and other glaciers devoid of consistent coverage, showcasing the need for further manual and machine-learning

efforts to provide terminus data. We provide tools for future tracing efforts and include software to enable the use of these data for the broader scientific community.

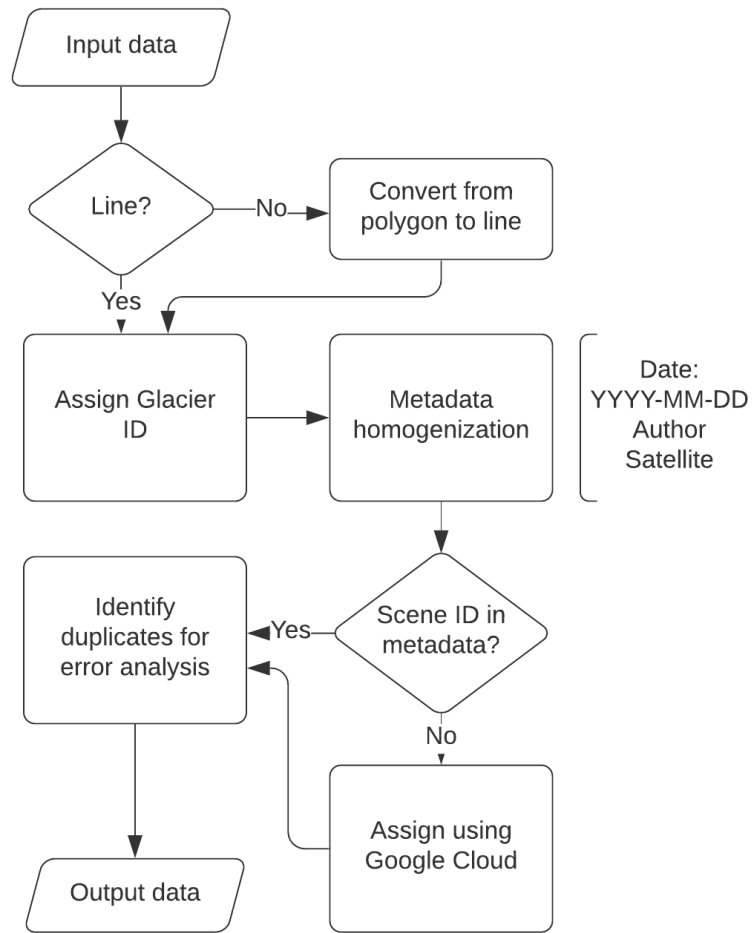


Figure 2.1: Flow chart showing processing pipeline for producing consistent terminus trace training data.

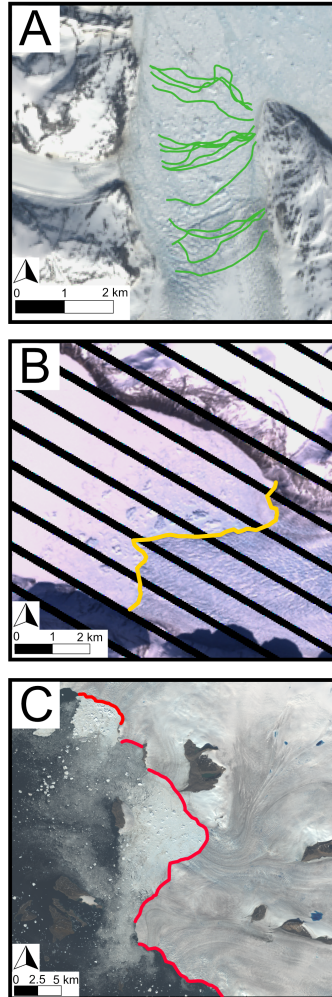


Figure 2.2: Common issues addressed in data cleaning and labeling. a) Box method glacier traces are contained within a box that is smaller than the full terminus width at Glacier 224 b) Landsat 7 ETM+ Scan Line Corrector-off image line artifacts at Glacier 291 and c) A single shapefile containing several different glaciers (IDs 27-30) that need to be split manually into separate glaciers to be consistent with the ID scheme. Additionally, all 3 images show varied levels of obstruction of the terminus in the fjord due to ice mlange. Landsat-7 and Landsat-8 images courtesy of the U.S. Geological Survey.

GlacierID	Date	Year	Month	Day	DecDate	QualFlag	Satellite	ImageID	Author	Center_X	Center_Y
3	2013-07-22	2013	7	22	2013.553425	05	Landsat	LC08_L1TP_014009_20150911_20170404_01_T1	Catania	-52.574288	72.042421
278	2018-02-28	2018	2	28	2018.158904	01,04	Sentinel 1	SEN1_NSIDC_0723_V2_20180226_20180303	Black_Taryn	-49.677742	69.203580
291	1978-07-03	1978	7	3	1978.501370	00	Aerial Photo	874D0164	Korsgaard	-51.406852	71.461398

Figure 2.3: Example metadata for the TermPicks data set. Each column corresponds to the description in Section 2.4 (Metadata Creation).

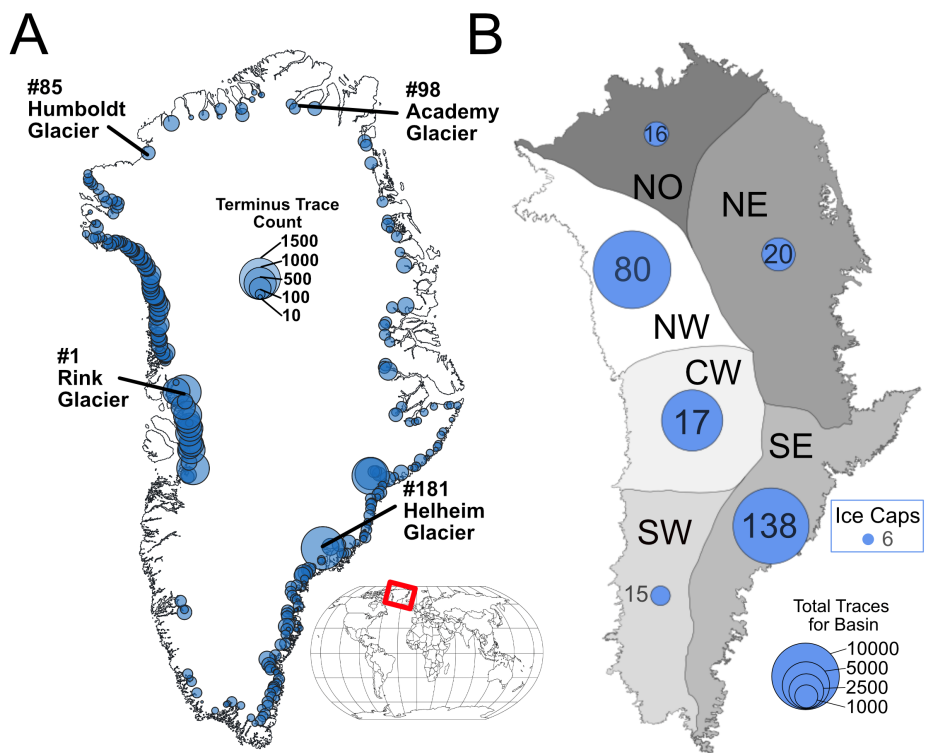


Figure 2.4: A) Terminus trace count for glaciers in Greenland. Each circle is centered on a location of a glacier in the TermPicks ID file. The size of the circle reflects the total number of terminus traces available for that glacier. B) The same data organized by drainage basin. Circle size reflects the total number of traces for that basin. The numbers inside or adjacent to the circle represent the number of individual glaciers in each basin with terminus traces. Each basin is defined by the ESA/NASA ice sheet mass balance inter-comparison exercise 2016 (IMBIE; *Shepherd et al.*) which includes basins from *Rignot and Mouginot* (2012) and *Rignot et al.* (2011). They are labeled by their geographic location. Region labels are NO = North, NE = North East, SE = South East, SW = South West, CW = Center West, NW = North West.

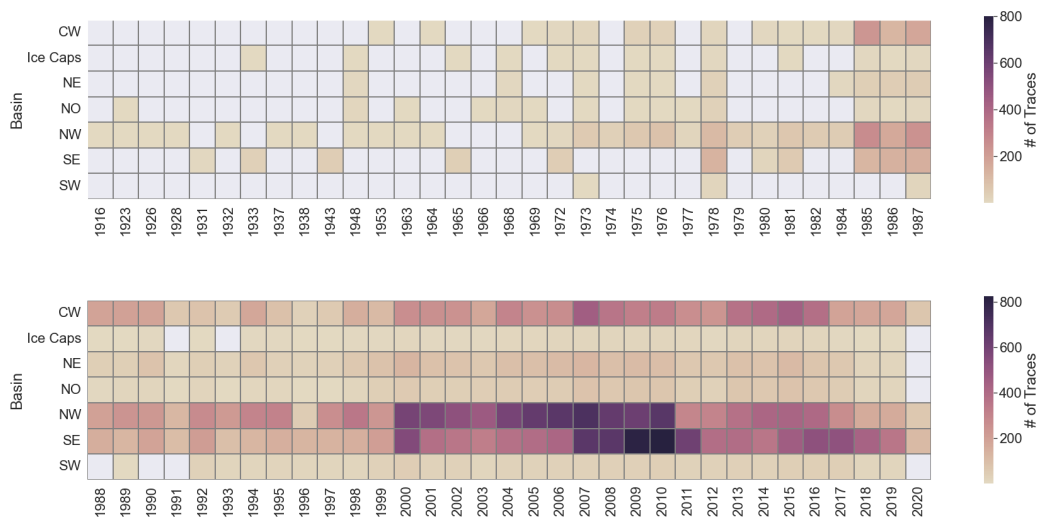
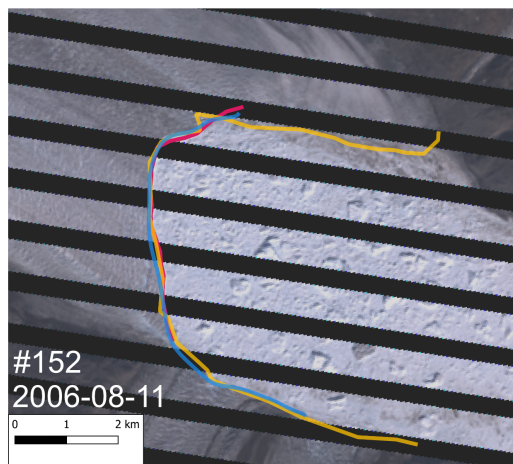


Figure 2.5: Heatmap of glacier traces in each regional basin from ESA/NASA ice sheet mass balance inter-comparison exercise 2016 (IMBIE; *Shepherd et al.*) in this study. Total number of traces per region can be found in Figure 2.4. The x-axis is year and the y-axis is the Basin ID. The color corresponds to the number of traces for that basin’s glacier per year. 0 traces are grey.



Retreat compared to 1978 position		
Author	Interpolation	Centerline
Bunce	6.1 km	6.5 km
Cheng	5.9 km	6.5 km
ESA	4.6 km	6.5 km

Figure 2.6: Terminus positions for Glacier 152 (Kangerlussuaq Gletsjer) from 2006-08-11 for 3 authors. Bunce (pink) and Cheng (blue) traces end before the northern fjord wall while the ESA (yellow) trace ends at the northern wall. The table shows each calculated retreat amount since the 1978 position using the Interpolation method and the Centerline method. Landsat-7 image courtesy of the U.S. Geological Survey. Base image has reduced saturation to increase contrast with traces.

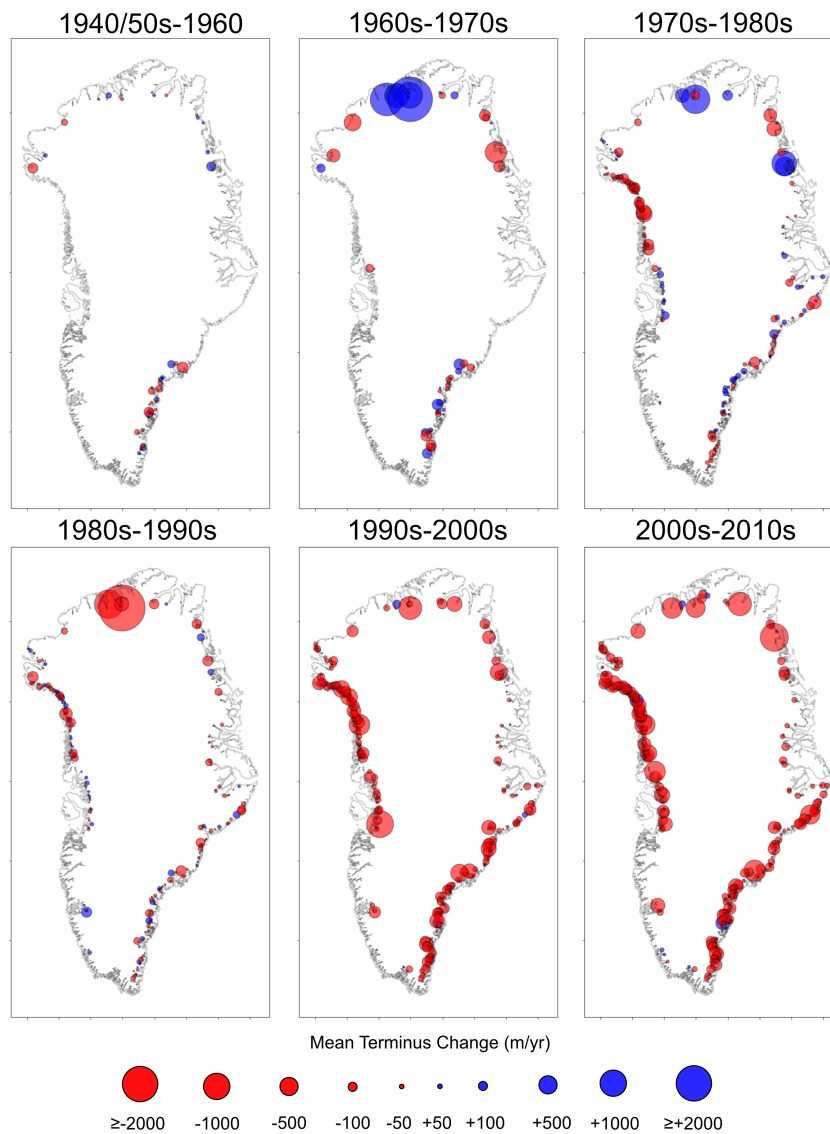


Figure 2.7: Decadal retreat patterns for available TermPicks data using the Centerline method. For each panel, the entire decade of traces were averaged to produce an average position for that decade. The 1940/1950s are an average over both decades as there are fewer traces available in the 1950s. Then the average position for the decade is differenced from average position of the previous decade. The size correlates to magnitude of terminus change, while red (negative) indicates retreat and blue (positive) indicates advance.

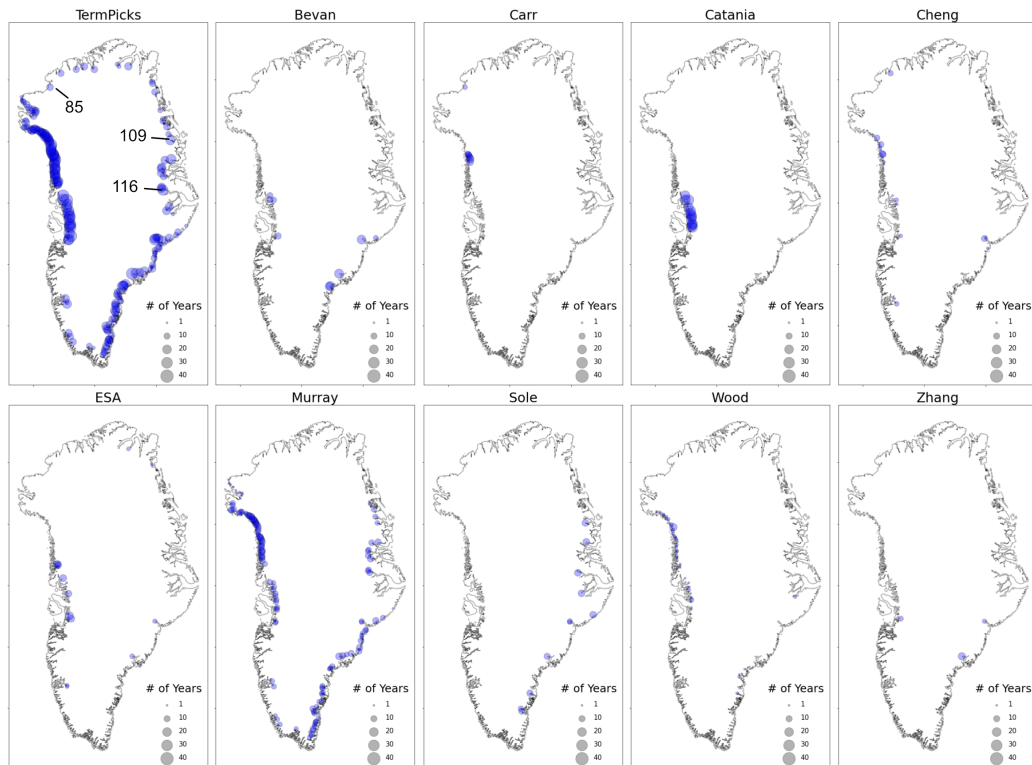


Figure 2.8: Locations of glaciers that include terminus delineations for at least three unique months, which is the minimum number of traces required to resolve seasonality, for the entire TermPicks data set and a subset of authors. The size of the blue circle indicates how many years there are enough traces to resolve seasonality, ranging between a single year to up to 40 years.

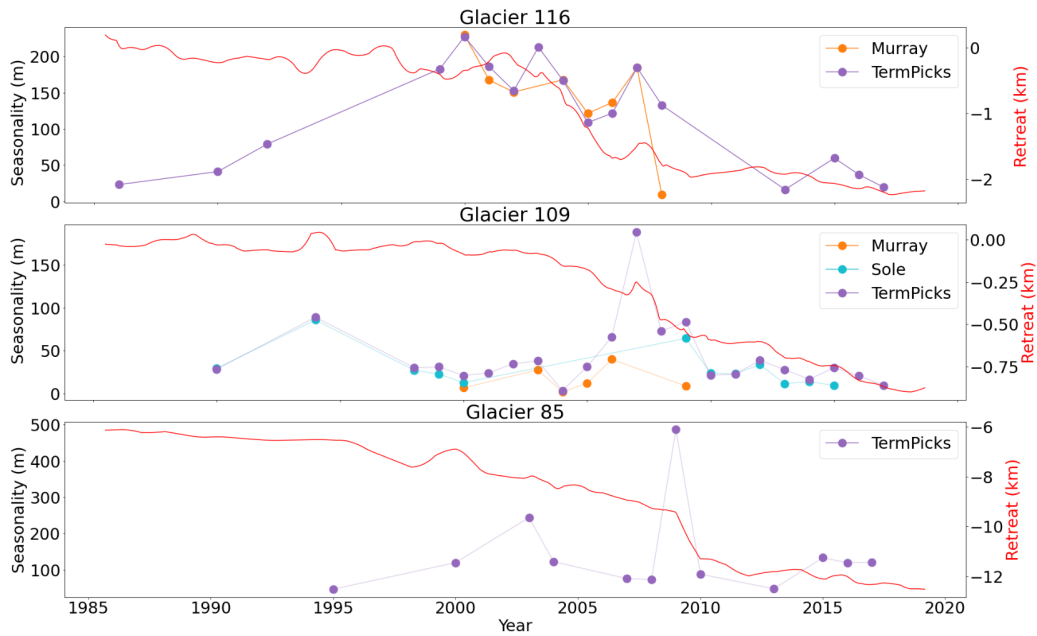


Figure 2.9: Example seasonality plots for three glaciers, F. Graae Gletscher(116), Heinkel Gletsjer (109), and Humboldt Gletsjer (85). The location of each of these glaciers is noted in Figure 2.8. Each color corresponds to either the entire TermPicks data set (purple) or an individual author. Glacier 85 has no individual author data set that can resolve the seasonality.

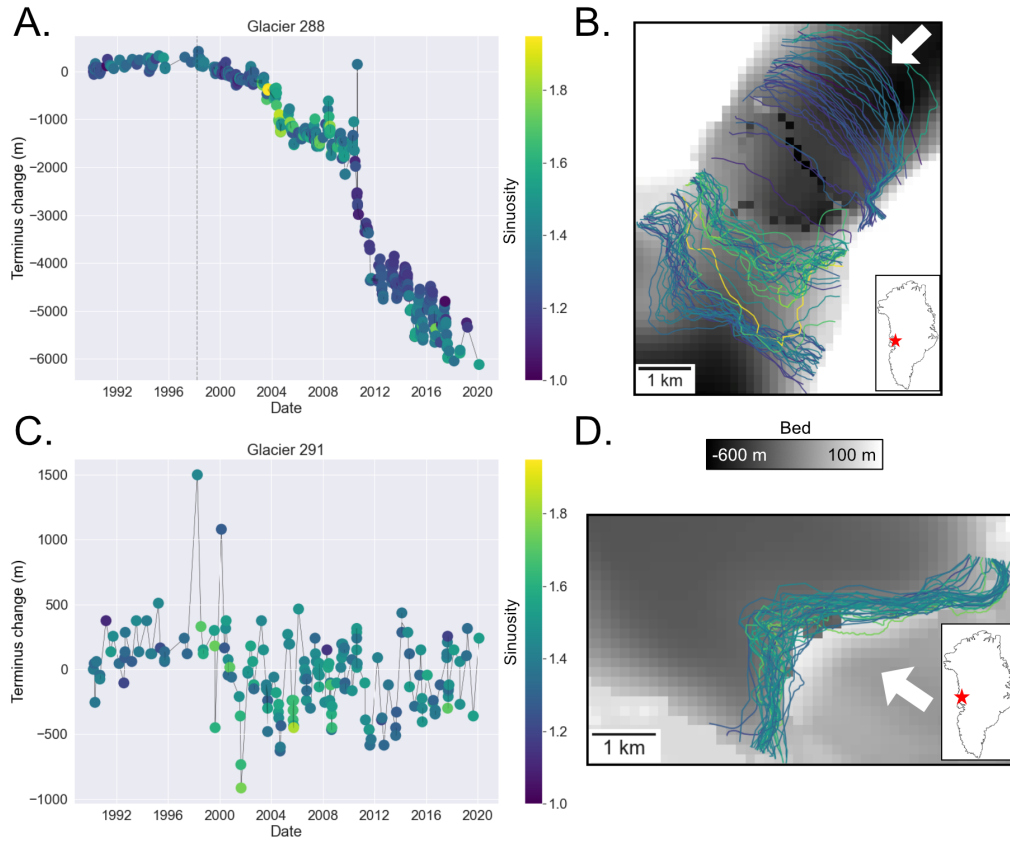


Figure 2.10: A: Terminus change between 1990-2020 colored by sinuosity for Glacier 288 (Sermeq Silarleq). The dashed grey line is the start of progressive retreat as defined in *Catania et al.* (2018). B: Corresponding map-view terminus traces For Glacier 288 with every 5th trace colored by sinuosity. C: Terminus change between 1990-2020 colored by sinuosity for Glacier 291. D: Corresponding map-view terminus traces for Glacier 291 (Kangerdlugssup Sermerssua) with every 5th trace colored by sinuosity. The base map in B and D is the bed from BedMachine (*Morlighem et al.*, 2017). The black pixels in B are errors, however they do not impact the overall interpretation of the bed. The bed scalebar applies to both B and D. The white arrows indicate glacier flow direction. The red star on the inset map is the location of the glacier on the Greenland Ice Sheet.

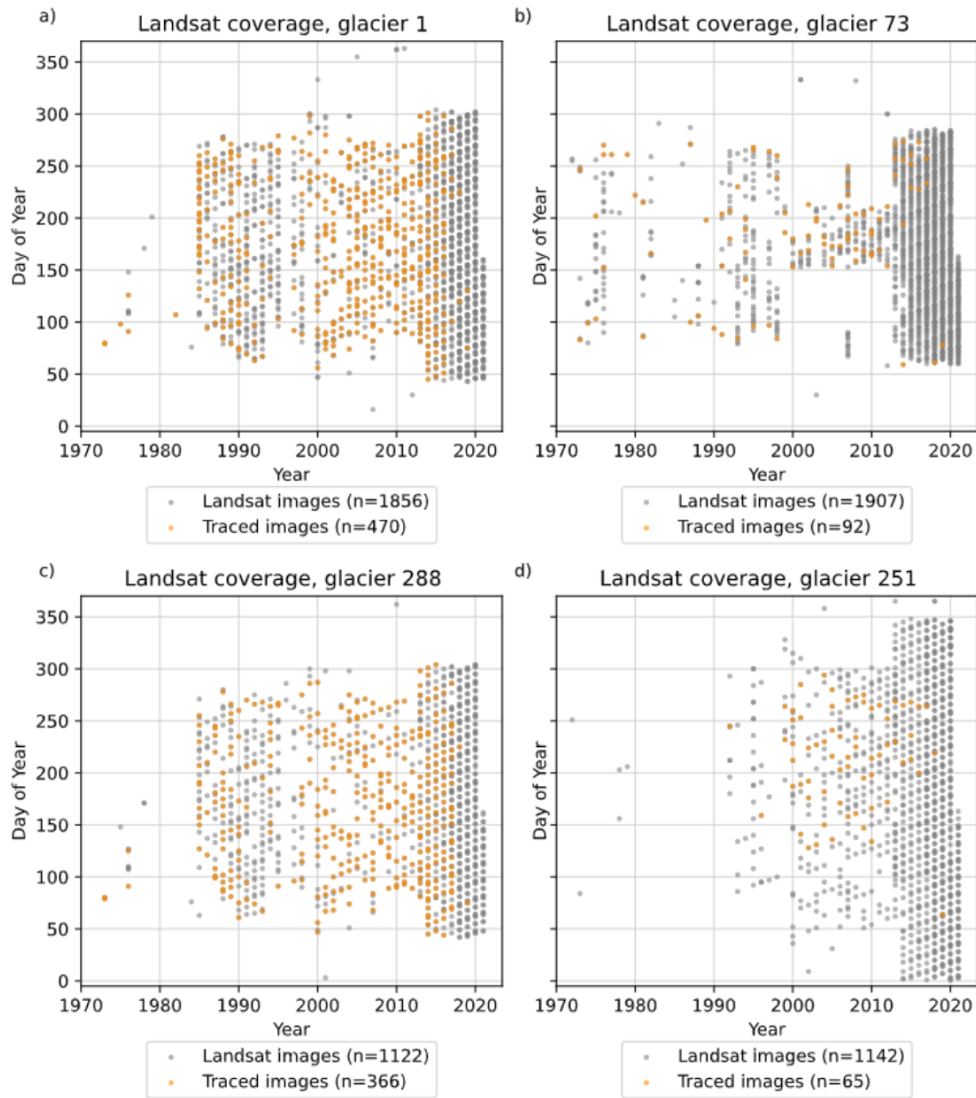


Figure 2.11: Examples of Landsat image availability (gray) versus terminus traced (orange) for (a) Kangilliup Sermia (Rink Isbræ; 1), a relatively well-traced glacier, (b) Qeqertaarsuusarsuup Sermia (Tracy Gletsjer; 73), a glacier representative of the average number of total traces for this dataset, (c) Sermeq Silarleq (288), the glacier with the highest percentage of available Landsat images that have been traced in this dataset, and (d) an unnamed glacier (251), representative of the average percentage of available Landsat images that have been traced in this dataset.

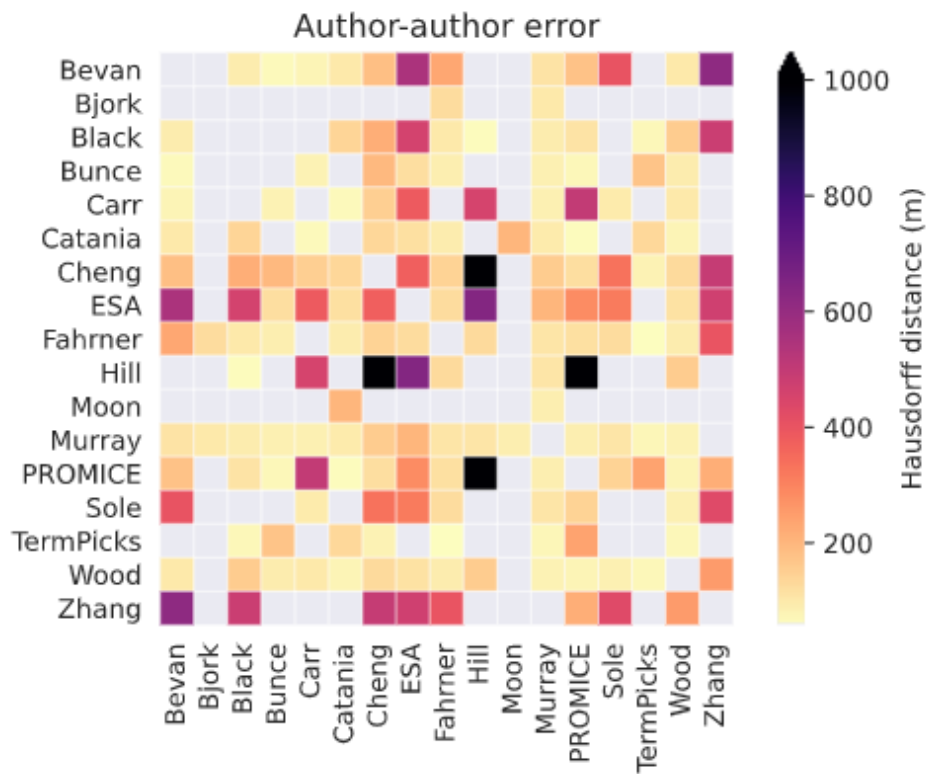


Figure 2.12: Median error between pairs of authors, for instances where those authors have duplicated a glacier trace on a given date. No color indicates two authors have no duplicated traces between them.

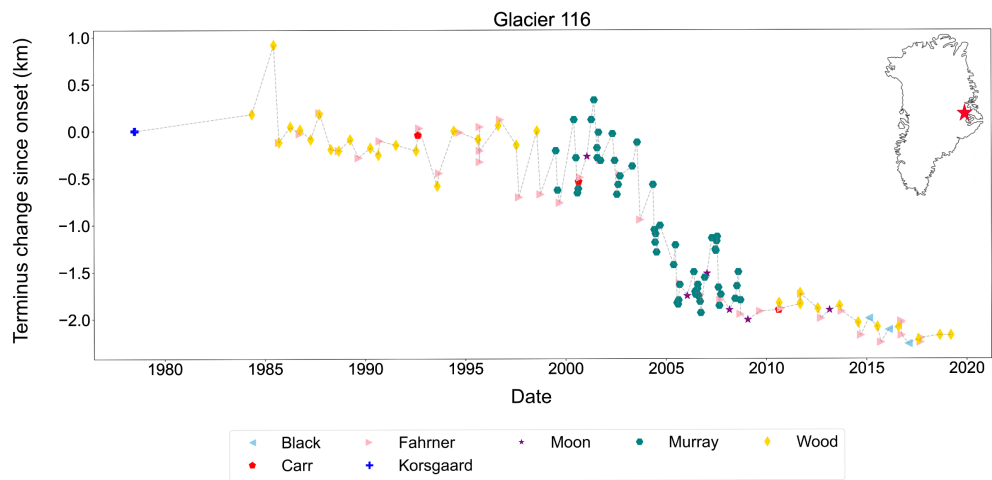


Figure 2.13: Example terminus change for Glacier 116 (F. Graae Gletscher). Color and symbol correspond to different authors for each pick.

Published source	Spatial coverage	Date range	Resolution	Method	Author key
<i>Andersen et al. (2019)</i>	GrIS wide; n =47	1999-2018	Annual	Full width	PROMICE
<i>Bevan et al. (2012)</i>	GrIS wide; n = 14	1985-2011	Sub-annual	Full width	Bevan
<i>Bevan et al. (2019)</i>	Kangerlussuaq; n = 1	1985-2018	Sub-annual	Full width	Bevan
<i>Björk et al. (2012)</i>	SE GrIS, n =132	1931-2010	Decadal-sub-decadal	Full width	Bjork
<i>Black and Joughin</i>	NW GrIS; n = 87	1972-2021	Annual	Box	Black
<i>Brough et al. (2019)</i>	Kangerlussuaq, n = 1	2013-2018	Sub-annual	Box	Brough
<i>Bunce et al. (2018)</i>	NW and SE; n = 276	2000-2015	Annual	Box	Bunce
<i>Carr et al. (2013)</i>	NW GrIS; n = 10	1976-2012	Decadal to monthly	Box	Carr
<i>Carr et al. (2017)</i>	GrIS Wide; n = 273	1992-2010	Decadal	Box	Carr
<i>Carr et al. (2015)</i>	Humboldt ; n = 1	1975-2012	Decadal-sub-decadal	Full width	Carr
<i>Catania et al. (2018)</i>	CW GrIS; n = 15	1965-2018	Sub-annual	Full width	Catania
<i>Cheng et al. (2020)</i>	GrIS wide; n = 65	1972-2019	Sub-annual	Full width	Cheng
<i>Cowton et al. (2018)</i>	E GrIS; n = 10	1993-2012	Sub-annual	Box	Sole
<i>Fahrner et al. (2021)</i>	GrIS wide; n = 224	1984-2017	Annual	Full Width	Fahrner
<i>Hill et al. (2017)</i>	N GrIS; n = 21	1916-2015	Annual	Box	Hill
<i>Hill et al. (2018)</i>	N GrIS; n = 18	1948-2015	Annual	Box	Hill
<i>Korsgaard (2021)</i>	GrIS Wide; n = 452	1978-1987	Annual	Full width	Korsgaard
<i>Moon and Joughin (2008)</i>	GrIS wide; n = 203	1992-2007	Sub-decadal	Box	Moon
<i>Murray et al. (2015a)</i>	GrIS wide; n = 199	2000-2010	Sub-annual	Full width	Murray
<i>Raup et al. (2007)</i>	GrIS wide; n = 28	1990-2016	Sub-annual	Full width	ESA
TermPicks	E and W GrIS; n = 13	1985-2019	Sub-annual	Full width	TermPicks
<i>Wood et al. (2021a)</i>	GrIS wide, n = 226	1992-2017	Annual	Full width	Wood
<i>Zhang et al. (2019)</i>	Helheim, Jakob., and Kanger.; n = 3	2009-2015	Sub-annual	Full width	Zhang

Table 2.1: Original sources for terminus traces for the TermPicks data set. Spatial coverage describes the number of glaciers and name/region(s) of the traces. Date range are the years covered by the data set. Resolution is the temporal resolution; Annual is approximately one trace per year, sub-annual is more than one trace per year, decadal is approximately one trace every ten years, sub-decadal is more than one trace every 10 years, but not each year. Method is the tracing method used by the author to digitize the terminus. The Author key is the label given to that data set in the TermPicks data set.

Source name	Start date	End date	Spatial res. (m)	Temporal res. (days)	Sensor type
ASTER	01-2000	11-2020	15-19	16	Multispectral
Landsat 1	07-1972	01-1978	80	18	Multispectral
Landsat 2	01-1975	08-1983	80	18	Multispectral
Landsat 3	03-1978	09-1983	80	18	Multispectral
Landsat 4	07-1982	12-1993	30	16	Multispectral
Landsat 5	03-1984	01-2013	30	16	Multispectral
Landsat 7	04-1999	Ongoing	30	16	Multispectral
Landsat 8	02-2013	Ongoing	30	16	Multispectral
Sentinel 1	04-2014	Ongoing	20	6-12	SAR
Sentinel 2	06-2015	Ongoing	10	12	Multispectral
SPOT-1	02-1986	12-1990	20	26	Multispectral
Corona	06-1959	05-1972	7.5	Irregular	Photograph
7th Thule Expedition	1933	1933		Single	Photograph
Aerial Oblique Photos					
British Arctic Air Route Expedition (BAARE)	1931	1931		Single	Photograph
Danish aerial photos	1978	1987		Single	Photograph
US Navy/US Army Air Force	1943	1943		Single	Photograph
ALOS-PALSAR	01-2006	04-2011	10-20	14	SAR
ENVISAT	03-2002	04-2012	30	35	SAR
ERS-1	07-1991	03-2000	30	3, 35, and 168	SAR
ERS-2	04-1995	09-2011	30	3, 35, and 168	SAR
JERS-1/ Fuyo-1	02-1992	10-1998	18	44	SAR
TerraSAR-X	01-2008	12-2020	40	11	SAR
RADARSAT 1	11-1995	03-2013	100	11	SAR

Table 2.2: Image sources used in this compilation of manually-traced glacier terminus trace dataset.

Flag code	Issue
X = 0	Manually-digitized trace
X = 1	Machine-generated trace
X0	No issues
X1	Trace uncertainty due to environment or image issues (clouds, shadows, missing data, etc.)
X2	Supplemented trace
X3	Landsat 7 SLC off
X4	Incomplete/Box Method
X5	Automatically assigned Image ID

Table 2.3: Flags assigned to output terminus trace data, created in conjunction with CALFIN (*Cheng et al., 2020*). All data in the TermPicks dataset has the prefix of X = 0.

Author	Vertices per km	Mean median error (m)	Median median error (m)
Bevan	2.5	227.5	145.8
Bjørk	14.2	113.6	113.6
Black	5.7	181.9	111.2
Brough	N/A	N/A	N/A
Bunce	14.1	109.0	88.3
Carr	7.1	201.0	98.0
Catania	18.3	112.7	100.9
Cheng	211.1	720.5	171.8
ESA	10.4	321.9	317.8
Fahrner	5.9	139.3	122.5
Hill	10.0	1458.8	309.1
Korsgaard	9.7	N/A	N/A
Moon	5.5	148.0	148.0
Murray	6.3	106.7	96.5
PROMICE	16.5	355.5	133.2
Sole	5.4	228.1	144.5
TermPicks	11.8	113.7	78.7
Wood	23.1	114.5	96.7
Zhang	55.7	421.8	452.0

Table 2.4: Mean vertices per kilometer of trace, and mean and median of the median errors of each author compared to other authors.

2.6 Supplemental Materials

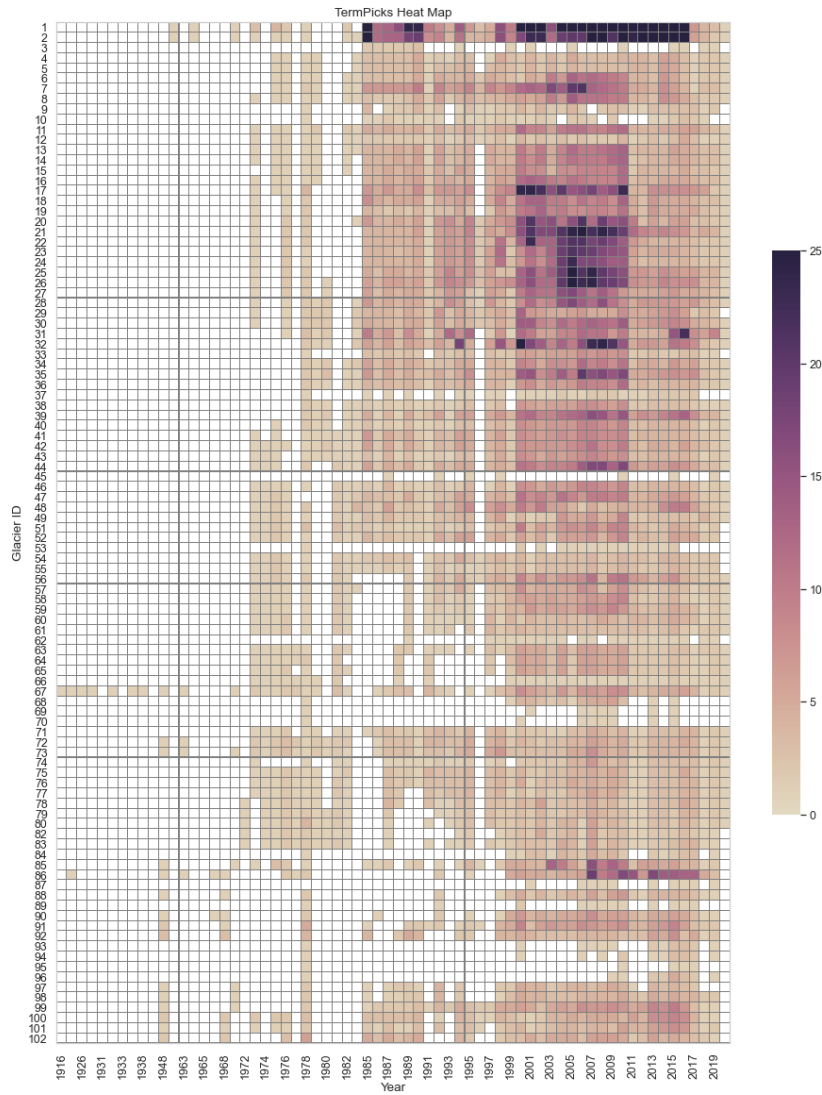


Figure 2.14: Heatmap of glacier traces for glaciers 1 to 102. The x-axis is year and the y-axis is the Glacier ID. The color corresponds to the number of traces for that basin's glacier per year, between 1 and 25. 0 traces are grey.

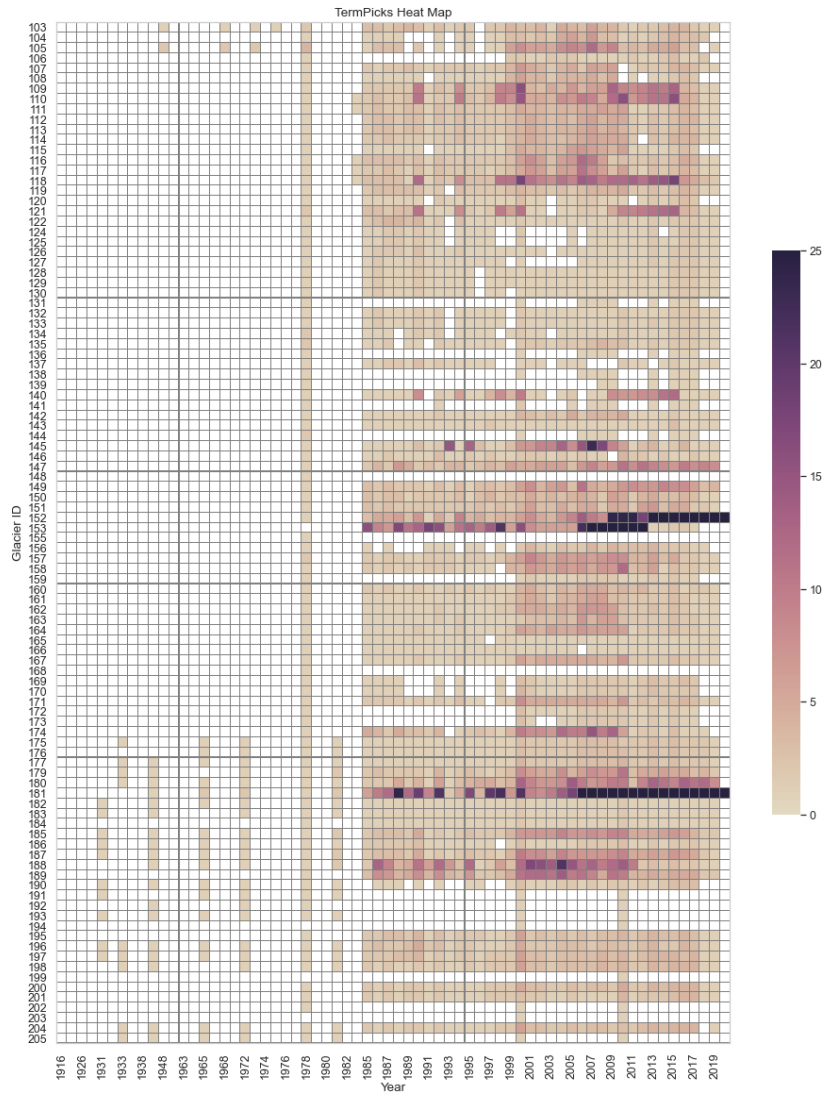


Figure 2.15: Heatmap of glacier traces for glaciers 103 to 205. The x-axis is year and the y-axis is the Glacier ID. The color corresponds to the number of traces for that basin's glacier per year, between 1 and 25. 0 traces are grey.

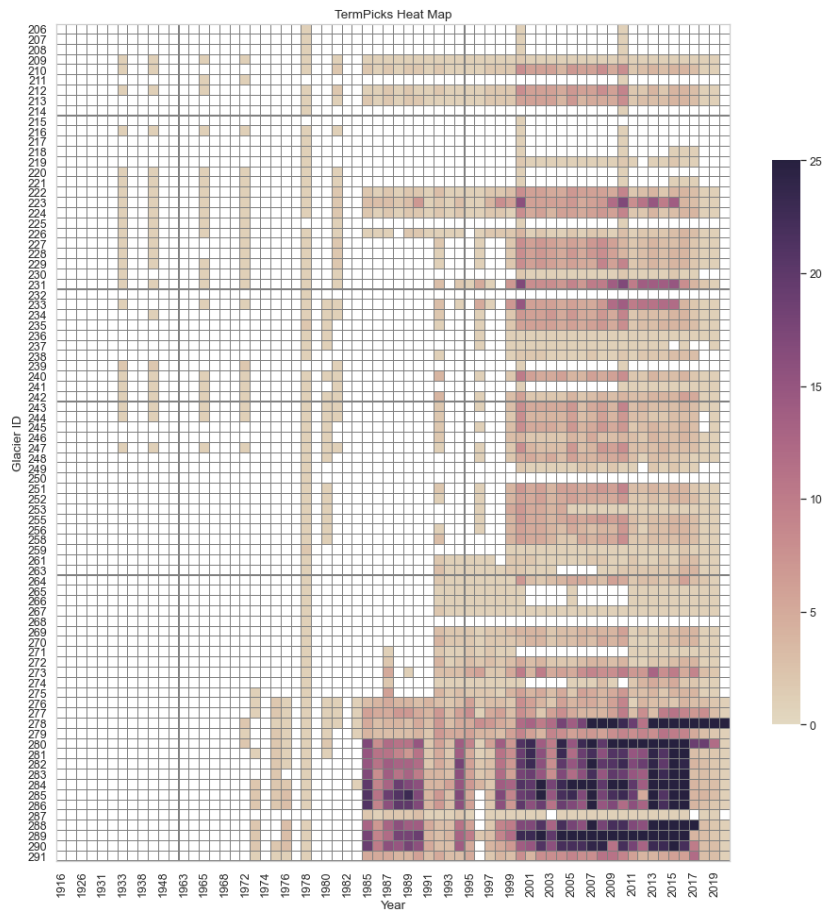


Figure 2.16: Heatmap of glacier traces for glaciers 206 to 291. The x-axis is year and the y-axis is the Glacier ID. The color corresponds to the number of traces for that basin’s glacier per year, between 1 and i 25. 0 traces are grey.

Chapter 3

Bed topographic controls on heterogeneous terminus dynamics in Greenland

Abstract

While the Greenland Ice Sheet has been losing mass ubiquitously, glacier terminus change is heterogeneous across the ice sheet, and this heterogeneity has been attributed to differences in glacier bed and the topography of the fjord. Despite the clear importance of subglacial topography, it is often examined in the paleo setting, where we lack information about the ice sheet behavior at the time of deposition, or it is modeled simply without the complexity represented in the observational data. Thus, it remains unclear what specific aspects of the bed and/or fjord are critical to terminus stability. Here, we compare terminus retreat over the satellite era to bed geometry across a suite of glaciers in Greenland with divergent terminus histories to assess what differences in bed topography control terminus retreat. We identify three main types of bed features present at locations associated with low terminus retreat (i.e., long-term stability); moraines, benches, and ridges. Further, stable glaciers are all grounded on the prograde side of a bed feature, and these bed features have higher prograde slopes than those found for glaciers that experienced retreat. In contrast, glaciers that retreated in the satellite era

initially experienced periods of transient stability on bed features. Retreating glaciers were also frequently grounded on the retrograde side of the bed feature before retreating. Finally, we find that different features permit different styles of terminus retreat, which may affect the timing of retreat onset. Our study highlights the need for more high-resolution surveys of the glacier terminus region and complex geometries of pinning points.

3.1 Introduction

The Greenland Ice Sheet has been in negative mass balance since the 1980s, with $\sim 66\%$ of the mass loss attributed to enhanced flow through outlet glaciers (*Mouginot et al.*, 2019). Glacier mass loss contributes to sea level rise, with predictions of up to 14 cm of global sea level rise by 2100 from outlet glacier discharge from the Greenland Ice Sheet alone (*Aschwanden et al.*, 2019). Although outlet glaciers in Greenland exhibit loss over long time scales, there is significant heterogeneity in the timing and amount of dynamic change (*Csatho et al.*, 2014; *Mankoff et al.*, 2020b; *Moon et al.*, 2022; *Murray et al.*, 2015a) making it difficult to predict the future behavior of any one glacier. The observed heterogeneity in glacier dynamics can arise from natural climate variability (*Christian et al.*, 2022) as well as local (fjord-scale) variability in bed geometry (*Catania et al.*, 2018; *Bunce et al.*, 2018). The geometry of the bed beneath the ice exerts a first-order control on the state of stress within a glacier (*Bassis and Jacobs*, 2013; *Pfeffer*, 2007). Furthermore, the topography of the fjords may also block warm Atlantic water from entering the fjords,

protecting the glacier termini from melting (*Straneo et al.*, 2010; *Rignot and Mouginot*, 2012; *Rignot et al.*, 2016a; *Bartholomaus et al.*, 2013). Topography is not stagnant, but can be built and destroyed over time, as glaciers are effective erosive agents (*Koppes and Hallet*, 2006) that can bring large volumes of sediment to their termini, forming moraines (*Alley et al.*, 1997; *Cowton et al.*, 2012). This raises the possibility that some of the heterogeneity found in Greenland glacier dynamics over time may alternatively be explained as a result of the complex interactions between sediment and ice sheet dynamics (*Brinkerhoff et al.*, 2017).

As a glacier retreats on a retrograde bed slope, its terminus retreats to deeper parts of the bed, and the ice at the grounding line becomes thicker. As a result, the ice flux must increase, creating a positive feedback that enables further retreat, known as the Marine Ice Sheet Instability (MISI *Schoof*, 2007; *Weertman*, 1974). In Greenland, MISI is observable on the scale of the outlet glaciers, as the retreat of each individual glacier appears to be paced by the size of the local over-deepening immediately behind the terminus (*Carr et al.*, 2015; *Catania et al.*, 2018). The converse is also true, as bed bumps (including moraines) stabilize glaciers due to flow restriction (*Warren*, 1991; *Enderlin et al.*, 2013; *Lthi et al.*, 2016; *Morlighem et al.*, 2016a). In fact, bed bumps at glacier termini may be the most important in determining the future evolution of a glacier in response to climate change (*Castleman et al.*, 2022). Indeed, recent model work by *Robel et al.* (2022) suggests that terminus persistence at bed bumps is associated with more steeply sloped retrograde bed

slopes at these bumps. However, despite the importance of bed bumps, the specific aspects of their morphology and geometry that might be responsible for heterogeneous glacier terminus behavior have not been examined.

The impact of bed bumps on glaciers is readily evident in the paleo-environment, where moraines and other glacial landforms serve as indicators of fast flow and terminus position over time (*Winkelmann et al.*, 2010; *Batchelor et al.*, 2019; *Arndt et al.*, 2015). This work suggests that any relationships identified in the modern glaciological setting should hold true for the paleo-glaciological setting; retreat rate increases as the glacier moves into deeper parts of the fjord (*Greenwood et al.*, 2021), and the glaciers stabilize when they enter more constricted parts of the fjord (*Briner et al.*, 2009). However, the elevation of bed topographic features does not always act as an impediment to retreat, particularly in the case of fast flow (*Greenwood et al.*, 2021), suggesting that other aspects of these features might be important controls on ice dynamics. While paleo-glaciological studies typically examine bed topography with high-resolution instrumentation, they cannot obtain simultaneous high-resolution terminus dynamics (at the time of deposition) to ascertain how the terminus position is controlled by different aspects of bed morphology. This is the focus of the present study. Our goal is to quantify the morphological variability across bed topographic features where glaciers have experienced standstills (persistent and transient). We explore these relationships between glacier populations that have experienced regional (although heterogeneous) retreat beginning in the late 1990s. We examine the bed using BedMachineV4

(*Morlighem et al.*, 2017) in fjords with bathymetric surveys that allow an examination of paleo-topographic features at times when glaciers were in standstill during the satellite era. We also use new records of terminus position over this same time period (*Goliber et al.*, 2022; *Cheng et al.*, 2020) with a resolution high enough to allow examination of the variability in the position of the terminus at standstills. We find very diverse bed geometries across this population and the prograde slope, lateral shape, as well as the initial position compared to a bed peak are important factors on the recent stability of Greenland glaciers. Our work suggests that, given a climate perturbation, differences in bed slope, terminus position on that bed slope, and feature type present in the fjord may determine whether a glacier will retreat.

3.2 Methods

Our main goal for this study is to examine differences in terminus bed topography across a population of glaciers that have experienced heterogeneous terminus change during the satellite era. Although Greenland has ~ 300 outlet glaciers, not all of these glaciers have sufficient data to allow examination of how bed topography controls terminus dynamics. For this task we require; 1) an adequate number of terminus traces per year ($n > 2$ in unique months per year) to examine the change in terminus position, sub-annual interaction between the terminus and the bed geometry, and the map-view pattern of terminus change; 2) adequately resolved bed/fjord topography in the vicinity of past and present-day terminus standstills, and; 3) heterogeneity

in the glacier dynamic behavior over the satellite era to provide contrasting inferences of the controls of bed topography on glacier dynamics to be tested. Further details on each of these requirements are provided below.

3.2.1 Identifying Glaciers with Adequate Data

Terminus trace data come from delineations of the ice-ocean boundary of outlet glaciers using satellite or aerial images at a specific date. These data are provided through a combination of the TermPicks and CALFIN data sets (*Goliber et al., 2022; Cheng et al., 2020*). In some cases, we correct CALFIN terminus traces that erroneously extend along the fjord walls by manually clipping these to the ice-ocean boundary. In combination, TermPicks and CALFIN data cover the time period 1916-2020; however, we only examined those glaciers where there are more than two terminus traces in unique months per year. This allows us to examine both long-term retreat and seasonality. With this restriction, viable terminus data extend over the time period 1985-2019. Most glaciers in Greenland began their retreat in the late 1990s (*Catania et al., 2018; Murray et al., 2015a*), so we cover this time period and can examine the topographic features of the bed from which these glaciers retreated at this time.

We also wish to have a balanced number of glaciers experiencing retreat and stability over the observational period. Thus, we need to examine the total terminus change over time to classify glaciers as retreating or stable over the satellite era. To quantify glacier terminus change, we use raw terminus trace

data to calculate the mean position of the terminus for each trace as a time series following *Catania et al.* (2018). We also computed a long-term average terminus position by interpolating this raw signal over a 14-day time interval (to account for missing data) and applied a 4-year moving average to remove seasonality in the raw terminus data. This long-term average terminus position is then used to classify glaciers as “retreat” glaciers if they have retreated more than 1 km over the observation period and “stable” glaciers if they have not moved more than 1 km. Since the majority of glaciers in the Greenland Ice Sheet have been in a phase of retreat since the 1990s, there are far fewer glaciers that have remained in persistent standstill over the satellite era. To compare populations of different sizes, we make use of Welch’s T-Test (Welch, 1947), which can determine the significance of differences between populations with small sample sizes ($n < 30$). We report the results of the t test as $t(\text{degrees of freedom}) = \text{the t-statistic}$, $p = \text{the p-value}$.

Finally, we limit our observations to glaciers with adequate bed topographic data using data from BedMachineV4, a Greenland wide ice bed/fjord topographic map (*Morlighem et al.*, 2017). BedMachineV4 combines extensive ship-based bathymetric and ice-penetrating radar surveys in a mass conservation approach to create a data-constrained ice thickness and bed topography estimate for Greenland that includes many fjords. Where bathymetry data are available right in front of an outlet glacier terminus and radar data are available upstream of the terminus, bed topography across glacier termini is seamless. Uncertainties in bed topography arise in areas where data are sparse.

We used the BedMachineV4 source location mask to identify where bathymetric and/or radar data are available for each glacier. We numerically classify the data coverage for each glacier fjord in BedMachineV4 as follows. A classification of 1 is given when bathymetric coverage and radar data extend to the location of a standstill. A classification of 2 is given when there is only bathymetric coverage. A classification of 3 is given when there is only radar coverage. Finally, a classification of 4 is given for when there are neither sufficient bathymetry nor radar data for a particular glacier standstill. For this study, we restricted our analysis to glaciers that are classified as 1 through 3 and note that most glaciers with long-term standstills do not have bathymetry surveys in the fjords (classified as 4).

Together, these three factors provide a population of glaciers with sufficient terminus and bed topographic data and a range of dynamic behavior (Supp. Table 3.6). We find that 157 glaciers have adequate terminus trace data. Of these glaciers, 96 also have adequate bed topography (classified as 1 or 2). Of these 96 glaciers, we retain 9 glaciers that remained stable throughout the time period and 31 that experienced some retreat, resulting in an examination of a total of 40 glaciers in this study. Glacier 112 is the only glacier we retain with a classification of 3 to increase the population of stable glaciers. We disregard 56 additional glaciers with adequate data because they either did not have long-term stability before retreat that could be identified from the terminus data, high bed data error, or were floating (Supp. Table 3.6).

3.2.2 Glacier Properties

In order to compare across this diverse population of glaciers, we also examine glacier dynamic properties for each glacier to determine whether they might play a role in controlling terminus behavior. We used the mean ice thickness and terminus velocity between 2000-2019 for each glacier from *King et al.* (2020) who derived data from a combination of AeroDEM, ASTER, ArcticDEM, and BedMachineV3 data, surface velocity from Landsat and TerraSAR/TanDEM-X InSAR data. They also computed ice discharge as a combination of ice thickness and velocity at a flux gate upstream of the terminus. Finally, we calculate the height of the glacier terminus above buoyancy (H_{ab}) following *van der Veen* (1996),

$$H_{ab} = H - \frac{\rho_{sw}}{\rho_i} D$$

where D is the fjord depth below mean sea level, H is the ice thickness, ρ_{sw} is the density of seawater, and ρ_i the density of ice. We use the 1985-1987 AeroDEM (*Korsgaard et al.*, 2016) with vertical accuracy of ~ 6 m for surface elevation, BedMachineV4 for bed elevation and ice thickness, a seawater density of 1023.6 kg/m^3 and an ice density of 917 kg/m^3 . We used the geoid height included with BedMachineV4 to convert to heights referenced to the WGS84 ellipsoid. We resampled the AeroDEM to 150 m to match the resolution of the BedMachineV4 data. We compute H_{ab} within ~ 2 km of the terminus across the entire terminus trace that aligns with the DEM locally

and take the median value to get a single value per glacier. We define glaciers with a median value of <50 m H_{ab} as “floating” and those with >50 m H_{ab} as “grounded”.

3.2.3 Identifying Standstills

We identify standstills in the terminus trace record using the long-term average terminus position and examining where the terminus position does not retreat more than it had in the previous two or more summers. Conversely, we define the terminus as being in a state of active retreat when we observe more retreat in a given year than in the previous two summers. For simplicity, we ignore glacier advance by labeling these termini as standstills. We use these definitions of standstill and retreat to label individual glacier terminus traces (e.g., Figs. 3.1, 3.2). We then identify longer-term periods of stability where there are >5 years of consecutive terminus traces that are classified as in standstill. If the standstill was transient (the glacier subsequently retreated from this location during the observational period), we term this a “transient standstill”. If the glacier never moved from the standstill during the observational period, we term this a “persistent standstill”. Finally, many glaciers have more than one standstill location because they retreated after a period of stability (transient standstill) and then restabilized at a new location further up-glacier. We term these new standstills where glaciers restabilized “restabilizing standstills”. This additional classification also expands the number of standstills where the terminus remains stable, providing an additional eight

examples to this population (although they are distinguished in our results).

3.2.4 Bed Morphology at Standstills

With these standstill locations and types identified, we then extract the properties of the bed at each standstill location. First, we determine if there are positive topographic features present at the standstill compared to the surrounding topography (Fig. 3.1 A, D, G). Bed features are manually delineated in QGIS (*QGIS Development Team, 2022*) to determine their extent using a combination of elevation contours from the bed topography map and slope breaks based on a directional slope map for each glacier. Directional slope is a method that calculates the slope of a surface in a user-defined direction (*Zevenbergen and Thorne, 1987; Neteler and Mitasova, 2013*). We used the Directional Slope Plug-in in QGIS (*Alberti, 2018*) to determine the directional slope of the BedMachineV4 topography data in the direction of ice flow for each glacier using

$$\alpha_D = \arctan \left[\frac{dz}{dx} \sin\alpha + \frac{dz}{dy} \cos\alpha \right]$$

where α_D represents the directional slope, α is the angle at which we calculate the slope direction relative to the fjord walls. The directional gradients are derived at each pixel in the elevation data following *Zevenbergen and Thorne (1987)*,

$$\frac{dz}{dx} = \frac{(i, j + 1) - (i, j + 1)}{2S}$$

$$\frac{dz}{dy} = \frac{(i-1, j) - (i+1, j)}{2S}$$

where (i, j) are row and column indexes of the center of a 3x3 kernel and S is the pixel size. To determine α for each pixel, we create a grid at each glacier where each pixel in the grid has a value that indicates an angle of ice flow direction. To create this grid, at least three flow lines are drawn in the direction of ice flow along the bed topography following the fjord walls. We then interpolate points 150 m along the line to determine the angle between each point. These points are then interpolated onto a 150 m grid using nearest neighbor interpolation. The directional slope is calculated using this grid creating maps of directional slope for each glacier (e.g., Fig. 3.1 B, E, H). We also extract the mean directional slope at each terminus trace by interpolating 150 m points along each trace, sampling the directional slope, then taking the mean slope across that trace. This is useful over using the maximum slope as it allows us to identify where positive and retrograde bed slopes occur in the general direction of ice flow. The edge of bed features are generally located where the prograde/retrograde side of the feature approaches zero (e.g. Fig. 3.1 B), or where the contours show a valley, or topographic low or flattening (e.g. Fig. 3.1 E).

There are some cases where there are no discernible positive bed features in the locations of standstills. There are also standstills with more than one positive bed feature present. To simplify our analysis we only categorize the most prominent feature that is impacting glacier termini at the initial

standstill. This is often evident through examination of the map-view pattern of terminus retreat over the bed feature. For example, Fig.3.1B shows a smaller positive bed feature located just northeast of the feature of interest but we do not examine this feature as the glacier terminus does not appear to be impacted by it.

3.2.5 Characterizing Standstill Features

Using the map-view areal extent of bed features at standstills we compute several morphological properties from the bed topographic data within the extent. First, we distinguish between the prograde (fjord-facing) and retrograde (glacier-facing) sides of bed features using the location of the zero contour of the directional slope, located on the crest of the feature. We take the mean of all pixels in each of the areas defined as the prograde and retrograde sides of each bed feature to compute the mean prograde and retrograde bed slopes. Second, we locate the peak of each feature by taking the minima of the slope (1st derivative) of the bed topography. As we are attempting to isolate the peak outside of the fjord walls, we cannot simply take the max height of the bed topography as this will identify the higher elevation fjord walls. The slope will approach zero when topography at a local minima or maxima, or at a peak or valley. Features that are simple bumps will be straightforward as peak will be defined where the crest of the feature is clearly located (Fig. 3.2I). For features that connect to fjord walls or may be elongated laterally, many minima may be located along the crest of the feature, therefore we take

the mean location of all minima located along the crest. We then snap the location of this initial peak to closest point on the zero directional slope contour (i.e. crest of the feature) and this is where we define the bed peak. This is useful in cases where the along flow profile of our feature has a clear peak, but the across-flow profile is at a minimum in the fjord (Fig. 3.2). We identify a peak in order to compare between features and the location of the terminus to a central location. Third, we use the areal extent to determine both the across-flow and along-flow feature lengths. Fourth, we compute the percentage of the cross-sectional fjord area that the feature takes up in two-dimensions using the across-fjord length as a percentage of the total fjord width. Finally, we calculate the centroid of each terminus trace using the Shapely centroid method in Python (*Gillies, 2013*). The terminus centroid gives us an average terminus position in map-view that can be used to quantify the distance between the terminus and the peak of the bed feature present over time. We compute the distance between the bed peak and the terminus centroid and then label the distance as either down-fjord of the bed peak or up-fjord of the bed peak if the terminus centroid falls on the down-fjord or up-fjord side of a line across-fjord at the location of the bed peak. Since the bed peak does not always line up with the terminus centroid, the distance between the two is a minimum (but perhaps not zero) when the centroid is closest to the bed peak. For retreating glaciers, we calculate the mean distance between the terminus centroid and the bed peak before the onset of retreat and for stable glaciers, we take the mean of the entire record.

Since the location of bed features may be controlled by the lithology of the bedrock due to differential erosion related to material strength, we examine bedrock geology of the fjord walls adjacent to identified standstills. Geologic information is provided by *Harrison et al.* (2011) and found in the QGreenland QGIS package (*Moon et al.*, 2022). For simplicity we categorize geology into three generalized types based on their erodibility; 1) crystalline rocks that include either metamorphic or volcanic intrusive facies; 2) sedimentary facies that include both carbonate and sedimentary rocks; and 3) varied lithology, which reflects a combination of sedimentary and volcanic facies. Additionally, we identify contacts between these three geologic rock types to determine if they are aligned with standstill locations. While we recognize that this analysis over-simplifies the complex geology of Greenland, our goal is to broadly identify correlation between lithology and standstills.

Finally, we also explore how the terminus behaves as it interacts with the bed feature by examining if the terminus sits mostly on the prograde or retrograde side of the bed feature, or if it oscillates between the two sides. To do this we first compute the centroid of each terminus trace in the raw terminus data. Then, we measure the distance between the terminus centroid and the peak of the bed feature we are interested in. We then examine the directional slope at each terminus trace as it approaches (and potentially retreats past) the bed feature of interest. Across both retreating and stable glacier populations, we find three general patterns in how glacier termini interact with bed slope as the termini approach peaks in bed topography; Mode 1) termini remain

primarily on the retrograde side; Mode 2) termini remain primarily on the prograde side or; Mode 3) termini oscillate between retrograde and prograde sides of the bed peak (Fig. 3.3). For transient standstills, this is the mean distance from the peak before the onset of retreat. For persistent standstills, this is the mean distance over the study period.

3.3 Results

3.3.1 Glacier and Fjord Characteristics

Our population of 40 glaciers reside in the North West, Central West, and Southeast regions of Greenland (Fig. 3.4). The majority of these glaciers (77%; $n=31$) have experienced at least one large (> 1 km) retreat event during the observational period (1985-2019) while the remaining 9 glaciers (23%) have been stable for the observational period. Of the 31 retreating glaciers, 16 of them (51%) restabilized at some point upstream of the of the first standstill, while the remaining 15 have continued to retreat through the entire observational period. We include 8 of the 16 restabilized glaciers in this analysis as they have sufficient bathymetry and/or radar at the new standstill location.

We find no significant differences in ice thickness or ice discharge between the stable glacier population (mean $H=355\pm 144$ m; mean $D=2.1\pm 3.1$ GT/yr) and the retreat glacier population (mean $H=344\pm 141.3$ m; mean $D=2.0\pm 2.2$ GT/yr; Tables 3.1, 3.2; Fig. 3.5). However, because 28% of retreating glaciers are near flotation at their termini (Fig. 3.5), the mean height above buoyancy for retreating glaciers (75 ± 42 m) is significantly lower than

that for stable glaciers ($135 \text{ m} \pm 61 \text{ m}$; $t(10.3) = -2.7$, $p = 0.02$). Finally, we find no significant differences in fjord lithology between stable and retreating glaciers, however, we do find that 30% of standstill locations are located in areas with geologic contacts (Fig. 3.6).

3.3.2 Bed Morphology at Standstills

All but two of the 40 glaciers have bed features present (95%; Fig. 3.4). Fjords without bed features are restricted to the South Eastern coast of Greenland. We classify the bed features found at standstills into three categories depending on their overall morphology: moraines, benches, and ridges. Moraines are identified when the bed has an along-fjord topographic high that is uniform across-fjord within a range of $\sim 50\%$ of the across-fjord length (e.g., Figs. 3.1G-I and 3.2C). Ridges are identified as bed features with an isolated high near the center of the fjord in both the across- and along-fjord directions. Thus, across-fjord bed topography for ridges has a characteristic 'W' shape with minima between the ridge and the fjord walls (e.g., Figs. 3.1D-F and 3.2B). Ridges are the most difficult to identify because of the influence of fjord walls and there is a high degree of variability in ridge shape. The majority of ridges (5 out of 6) are found in fjords with an upstream convergence of two glaciers that were once tributaries to a central, larger glacier (Fig. 3.1D-F). Finally, we define benches as bed features with an along-fjord topographic high that lies along only one side of the fjord, providing a characteristic bench-shape in the across-fjord direction (e.g., Figs. 3.1A-C and 3.2A). For all fjords studied

here, moraines are the most common feature type (57% of fjords), followed by benches (22%), ridges (15%), and then no feature (5%) (Fig. 3.4). There is a weak correlation between bedrock type and feature type. For example, bench features are only found in fjords bounded by crystalline lithology, while ridges and moraines have more variable lithology bounding those standstill locations (Fig. 3.6).

3.3.3 Terminus Behavior at Standstills

In addition to categorizing bed morphology at glacier standstills, we also examine how the terminus behaved for each type of standstill identified. We acknowledge that Greenland Ice Sheet glaciers have been retreating since the Little Ice Age, and thus categorize the standstills at termini that did not retreat during the observational period as “persistent standstills.” Further, we categorize standstills that termini retreated from during the observational period as “transient standstills.” Finally, “restabilizing standstills” are standstills that caused retreating termini to restabilize during the observational period. Of the 40 glaciers in our study, 31 of them retreated from transient standstills, 8 restabilized at restabilizing standstills, and 9 never retreated (persistent standstills). This gives us a total of 48 standstills. Glaciers with transient standstills have the most heterogeneity in bed morphology at the standstill (Fig. 3.7); 48% are moraines, 26% are benches, 19% are ridges and 6% have no discernible bed feature present at the transient standstill. For both restabilizing standstills and persistent standstills we find only bench and

moraine bed features present (Fig. 3.4), with more moraines at persistent standstill locations (89%) compared to restabilizing standstills (75%) (Fig. 3.7).

In addition to differences in morphology, different standstill types appear to influence the position of the glacier terminus. At transient standstills (where termini retreated from), termini are more likely to be located on the retrograde side of the bed feature present before retreat. Of the 31 glaciers that retreated from standstills, 29 of them have bed features at the transient standstill identified in the fjord. Of these 29, 18 (62%) of these had termini that were either entirely on the retrograde side of the bed feature (Mode 2: n=8, 28%) or oscillating into the retrograde side periodically (Mode 3: n=9, 31%; Fig. 3.3, Table 3.5). This is markedly different for persistent standstills, which were more likely to have termini grounded on the prograde side of bed features present in these locations (Mode 1: n=6, 67%) or oscillating regularly across the peak in bed topography (Mode 3: n=3, 33%; Fig. 3.3, Table 3.5). In addition, when glaciers retreat from transient standstill locations they tend to have a larger range in distance between the terminus centroid and the bed feature peak before retreat when compared to glaciers that remain stable at persistent standstill locations, where the terminus centroid is typically very close to the bed feature peak (Fig. 3.8). The one outlier for the stable glacier population here is Glacier 33, which has a very large stabilizing moraine, therefore the peak is very far from the termini. Finally, we also observe variations in retreat style as termini retreat from transient standstills of various mor-

phologies. Out of all 40 glaciers, approximately 23 (57%) experience terminus change that is greater on one side of the terminus than another, which we term 'swinging door' retreat (Fig. 3.9). This definition can be quantified as a style of retreat where approximately 50% of the terminus on a single date is greater on one side of the terminus than the other (Fig. 3.9).

3.3.4 Bed Feature Properties at Standstills

For each standstill population (transient, persistent, and restablizing) we examine a suite of bed properties associated with the bed feature at the standstill location (where available). We find significant differences in the mean prograde slope between bed features across standstill type. Transient standstills have bed features with smaller prograde slopes ($4.4 \pm 2.6^\circ$) than those found at both persistent ($8.1 \pm 3.4^\circ$; Table 3.3) and restablizing standstills ($6.9 \pm 1.9^\circ$; Table 3.4). We do not find significant differences in the mean retrograde slope of bed features across standstill type. For example, transient standstills have bed features with only slightly smaller retrograde slopes of $3.7 \pm 2.7^\circ$, compared to those at persistent ($5.1 \pm 4.1^\circ$), or restablizing standstills ($4.7 \pm 2.1^\circ$; Tables 3.3, 3.4). Examining within the population of transient standstills, there is no significant difference in bed slope (either prograde or retrograde) between ridges, benches, and moraines (Fig. 3.7). However, within the persistent and restablizing standstill populations, we find that benches have steeper prograde and retrograde slopes than moraines (Fig. 3.7), although there are markedly smaller populations of benches available for analysis.

We examine other properties of bed features at standstills including the percent of the total fjord cross-sectional area that the bed feature occupies, the depth below sea level to the peak of the bed feature, the along-flow length of the bed feature, and the map-view area of the bed feature (Fig. 3.10). Similar to slope values, we find significant differences in the sizes of bed features across transient, persistent, and restablizing standstills. Transient standstills have bed features with a large range in values of % fjord occupied with a mean of $73\pm 29\%$. This value is significantly different when compared to bed features at persistent standstills ($96\pm 11\%$) and bed features at restablizing standstills ($89\pm 21\%$). This is expected because transient standstills have bed features that are more likely to be either ridge or bench type in their morphology, both of which are inherently smaller bed features than moraines.

The mean depth (in m below sea level) of the peak of bed features is also significantly different between those found at transient standstills and persistent standstills, but not between those found at transient and restablizing standstills because of the large range found across each of these populations (Fig. 3.10D, Table 3.3, 3.4). We find that bed features at persistent standstills have significantly shallower peak heights on average (-61 ± 107 m) compared to those at transient standstills (-174 ± 193 m) or restablizing standstills (15 ± 302 m) (Fig. 3.10D, Table 3.3, 3.4). We find additional subtle morphological differences across bed features including area and along-fjord length, however none of these differences are significant (Fig. 3.10, Tables 3.3, 3.4).

3.4 Discussion

Glacier bed/fjord topography is complex and heterogeneous between fjords making it challenging to elucidate how glacier termini are influenced by bed topography. We use the simple approach of examining the topography right at the terminus during periods of standstill and find that most glaciers have bed topographic features present at standstills with only two out of our forty glacier standstills having no bed topographic feature present. This is not a new finding as the presence of paleo-morainial features are ubiquitous in paleo-glaciological studies and are used to infer standstill conditions at these locations (*Winkelmann et al.*, 2010; *Batchelor et al.*, 2019; *Arndt et al.*, 2015). However, knowing the state of the glacier during its interaction with each bed feature gives us unique perspective into the specific properties of a bed feature that may be important in controlling how the glacier responds to that feature. One caveat of this is that we only have topography data after glacier retreat and do not know the state of the bed before the glacier terminus was in that location. Thus, it is impossible to know if the topography is influencing the glacier dynamic behavior or if the glacier dynamic behavior is influencing the topography. For example, stable glaciers may be more able to build bed features with that are larger and have steeper slopes because of their persistence at a constant location. We also find that the retreat population of glaciers are more commonly floating or near floatation at their termini, which may contribute to their prevalence for retreat and their ability to build buttressing bed features. Despite these caveats, we find key differences in bed features across

our population of standstill types permitting development of a classification of feature by morphology (Fig. 3.4).

When we examine the bed features at standstills and compare feature properties across populations of glaciers that retreated compared to those that did not, we find that the most prominent factors that correlate to glacier state are the prograde bed slope, location of the terminus on the prograde part of the bed feature, feature type, and feature size (% fjord and peak depth). Stable and restablizing standstills are more likely to have moraines over ridges and benches. Further, because moraines (by definition) extend across the entire fjord they tend to occupy a greater percentage of the fjord cross sectional area than other feature types. Thus, because stable and restablizing glacier populations are composed more of moraine-type features, we see moderate correlation between glacier state at the standstill and the fjord cross sectional area of a feature; larger bed features are present at persistent and restablizing standstills. For restablizing glacier populations, there are some bed features that are now above sea level suggesting that restabilization of the terminus occurred as a result of the glacier becoming decoupled from the ocean (Fig. 3.10D). We also find that the prograde bed slope is correlated to glacier state with prograde bed slopes up to 4 degrees steeper for glaciers that are stable or have restablized compared to those experiencing retreat.

Previous model studies suggest that the retrograde bed slope is critical for determining if glaciers persist at a standstills with steeper retrograde bed slopes responsible for longer term persistence (*Robel et al., 2022*). Our ret-

prograde bed slope data exhibits considerable range for the stable and retreat glacier populations making it difficult to draw similar conclusions to *Robel et al.* (2022). This may be a consequence of the differences in data coverage upstream of glacier termini where we often rely on single along-flow radar flights to determine bed geometry. If we assume that the prograde bed slope scales with the retrograde bed slope, which seems true on average (Fig. 3.10A, B), we can use prograde bed slope as an approximation for retrograde bed slope in order to interrogate differences in the duration of glacier standstills. We see general correlation between prograde bed slope and glacier stability (as discussed above), but we also see hints of correlation between prograde bed slope and the timing of retreat. While most glaciers retreated in the late 1990s/early 2000s, Glacier 171 retreated much later than the general population of retreat glaciers (in 2016), and has the steepest prograde bed slope across all standstill features in the retreating glacier population (12° ; Fig. 3.10A).

In addition to feature type, size, and prograde bed slope, we also find that stable and restablized glaciers have their termini more often situated down-fjord of the bed feature prior to retreat (thus are on the prograde bed slope). This confirms prior research suggesting that glaciers grounded on prograde bed slopes can remain persistent (*Motyka et al.*, 2017; *Carr et al.*, 2015; *Millan et al.*, 2018; *Catania et al.*, 2018; *Bunce et al.*, 2018) likely because ice flux increases downstream of the bed peak (*Robel et al.*, 2022). Indeed, because stable glaciers tend to have higher prograde bed slopes this may keep them from retreating to the retrograde part of the bed feature. However,

simply having termini grounded on retrograde bed slopes is not sufficient to initiate retreat because we find many glaciers at persistent standstill that are regularly grounded on the retrograde part of the bed feature. This suggests that topography alone does not control retreat but topography may prime a glacier to experience retreat if it experiences a perturbation to the climate system that permits it to remain at standstill (*Millan et al.*, 2018; *Catania et al.*, 2018; *Bunce et al.*, 2018). Similar conclusions were found in a recent study by *Christian et al.* (2022) who found that glacier termini that were downstream, but closer to their bed peaks were more likely to retreat into regions of the bed with retrograde bed slopes. Therefore, the stable glaciers that tend to oscillate are likely to retreat with future climate warming.

The style of retreat (its pattern in map-view) is also correlated to feature type. Because they do not occupy the entire fjord width, bench and ridge feature types tend to more commonly produce a “swinging door” retreat style (Fig. 3.9) where the retreat rate is slower where it is in contact with the bed feature and faster elsewhere. Examination of ice-ocean thermal forcing suggests that glacier termini at depths of 200 m or more are at a greater risk of retreat due to ocean warming (*Wood et al.*, 2021a; *Straneo and Heimbach*, 2013; *Holland et al.*, 2008; *Rignot et al.*, 2016b). Thus, one mechanism for the swinging door retreat style may simply be exposure of the deeper parts of the terminus to warmer ocean waters. Further, the more a terminus deviates from a straight line over variable topography, there is an increase in the submerged area of the front, which when combined with higher ice flux, is known to cor-

relate with retreat (*Frank et al.*, 2022). Swinging door retreat style may also result because of the steeper bed slopes experienced by the terminus where it is in contact with the bench (Fig. 3.1). A reason for this may be because the parts of the termini grounded at deeper depths may approach flotation conditions permitting large-scale full-thickness calving events to dominate calving style here. Calving styles that vary across glacier termini are not currently captured in ice sheet models (*van Dongen et al.*, 2021; *Amaral et al.*, 2019), but may be helpful to reproduce the observed terminus position with time.

While we find some clear relationships between bed feature type and morphology to glacier state there are several shortcomings to this study. First, inferring long term stability (>100 years) is more difficult given that our observational period only covers ~ 40 years. This is particularly true for our conclusions regarding the restabilizing population of glaciers because they have only remained at these standstills for short periods of time (mean of ~ 7.5 years). Our results are further limited because of the small sample size of stable glaciers compared to the size of the retreating glacier population. Further, because stable glaciers have not retreated from a current bed feature, they are more likely to be under-sampled in terms of bathymetry. We also do not include glaciers that do not exhibit a more complex pattern of terminus change than those discussed here (persistent, transient, restabilizing). For example, a glacier may be present at a standstill feature, however the terminus change record could be highly variable and therefore inferring a single period of stability and retreat is non-trivial. The low resolution of the BedMachine

topography product may be obscuring some details of the features we have identified and we also do not account for the impact of bed features found downstream of glacier termini. Prior work suggests that the overall depth and shape of the fjord influences its connection to warm waters on the continental shelf and how these warm waters might reach glacier termini (*Slater et al.*, 2022; *Carroll et al.*, 2016). Further, the shape of the fjord can influence circulation within the fjords (*Slater et al.*, 2018) and the export of calved icebergs, which can create melange-choked fjords that impact calving (*Amundson et al.*, 2010; *Cassotto et al.*, 2015; *Robel*, 2017).

3.5 Conclusions

In this study, we examine the morphological variability across bed topographic features where glaciers have experienced standstills (persistent and transient). Our work suggests that some of the glacier-to-glacier heterogeneity in retreat style, timing, and rate may be related to differences in bed slope, terminus position on that bed slope, and feature type present in the fjord. We also find that retreating glaciers were more commonly floating or near flotation at their termini before retreat suggesting that they may not be able to produce the same types of features as found at termini that are fully grounded. Future studies integrating the impact of bed topography on transient and persistent stability with studies of ice melange, submarine discharge, flotation, and terminus shape will further aid in understanding the mechanisms behind complex heterogeneous changes at marine-terminating glaciers in Greenland.

This study also highlights the need for more high-resolution ice-penetrating radar surveys of the terminus region of glaciers, particularly at persistent termini, in order to capture the complex geometries of stability points.

Glacier ID	Onset Date	Terminus change 1985-2019 (km)	Ice Discharge 2000-19 (GT/yr)	Thickness 2000-19 (m)	Velocity 2000-19 (m/yr)	Hab 1985 (m)
2	2002.5	4.4	1.25	486.5	537.5	65
3	2003.2	-8.5	0.62	261.0	761.4	34
7	1997.7	-5.0	5.80	334.0	887.2	29
19	1998.7	-1.1	0.08	169.7	119.5	98
22	1985.7	-6.7	0.92	383.7	132.6	42
29	1985.2	-3.2	3.09	304.1	531.8	56
32	1998.6	-5.2	3.98	385.2	1457.2	70
35	2010.6	-2.2	1.48	372.2	467.3	74
44	2000.2	-1.5	0.66	246.4	796.5	16
49	1997.7	-4.2	1.28	395.5	579.0	25
54	1998.3	-2.2	0.73	301.9	757.3	26
58	1998.6	-1.1 (1989)				86
61	1997.7	-4.2 (1989)	0.73	227.4	267.7	44
63	1999.5	-1.3 (1988)	0.07	102.0	125.6	83
65	1999.7	-4.3 (1988)	0.43	237.3	300.6	23
73	1999.5	-6.9 (1986)	1.65	370.8	1067.7	-12
77	2008.5	-1.2 (1986)	0.11	129.0	261.1	56
171	2016.1	-1.9	3.76	874.5	861.6	131
210	2001.6	-2.3	5.15	357.6	791.9	112
213	2000.7	-2.7	0.56	220.7	422.4	137
231	2000.7	-4.3 (1992)	8.09	569.7	1181.9	94
233	1997.2	-5.9 (1992)	2.65	418.5	1691.5	82
247	1996.4	-3.1 (1992)	5.10	433.2	1891.9	87
248	1999.6	-1.0 (1996)	0.88	435.8	727.1	193
252	2001.6	-2.7 (1992)	1.71	393.0	828.9	91
280	1998.6	-1.9	0.53	363.6	389.7	131
281	2001.8	-2.4	1.29	343.2	768.5	78
282	1998.2	-0.3	7.14	368.3	2059.6	100
285	1998.6	-1.5	0.18	295.4	259.5	100
289	2000.3	-3.2	0.62	323.6	471.5	85
290	2001.2	-1.2	0.11	220.2	224.1	108
Mean		-2.86	2.02	344.1	720.7	76
STD		2.37	2.19	141.3	502.8	42

Table 3.1: Glaciers with standstills defined as 'transient' for this study. Retreat estimates are the difference between 1985-2019 terminus positions derived from TermPicks and CALFIN datasets. Mean ice discharge, thickness, and velocity estimates between 2000-2019 are derived from King et al. 2020. The H_{ab} values are median values from within ~ 2 km of the terminus of the AeroDEM in 1985.

Glacier ID	Terminus change 1985-2019 (km)	Ice Discharge 2000-19 (GT/yr)	Thickness 2000-19 (m)	Velocity 2000-19 (m/yr)	Hab 1985 (m)
11	-0.13	1.19	423.6	612.8	77
33	-0.09	0.72	318.6	278.3	270
112	0.08	0.25	120.1	588.4	95
227	0.15 (1992)	0.13	217.2	364.0	162
229	0.12 (1992)	1.17	203.2	1791.3	135
264	0.28 (1992)	3.68	496.8	1699.7	122
284	0.58	9.91	450.6	3395.9	98
287	-0.21	0.63	485.4	412.0	175
291	-0.06	2.22	483.7	757.3	83
Mean	0.08	2.21	355.5	1100.0	135
STD	0.23	2.91	135.8	967.0	58

Table 3.2: Glaciers with standstills defined as "persistent" for this study. Retreat estimates are the difference between the 1985-2019 terminus positions derived from the TermPicks and CALFIN datasets. Mean ice discharge, thickness, and velocity estimates between 2000-2019 are derived from King et al. (2020). The H_{ab} values are median values within ~ 2 km of the AeroDEM terminus in 1985.

	t-statistic	p-value
Mean prograde slope	-2.988	0.012
Mean retrograde slope	0.978	0.35
Peak Depth	-5.556	0.020
Along-flow length	-0.471	0.645
Percent of Fjord	-3.434	0.002
Area	-1.076	0.311
Ice Discharge	-0.171	0.867
Thickness	-0.207	0.839
HaF	-2.74	0.02

Table 3.3: Results of the Welch's T tests comparing the mean values of the measurements of transient and persistent standstill features.

	t-statistic	p-value
Mean prograde slope	-3.009	0.009
Mean retrograde slope	1.195	0.251
Peak Depth	-1.722	0.124
Along-flow length	1.058	0.305
Percent of Fjord	-1.677	0.113
Area	-0.761	0.464

Table 3.4: Results of the Welch’s T tests comparing the mean values of the measurements of transient and restablizing standstill features.

	Mode 1	Mode 2	Mode 3
Transient Standstills	11	8	10
Persistent Standstills	6	0	3

Table 3.5: Summary of the mode types for transient and persistent standstills corresponding to the modes shown in Fig. 3.3. Mode 1) termini remain primarily on the retrograde side; Mode 2) termini remain primarily on the prograde side or; Mode 3) termini oscillate between retrograde and prograde sides of the bed peak.

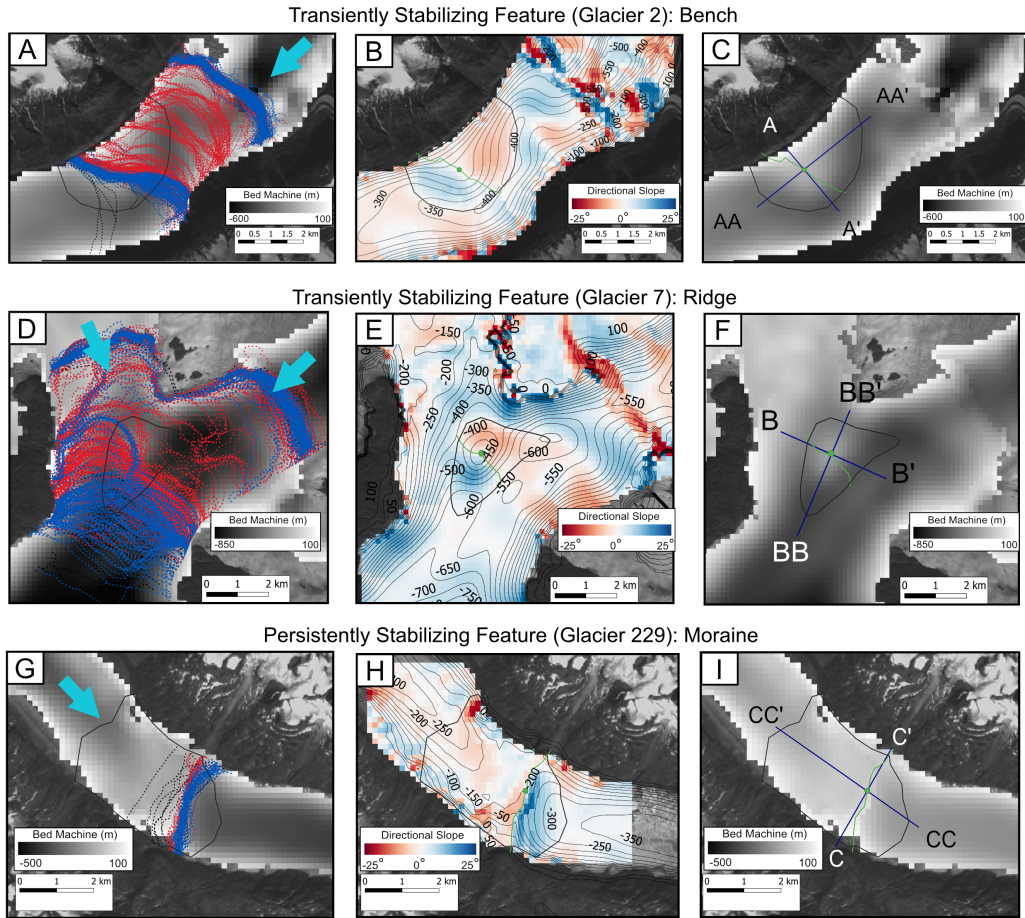


Figure 3.1: **A, D, G:** Terminus traces colored by retreat (red dashed line), standstills (blue dashed line) for Glacier 2, 7, and 229. Black dashed lines indicate times when there was not enough data to define a retreat or standstill. The solid black line delineates the standstill feature. **B,E,H:** Directional slope for each glacier. The solid black line delineates the standstill feature (same as A, D, G) The green circle is the location of the bed peak, and the green line is the location of the split between the prograde and retrograde slope defined by the 0-slope contour. **C,F,I:** The solid black line delineates the standstill feature (same as A, D, G). The blue lines correspond to the transects shown in Fig. 3.2. The base map for all figures labeled A, C, D, F, G, H, I is BedMachine V4.

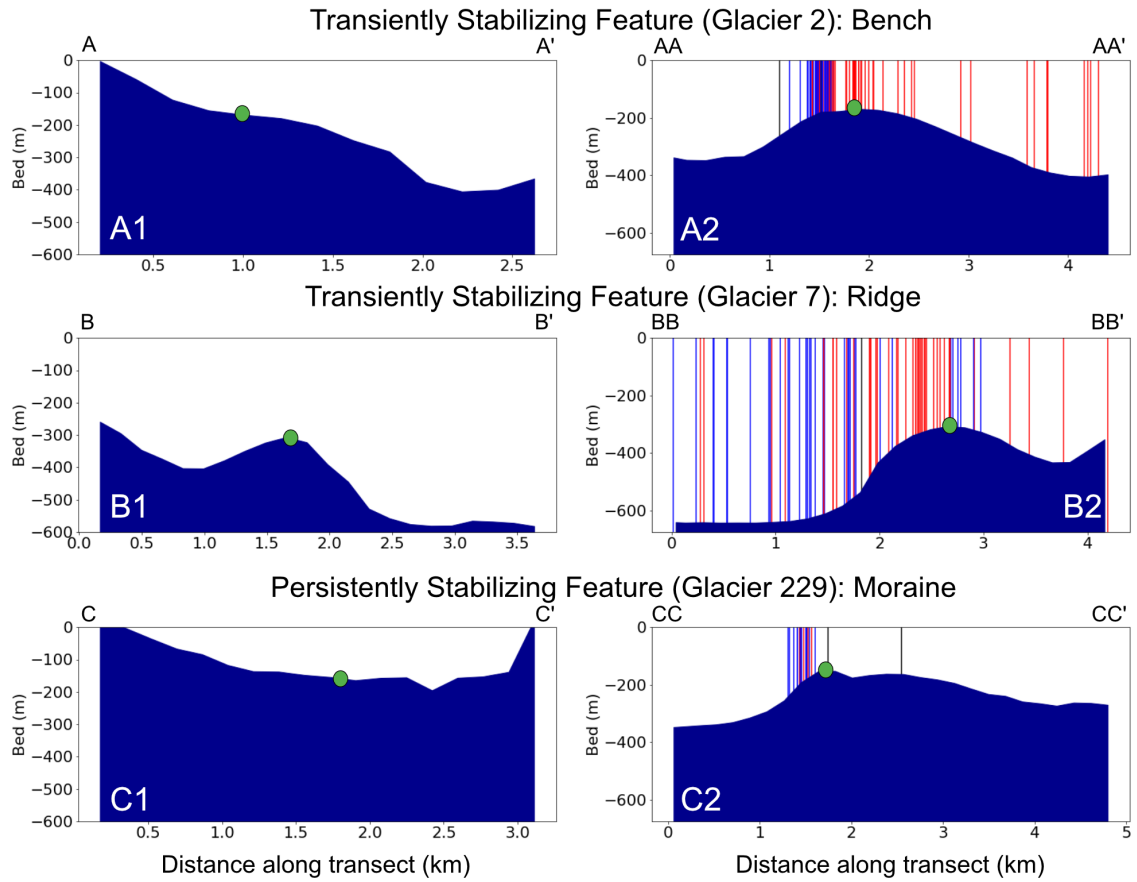


Figure 3.2: Bed features along and across the fjord transects for Glaciers 2, 7, and 229 to demonstrate the different types of features identified. Each transect corresponds to the same location as noted in figures 3.1 B, E, H. The vertical lines in the figures on the right are every fifth terminus colored by standstill(blue) or active retreat (red). The green dot corresponds to the apex location.

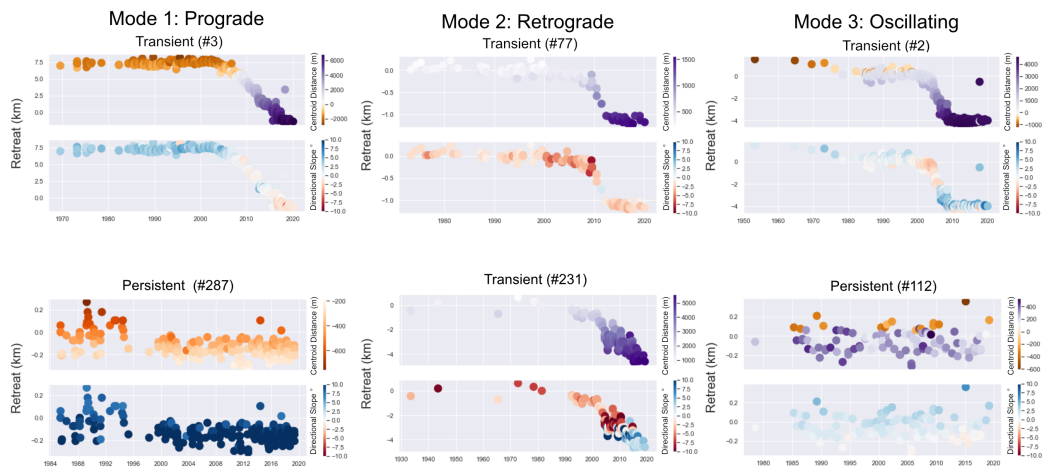


Figure 3.3: Examples of the distance between the terminus (centroid) and the peak of the bed feature compared to the mean directional slope at the terminus for six glaciers. When the centroid distance is negative (orange), the centroid is on the down-glacier side of the peak. When the centroid distance is positive (purple), the centroid is located on the up-glacier side of the peak. The slope is saturated at -10 and 10 to compare the figures.

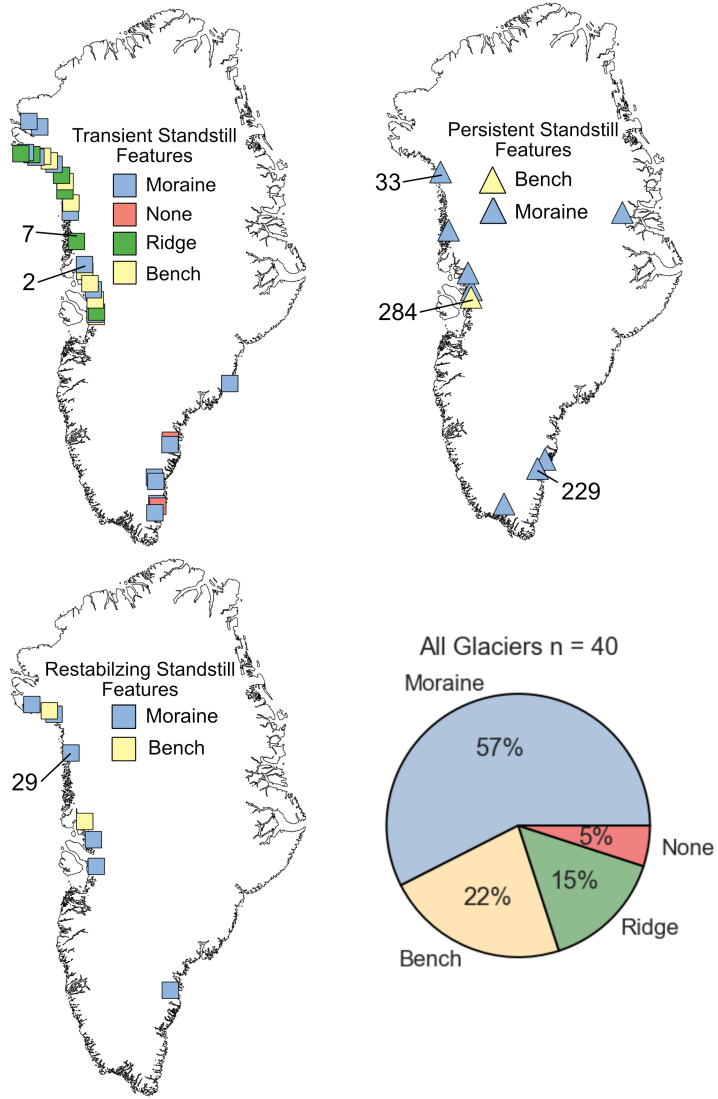


Figure 3.4: Overview of the locations of the standstill features defined in this study. Each map corresponds to the locations of the transient, persistent, and restabilizing standstill features. The pie chart is the distribution of types for the transient and persistent standstill features in this study. The numbers that offshoot from the maps are locations of some glaciers noted in the text.

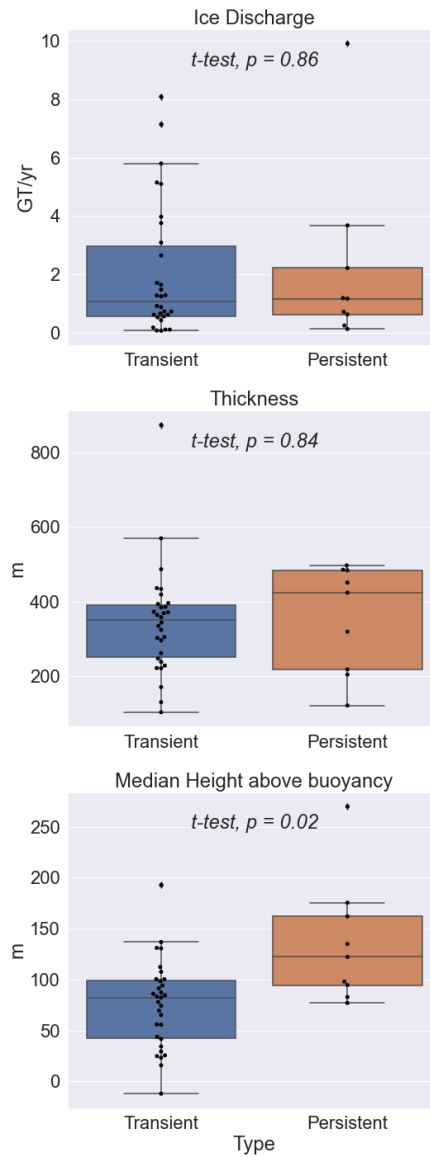


Figure 3.5: Ice discharge, thickness, and median height above buoyancy (H_{ab}) for glaciers with transient and persistent standstills in this study. Ice discharge and thickness data are from *King et al. (2020)*. The H_{ab} is derived from AeroDEM (*Korsgaard et al., 2016*) and BedMachineV4 (*Morlighem et al., 2017*). The t-test values are also reported in Table 3.3

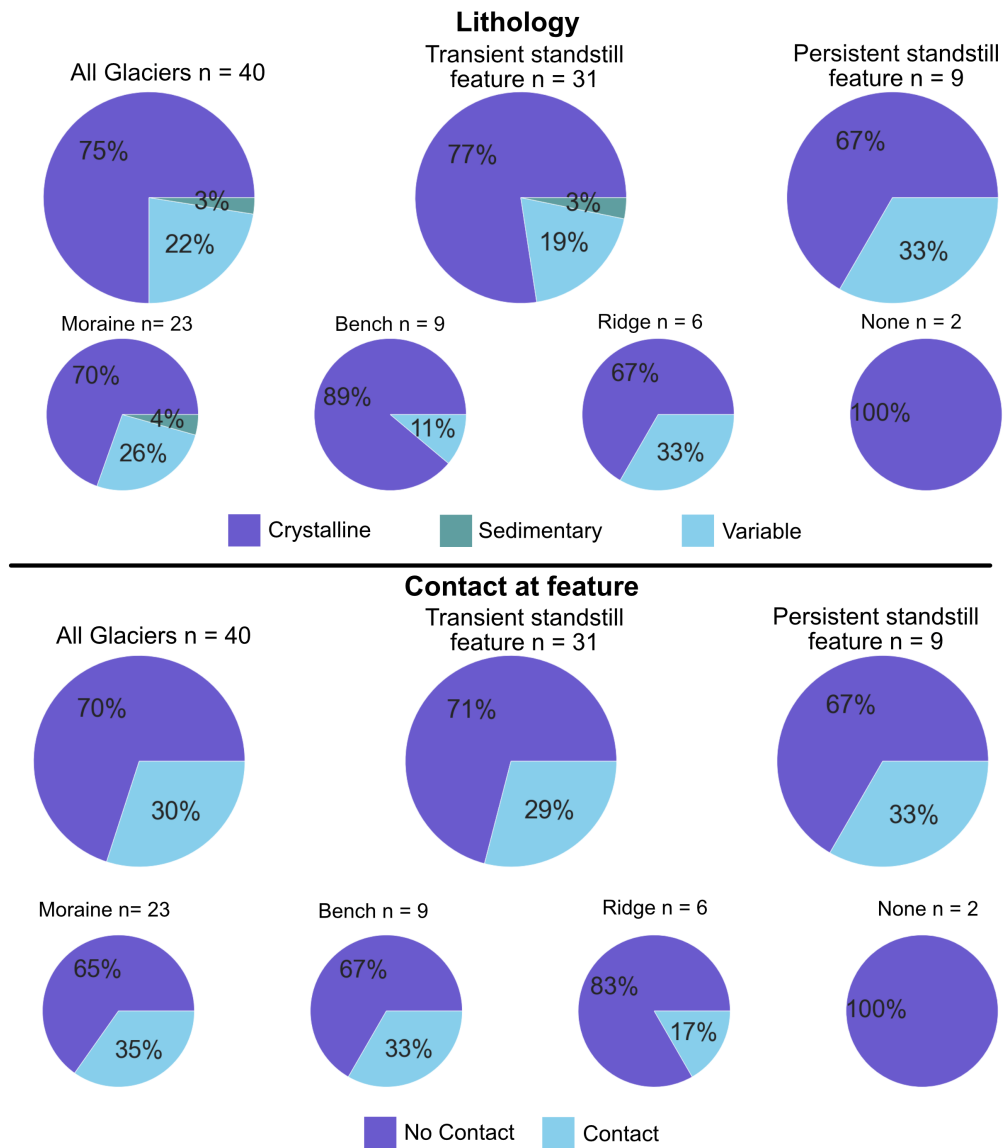


Figure 3.6: Top: Distribution of the lithology by transient and stabilizing standstill features and feature type. Bottom: Distribution of the presence of contact at features by transient and stabilizing standstill features and feature type

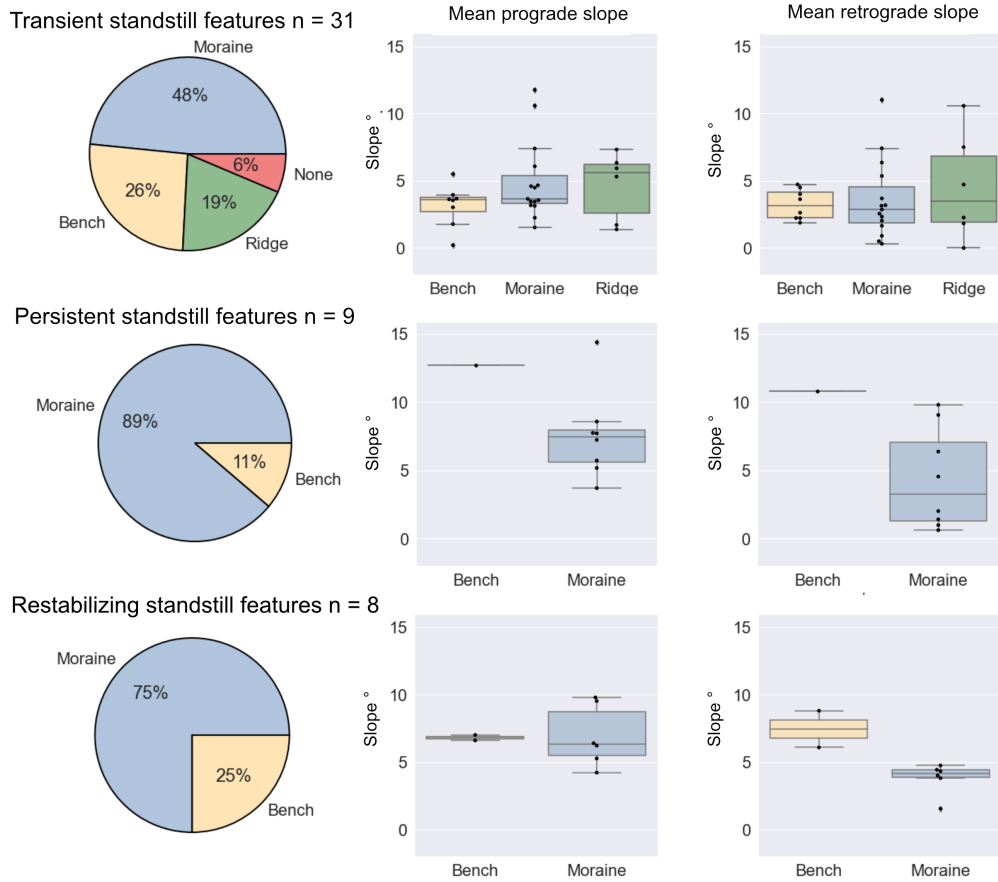


Figure 3.7: Overview of the distribution of the type of feature and mean slopes for the transient, stabilizing, and restabilizing standstill features. Pie charts correspond to the distribution of feature types, whereas box plots show the mean prograde and retrograde slopes for each type. The black dots in the box plots are the raw data used to produce the plots.

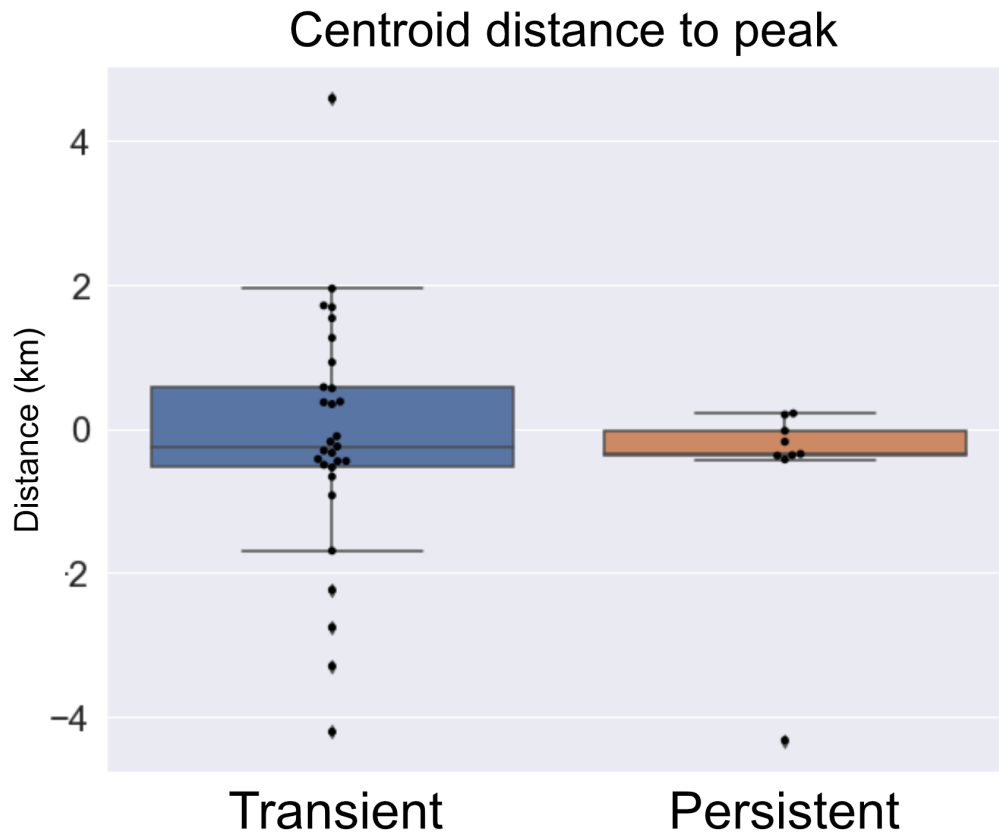


Figure 3.8: The mean distance from the terminus centroid to the peak of a bed feature for different standstill types. For transient standstills, this is the mean distance from the peak before the onset of retreat. For persistent standstills, this is the mean distance over the study period.

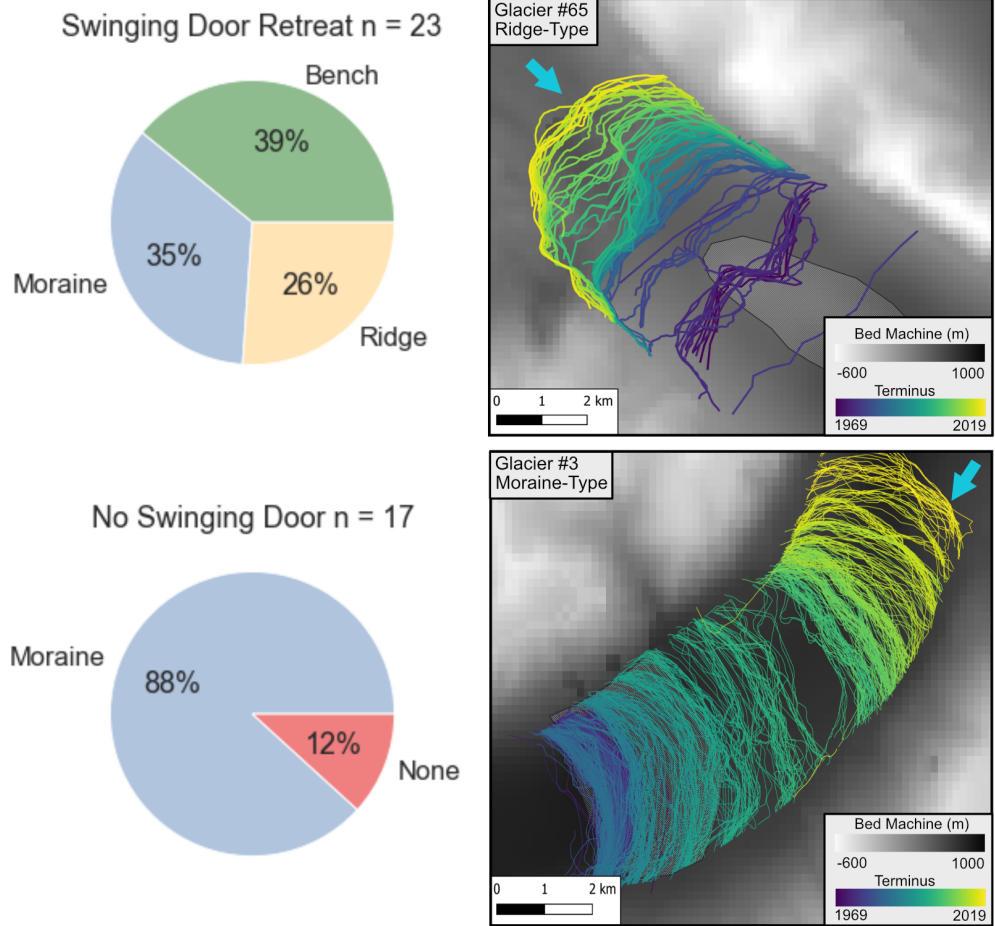


Figure 3.9: Left: Distribution of feature types according to the presence of swinging door retreat. Right: Examples of swinging door retreat at glacier #65 and non-swinging door retreat at glacier #3.

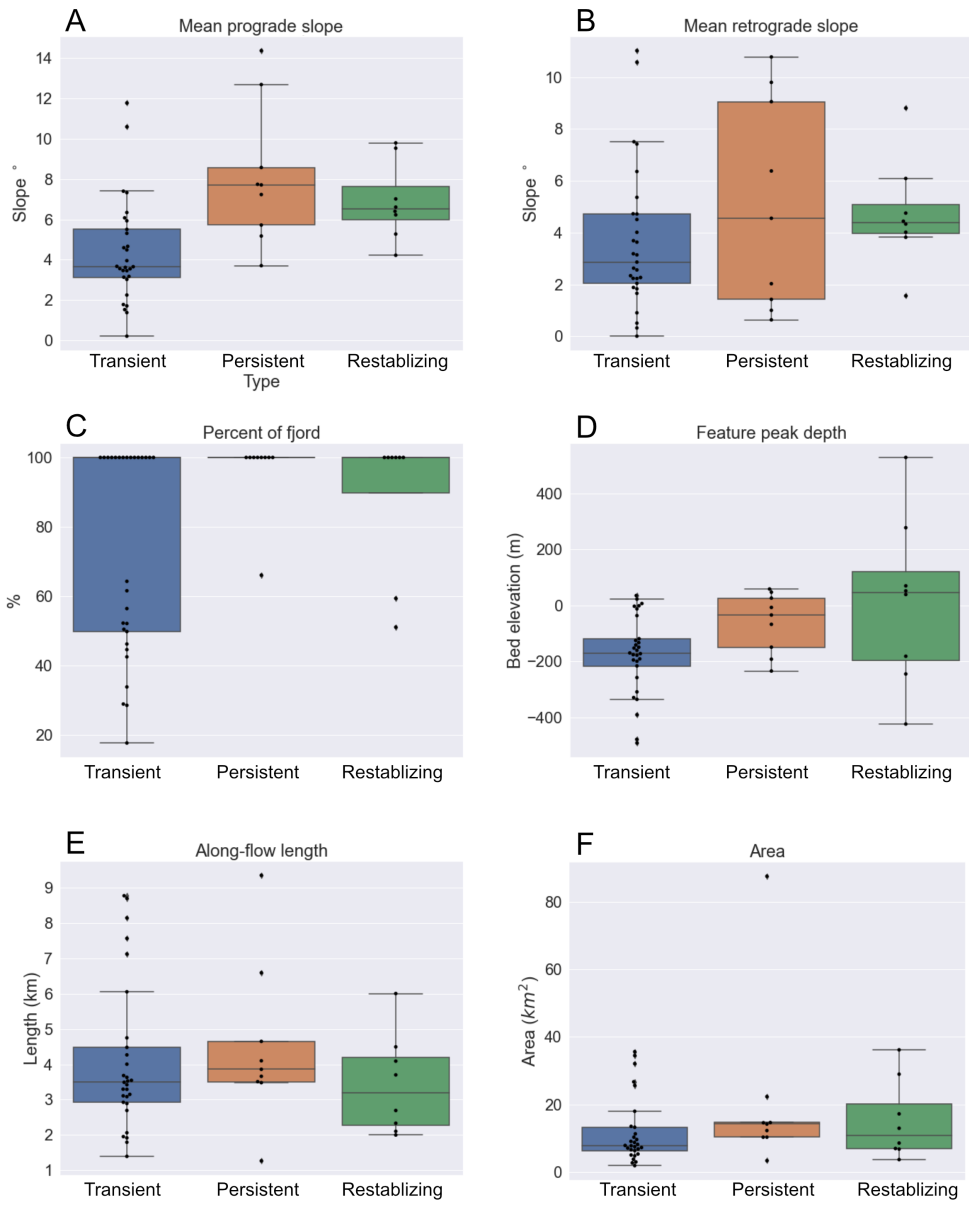


Figure 3.10: Box plots comparing transient, stabilizing, and restablizing standstill features. The black dots in the plot are the raw data used to produce the plots.

3.6 Supplemental Materials

Glacier ID	Coverage	Picks Per Year	Retreat Pattern	Exceptions	Chosen
1	2	22.7	Varied		No
2	1	15.4	Stable-Retreat-Stable		Yes
3	1	16	Stable-Retreat		Yes
4	2	7.2	Retreat		No
5	1	9.3	Retreat		No
6	3	12.3			No
7	1	13.1	Stable-Retreat		Yes
8	2	10.1	Retreat		No
9	4	2.1			No
10	3	6.3			No
11	2	9.2	Stable		Yes
12	4	2.2			No
13	4	9			No
14	3	6.2	Stable-Retreat-Stable		No
15	3	8.1			No
16	1	13	Varied		No
17	2	13.1	Varied		No
18	1	14.3	Varied		No
19	1	10.9	Stable-Retreat		Yes
20	1	16	Stable-Retreat	Bed data error	No
21	3	14	Stable-Retreat		No
22	1	7.1	Stable-Retreat		Yes
23	4	6.4			No
24	1	6.4	Varied		No
25	4	14.9			No
26	4	15.8			No
27	2	8.8	Varied		No
28	1	13.1	Varied		No
29	1	4.5	Stable-Retreat		Yes
30	4	13.6			No
31	1	11.1	Stable-Retreat	Bed data error	No

32	1	13.4	Stable-Retreat	Yes
33	1	3.3	Stable	Yes
34	1	8.8	Varied	No
35	1	8.5	Stable-Retreat	Yes
36	4	4		No
37	4	1.3		No
38	3	3.2		No
39	3	9.3		No
40	3	3.5		No
41	1	4.1	Retreat	No
42	1	7.6	Retreat	No
43	4	3.5		No
44	1	7.7	stable-retreat-stable	Yes
45	4	0		No
46	3	3.5		No
47	1	5.7	Varied	No
48	1	5.1	Varied	No
49	1	4.4	stable-retreat-stable	Yes
50	4	0		No
51	1	4.9	Retreat	No
52	2	4.8	Retreat	No
53	2	1.1		No
54	1	2.2	Stable-Retreat	Yes
55	4	2.1		No
56	3	3.5		No
57	4	3.1		No
58	1	2.8	Stable-Retreat	Yes
59	2	3	Insufficient data	No
60	4	2.5		No
61	2	2.1	Stable-Retreat-Stable	Yes
62	2	0		No
63	2	2.6	Stable-Retreat	Yes
64	1	2.8	Insufficient data	No
65	2	2.8	Stable-Retreat	Yes
66	3	1		No
67	1	3.2	Varied	No
68	1	3.1	Insufficient data	No

69	1	1			No
70	4	1			No
71	1	2.3	Stable-Retreat	Bed data error	No
72	1	2.7	Stable-Retreat	Bed data error	No
73	1	2.8	Stable-Retreat		Yes
74	2	2.1	Retreat		No
75	4	2.6			No
76	1	2.6	Retreat		No
77	1	2.5	Stable-Retreat		Yes
78	2	2.3	Varied		No
79	1	2.2	Advance-Retreat		Yes
80	2	2.2	Varied		No
81	4	0			No
82	4	2.1			No
83	4	2			No
84	4	2.4			No
85	1	4	Varied		No
86	2	7	Stable-Retreat	Floating	No
87	3	1			No
88	4	2.8			No
89	4	1.1			No
90	2	3.3	Varied		No
91	4	3.2			No
92	4	1.8			No
93	4	1.5			No
94	4	1.5			No
95	4	1			No
96	4	1.9			No
97	3	2.5			No
98	3	2.7			No
99	3	3.5			No
100	3	2.8			No
101	3	2.8			No
102	4	2.6			No
103	4	2.5			No

104	3	2		No
105	4	3		No
106	4	1.1		No
107	4	2.7		No
108	4	2.2		No
109	4	5.1		No
110	4	5.6		No
111	4	2.9		No
112	3	2.9	Stable	Yes
113	3	2.9		No
114	3	2.8		No
115	4	2.4		No
116	3	3.5		No
117	4	3.3		No
118	4	7.3		No
119	4	2.6		No
120	4	1.3		No
121	4	4.3		No
122	4	1.7		No
123	4	0		No
124	3	1.3		No
125	4	1.3		No
126	4	1.3		No
127	4	1.2		No
128	4	1.1		No
129	4	1.1		No
130	4	1.2		No
131	4	1		No
132	4	1.2		No
133	4	1.3		No
134	4	1.2		No
135	4	1.7		No
136	4	1		No
137	4	1.3		No
138	4	1		No
139	4	1		No
140	4	3.7		No

141	4	2.8		No
142	4	2.5		No
143	4	2.6		No
144	4	1		No
145	4	8.5		No
146	4	7.5		No
147	4	12.5		No
148	4	0		No
149	4	12.5		No
150	4	10.5		No
151	4	10.1		No
152	3	24.9		No
153	3	34		No
154	3	0		No
155	4	0		No
156	4	11.9		No
157	1	11.1	Varied	No
158	4	9		No
159	4	1.4		No
160	4	6.5		No
161	4	1.9		No
162	4	2.1		No
163	4	2		No
164	4	2.4		No
165	4	1		No
166	4	1		No
167	2	2.3	Insufficient data	No
168	4	0		No
169	4	1.6		No
170	2	1.6		No
171	1	2.7	Stable-Retreat	Yes
172	2	1.4		No
173	4	1.5		No
174	4	5.7		No
175	2	1.7	Varied	No
176	4	1.7		No
177	2	1.7	Retreat	No

178	4	0			No
179	2	5.6	Retreat		No
180	3	11.1			No
181	3	49.1			No
182	2	1.1			No
183	2	1.1			No
184	2	1.1			No
185	1	3.7	Stable-Retreat	Bed data error	No
186	1	1.5			No
187	2	3.5	Varied		No
188	2	4.3	Varied		No
189	1	4.9	Varied		No
190	4	1.5			No
191	4	1			No
192	4	1			No
193	2	1			No
194	4	1			No
195	2	2.3	Varied		No
196	1	2.2	Varied		No
197	1	2.3	Insufficient data		No
198	4	2.2			No
199	4	1			No
200	4	2.1			No
201	4	1.6			No
202	4	1			No
203	4	1			No
204	4	2.1			No
205	4	1			No
206	4	1			No
207	4	1			No
208	4	1			No
209	4	1.1			No
210	1	2.7	Advance-Retreat-Stable		Yes
211	1	1			No
212	2	2.7	Varied		No

213	2	2.5	Stable-Retreat		Yes
214	4	1			No
215	4	1			No
216	4	1			No
217	4	1			No
218	4	1			No
219	4	1.2			No
220	4	1			No
221	4	1			No
222	4	2.8			No
223	4	4.8			No
224	4	2.8			No
225	4	1			No
226	4	1.6			No
227	1	3.3	Advance-Stable		Yes
228	1	3.3	Varied		No
229	1	3.3	Advance		Yes
230	4	1.2			No
231	1	5.1	Retreat		Yes
232	2	0			No
233	1	5.6	Stable-Retreat		Yes
234	1	3.4	Retreat		No
235	2	3.3	Varied		No
236	2	1			No
237	4	1			No
238	4	1.6			No
239	4	1			No
240	2	3.1	Retreat	Bed data error	No
241	2	1			No
242	2	2.1	Retreat		No
243	2	3.3	Retreat		No
244	4	3.3			No
245	2	3.5	Retreat		No
246	4	2.5			No
247	2	3.2	Stable-Retreat		Yes
248	2	2.7	Stable-Retreat-Stable		Yes

249	4	1.4			No
250	4	0			No
251	2	3.3	Stable-Retreat	Bed data error	No
252	2	2.9	Stable-Retreat		Yes
253	2	3.7	Insufficient data		No
254	2	0			No
255	2	3.2	Varied		No
256	4	2.7	Insufficient data		No
257	4	0			No
258	4	2.7			No
259	2	1			No
260	4	0			No
261	4	1.3			No
262	4	0			No
263	3	1.6			No
264	2	2.4	Advance		Yes
265	4	1			No
266	2	1			No
267	4	1			No
268	4	0			No
269	4	2.6			No
270	4	2.4			No
271	4	1.2			No
272	4	2.5			No
273	4	7.5			No
274	4	4.8			No
275	4	7.8			No
276	1	8.1	Varied		No
277	4	8.5			No
278	3	24.8			No
279	3	9.4			No
280	1	15.7	Advance-Retreat		Yes
281	1	12.3	Stable-Retreat		Yes
282	1	14.2	Advance-Retreat		Yes
283	1	13.9	Varied		No
284	1	16.3	Stable		Yes

285	2	16.1	Stable-Retreat	Yes
286	2	15	Varied	No
287	2	5.9	Stable	Yes
288	4	12.9		No
289	1	15	Stable-Retreat	Yes
290	2	13.1	Stable-Retreat	Yes
291	2	11.4	Stable	Yes

Table 3.6: Classification of glaciers by coverage 1-4 (determined from *Morlighem et al. (2017)*), terminus traces per year, retreat pattern, and exceptions for this study.

Chapter 4

Using the map-view terminus morphology to deduce ice-ocean processes

Abstract

Existing calving laws are unable to accurately represent the range of terminus change observations in ice sheet models casting doubts on how accurate future projections of sea level change can be. In part, this challenge arises because calving represents many different processes, including two that have been recently observed. First, glaciers can calve via serac failure as the result of melt-related undercutting of the glacier terminus face. This type of calving produces small icebergs with changes in the terminus position tied to changes in subglacial discharge. Second, glaciers can calve via buoyant flexure in which glaciers approach flotation toward the terminus, forming basal crevasses that eventually propagate through-ice to form full-thickness tabular icebergs. There is additional complexity in that these calving styles vary across space and time within and between glaciers. Here, we present a simple methodology for characterizing glacier terminus morphology to elucidate the diverse calving styles that might be occurring and how these change over time and space. This is accomplished by quantifying seasonal terminus change, sinuosity, and convexity of termini and comparing this with observations of flotation, subglacial

discharge routing, and ocean-induced melting for four glaciers where differences in these two calving styles have been previously identified. From this, we develop a classification scheme for the two different calving styles based on terminus morphology alone. We then apply this classification to twelve additional glaciers (some with known calving information) to test the robustness of this relationship. We find that the convexity and the sinuosity of a glacier terminus (in combination) is highly indicative of flotation conditions and therefore represent a glacier’s tendency to calve via buoyant flexure. We also find that some glaciers defy neat categorization into each of these end members and may switch calving styles over time or across the glacier fjord.

4.1 Introduction

Calving of outlet glacier termini is observed to occur as a result of at least two processes. The sloughing of icebergs through serac failure is one mechanism that appears to be the result of weakening of the ice above regions of the terminus that are deeply undercut as a result of terminus melt (*Chauch et al.*, 2014; *Rignot et al.*, 2015; *Motyka et al.*, 2003; *Fried et al.*, 2015; *O’Leary and Christoffersen*, 2013). Terminus melt results from subglacial freshwater runoff, which entrains warm, salty ocean water and rises buoyantly along the terminus face causing localized melt that is enhanced closer to the glacier grounding line (*Jenkins*, 2011; *Carroll et al.*, 2015). The effect of this plume melt is expected to vary seasonally with runoff and be distributed according to subglacial conduits, which follow the subglacial hydraulic potential (*Fried*

et al., 2015; *Mankoff et al.*, 2020a). Sloughing is typically a high-frequency, low-volume calving style that is nearly doubled in locations with meltwater plume locations (*How et al.*, 2019). Because terminus melt undercutting is more effective for glaciers where the fjord hydrography permits shoaling of subglacial discharge plumes, sloughing is a more common calving style for these glaciers. Typically, plume shoaling on the surface of a fjord occurs at thin glaciers and in shallow fjords (>500 m; *Carroll et al.* (2016); *Fried et al.* (2018)).

Another style of calving that has been observed is full-thickness calving that results from glaciers approaching buoyant conditions at their termini. The buoyancy causes the terminus to float, allowing basal crevasse formation (*van der Veen*, 1996). Over time, basal crevasses can propagate upwards, where they create flexure zones (surface depressions) across the full width of the glacier characterized by local bending of the terminus (*James et al.*, 2014; *Murray et al.*, 2015b; *Wagner et al.*). Over time, basal crevasses eventually propagate to the surface connecting to surface crevasses, causing large, full-width tabular icebergs to calve off the front of a glacier (*Fried et al.*, 2018; *Murray et al.*, 2015b). This calving style is more common for glaciers with deeper fjords that allow near-flotation conditions (*Fried et al.*, 2018; *James et al.*, 2014). For these glaciers, the relative impact of runoff on calving timing and volume may be smaller compared to glaciers that calve via serac failure; however, ice melange in fjords can exert a seasonal buttressing effect on the terminus that influences the timing of full-thickness calving events (*Amundson*

et al., 2010; *Robel*, 2017; *Fried et al.*, 2018; *Bunce et al.*, 2022).

In western Greenland, seasonal changes in terminus position have been used to understand environmental controls of the terminus for thirteen glaciers from 2013-2016 by *Fried et al.* (2018). In that study, glaciers that calve via serac-failure tend to have low-amplitude seasonal changes in terminus position (10s of meters) with timing that is strongly correlated with runoff. Conversely, *Fried et al.* (2018) also found that glaciers that calve via buoyant flexure tend to have high amplitude seasonal changes in terminus position (100s of meters), which have a timing more strongly correlated with ice melange presence in the fjord. *Fried et al.* (2018) also found that the morphology of the terminus can be distinguished between these different calving styles with more heavily crenulated glacier termini associated with glaciers calving via serac failure due to the localized nature of the terminus melt at these glaciers. These different calving styles also arise in 3D models of outlet glaciers (*Gagliardini et al.*, 2010; *Benn et al.*, 2017a; *Todd et al.*, 2018) when varying the buoyancy and melt conditions at the terminus. Calving style may also vary across glacier termini, when one side of the terminus is located in a deeper part of the bed, or grounded on a moraine (*Carr et al.*, 2015). Finally, calving styles can vary over time as glacier geometry and fjord conditions change during retreat of the terminus (e.g. *van Dongen et al.*, 2021).

Here, we make use of morphological properties of glacier termini and how they differ in time and between glaciers to identify the characteristics that make calving processes distinct with the goal of categorizing glaciers

by calving style (time and space dependent). By identifying the timing and distribution of different calving styles at glaciers across Greenland, we may be able to improve correlation between existing calving laws and terminus change observations, which are presently only weakly correlated (*Amaral et al.*, 2019; *Benn et al.*, 2017a). In this work, various aspects of the map-view shape of the terminus including its seasonal terminus change, sinuosity, and convex hull area. Then these parameters are used to identify how they vary between glaciers where different calving styles have been previously identified. Then, we apply this classification to twelve additional glaciers to test the robustness of this relationship.

4.2 Methods

Our overarching methodology is to examine the terminus dynamics and morphology for glaciers in central west Greenland where data availability and prior work allows us to confirm calving style (and changes in calving style with time). We search for two distinct calving styles; 1) full-thickness calving via buoyant flexure as glaciers approach buoyancy toward their termini (*Amundson et al.*, 2010; *Murray et al.*, 2015b; *James et al.*, 2014) and; 2) serac failure related to undercutting induced by submarine melt (*Fried et al.*, 2015; *Chauch et al.*, 2014).

4.2.1 Glaciers

Our initial focus is on four glaciers in central western Greenland with known differences in calving patterns and retreat based on previous research (Fig. 4.1; *Catania et al. (2018)*; *Fried et al. (2018)*). For each glacier experiencing retreat, we term the time before the onset of retreat to be "pre-retreat", the time after after retreat to be "post-retreat". One of the four glaciers, Rink Isbr (RNK; Glacier 1) is characterized by a deep grounding line with regularly occurring, full-thickness calving events for most or all of the satellite era (*Medrzycka et al.*; *Bartholomaus et al., 2016*; *Morlighem et al., 2017*; *Fried et al., 2018*). This style of calving is commonly associated with floating termini (*James et al., 2014*; *Murray et al., 2015b*) and RNK has a portion of its terminus that is floating (*Rignot et al., 2015*; *Bartholomaus et al., 2016*; *Fried et al., 2018*) where icebergs tend to form and detach. RNK has large seasonal swings in terminus position that makes it difficult to detect small changes in terminus position (*Catania et al., 2018*), however there was a small, ~ 1 km retreat from 1995-2012 (*Catania et al., 2018*). The neighboring glacier, Kangerdlugssup Sermerssua (KAS; Glacier 291), has a well-grounded and stable terminus that has not retreated during the satellite era (*Catania et al., 2018*). Calving style for KAS has been characterized as a serac-failure, and most of the terminus change occurs local to the central part of the terminus where subglacial plumes frequently breach the surface of the fjord *Fried et al. (2018)*; *Jackson et al. (2019)*. Observations of Store Gletscher (STR; Glacier 284) have shown that the front can reach flotation, however, it does not do so persistently (*Rignot*

et al., 2015; *Walter et al.*, 2012). This glacier has also remained stable during the satellite era (*Catania et al.*, 2018). STR has evidence of subglacial plumes that breach in summer, creating embayments (*Chauch et al.*, 2014). Previous authors have characterized its calving style as bimodal, with full-thickness icebergs formed toward the southern margin and serac-failure more frequent along the northern margin (*Todd et al.*, 2018; *Cook et al.*, 2021). Finally, we examine Sermeq Silardleq (SIL; Glacier 288) which underwent a ~ 5 km retreat starting in 1998 (*Catania et al.*, 2018). While *Fried et al.* (2018) observed a flexure zone in 2016 and large-amplitude seasonal changes in the terminus between 2013 and 2017, supporting calving via buoyant flexure, little is known of the calving style before 2016. We also examine terminus morphology at an additional twelve other glaciers where retreat, seasonality, and fjord geometry are well constrained. This includes 11 additional glaciers in central west Greenland with unknown calving styles (*Catania et al.*, 2018; *Fried et al.*, 2018; *Felikson et al.*, 2017) and Helheim Glacier in southeastern Greenland, which is known to calve via buoyant flexure (*James et al.*, 2014; *Murray et al.*, 2015b). Nearly all of these additional glaciers started retreating in 1995/1998, except UMI and ING which began retreating in 2001/2002 (*Catania et al.*, 2018). Helheim has undergone various retreats and advances since the 1970s, and had 7.6 km of terminus retreat between 1984 and 2017 (*Bevan et al.*, 2012; *Fahrner et al.*, 2021).

4.2.2 Terminus Data

We use terminus data from both TermPicks (*Goliber et al., 2022*) and a new terminus trace data set derived from machine learning using Sentinel-1/2 (*Zheng et al., in prep*) that provides unprecedented resolution of terminus changes, particularly between 2014-2021 when Sentinel-1 was launched. Sentinel-1 is an imaging radar that differs from optical satellites (e.g. Landsat) as it is able to detect termini in winter months when optical images fail to do so due to low illumination. We calculate terminus change following (*Catania et al., 2018*) and interpolate points along each terminus trace to evenly spaced points every 30 m and then projecting these points to a centerline. The terminus position is then the mean of the projected centerline points and it has a minimum resolution of 30 m, which is the resolution of the majority of the input data used to derive terminus traces (*Goliber et al., 2022*). Here we focus on long-term trends in terminus shape and position and so we interpolate the terminus position data over a 7-day time period and then apply a LOWESS filter over a 2-year window. We derive yearly seasonality as a measure of the total variation in the terminus position over the annual cycle. This is quantified using the standard deviation of the difference between the raw terminus position data and the LOWESS smoothed terminus position data. We estimate seasonality for glaciers in years where there are terminus traces in at least four unique months to ensure accurate and detailed seasonality.

4.2.3 Terminus Morphology

We quantify the terminus morphology by its sinuosity and convexity for each terminus trace from 1985-2021 (Fig. 4.2). We calculate the piece-wise sinuosity for 1 km segments along the termini. The piece-wise sinuosity allows us to correlate local changes in sinuosity to locations of potential subglacial channels. The mean sinuosity is the mean of all piece-wise values across the terminus. For reference, the median global river sinuosity is estimated to be 1.11, with a 1st quartile of 1.04 and a 3rd quartile of 1.34 (*Frasson et al.*, 2019). As a measure of convexity, we also compute the convex hull area, which measures the space enclosed by the terminus and the terminus end points (Fig. 4.2). This is done using the Shapely package in Python, which creates the smallest convex polygon containing all points along each terminus trace (*Gillies*, 2013). We then cropped the resulting polygon by the terminus in order to isolate only the convex polygon associated with the glacier. The centroid of the resulting polygon determines whether the terminus is convex or concave. If the centroid is located down-fjord of the line connecting the two terminus end points, it is defined as convex, and the convex hull area is positive (e.g., Fig. 4.2b). Conversely, if the centroid is located up-fjord of the line connecting the two terminus end points it is defined as concave and has a negative convex hull area (e.g., Fig. 4.2b). For both of these parameters we perform the same long-term smoothing as done with the terminus position described above. This includes a 7-day interpolation and the application of a LOWESS filter over a 2-year window.

4.2.4 Height above Buoyancy

We use multiple Digital Elevation Models (DEM) to compute the height above buoyancy (H_{ab}) following (*van der Veen*, 1996),

$$H_{ab} = H - \frac{\rho_{sw}}{\rho_i} D \quad (4.1)$$

where D is the fjord depth below mean sea level, H is the ice thickness, ρ_{sw} is the density of seawater, and ρ_i the density of ice. We used a common bed topographic digital elevation model from BedMachineV4 (*Morlighem et al.*, 2017) for all surface elevation DEMs to derive H . We also use a seawater density of 1023.6 kg/m³ and an ice density of 917 kg/m³. Digital elevation models of surface elevation are available from a variety of sources. First, we use AeroDEM from 1985-1987 with a spatial resolution of 25 m and a vertical accuracy of ~ 6 m (*Korsgaard et al.*, 2016). Second, we used ArcticDEM strips from the Polar Geospatial Center, with a spatial resolution of 2 m and a vertical accuracy of ~ 6 m (*Porter et al.*, 2018). Digital elevation models provided by ArcticDEM cover ~ 2011 -2021 for our four glaciers of interest. Finally, we used the GrIMP digital elevation model derived as an average surface elevation obtained from ASTER and SPOT digital elevation models for a nominal year of 2007 (*Howat, I.*, 2015). For each surface elevation digital elevation model we resampled the digital elevation model to 150 m to match the spatial resolution of the BedMachineV4 data. We also used the geoid height included with BedMachine to convert to heights referenced to the WGS84 ellipsoid.

We computed H_{ab} within a region bounded by the terminus trace, the fjord walls, and a distance upstream of the terminus trace estimated by the stress coupling length (~ 4 times the ice thickness; *Enderlin et al. (2016)*). We then take the median value of H_{ab} in this region to get a single value of H_{ab} per digital elevation model to compute a time series of H_{ab} . We define glaciers with a median value of ≤ 50 m H_{ab} as “near floating” and those with > 50 m H_{ab} as “grounded” after *van der Veen (1996)*. Near the terminus, the mean error in the bed topography data ranges between ~ 30 -60 m *Morlighem et al. (2017)*, limiting confidence in H_{ab} . To confirm buoyant conditions, we also look for flexure zones (*i.e. James et al. (2014); Murray et al. (2015b); Wagner et al.*) in both map-view and along-flow transects to confirm flotation conditions at these glaciers (Supp. Figs 4.15-4.18). All digital elevation models and mean bed errors used for each glacier can be found in Supplementary Tables 4.5-4.8.

4.2.5 Subglacial Hydrology

We also use digital elevation model data to estimate the locations of subglacial channels calculated using the hydraulic potential following *Shreve (1972)*

$$h = z_b + k \frac{\rho_i}{\rho_w} (z_s - z_b) \quad (4.2)$$

where h is the hydraulic head, z_b is the bed topography, k is the flotation fraction (for simplicity, we use $k = 1.0$ following *Mankoff et al. (2020a)*), ρ_i and ρ_w are the ice and freshwater densities respectively, and z_s is the ice surface. This produces gridded values of the subglacial hydraulic head and we find locations

of subglacial channels using the GRASS GIS tool 'r.stream.extract' (?) following (*Mankoff et al.*, 2020a). We only calculate the presence of channels near to the termini and do not determine the upstream contribution area. Thus, there is no differentiation between channels that may contribute more discharge. The resolution of the channels is 150 m. We compute channel locations with the oldest (AeroDEM) and newest (PGC) digital elevation models and do not find large deviations (>150 m) in the locations of subglacial channels, thus we present only our results from the AeroDEM (1985 surface topography). To further estimate locations of subglacial discharge, we map the central locations of plumes determined from Landsat imagery from 1985-2021 during the months of June and July. As plumes may exist across the terminus and may not reach the surface as they reach buoyant equilibrium before breaching, we expect this is an under-estimation of locations of subglacial plume outlets (*Fried et al.*, 2015; *Carroll et al.*, 2015). Plumes were identified and mapped using GEEDiT (*Lea*, 2018).

4.2.6 Submarine terminus melt

We estimate yearly terminus submarine melting q_m following (*Wood et al.*, 2021b; *Rignot et al.*, 2016a)

$$q_m = (A h Q_{sg}^\alpha + B) TF^\beta \quad (4.3)$$

where A , α , B , and β are unit-less constants (*Rignot et al.*, 2016a), h is the fjord water depth at the terminus, Q_{sg} is the glacier subglacial discharge,

and TF is the depth-averaged ocean thermal forcing. We follow *Rignot et al.* (2016a) and use values of $A = 3 \times 10^{-4}$, $\alpha = 0.39$, $B = 0.15$, and $\beta = 1.18$ determined from model parameters from *Xu et al.* (2013-08). For Q_{sg} we use the daily ice sheet liquid runoff from 1992-2019 from *Mankoff et al.* (2020a) who use a regional climate model to estimate runoff. We then use the glacier catchment basins outlined by *Mankoff et al.* (2020a) to sum glacier runoff for each glacier and a 7-day rolling mean to derive a discharge product (Fig. 4.1). For h we extract the mean fjord depth across the terminus over time from BedMachineV4. To remove noise and handle missing data, we apply a 1-day interpolation and the application of a LOWESS filter over a 2 year window to smooth our data. Finally, we use TF is provided by *Wood et al.* (2021b) who use the Estimating the Circulation and Climate of the Ocean (ECCO) model and ocean CTD data integrated over the deepest 60% of the water column to reconstruct TF from 1992-2016 in front of each glacier. This is provided in 2-week increments, therefore we interpolate onto a daily timescale in order to use it in conjunction with the runoff data. We apply a rolling yearly mean of q to estimate annual submarine melting spanning from 1992-2016. Values of each product used for each glacier can be found in Supplemental figures 4.19-4.22.

4.2.7 Cluster Analysis

In order to classify glaciers by calving style, we use K-means clustering in three dimensions for sinuosity and convex hull area against q_m , H_{ab} , and

seasonality using the SciPy package in Python (*Virtanen et al., 2020*). K-means clustering is an unsupervised learning algorithm that finds clusters of data that have not been explicitly labeled based on trends in the data. In order to find the optimal number of clusters, or the k value, we calculate the Within Cluster Sum of Squares (WCSS) for several values of k , where a smaller value indicates less variance within each cluster and better clustering of the data. We choose the value where WCSS starts to diminish, or at the elbow (e.g., Elbow Method; Supp. Figs. 4.23-4.25; *Cui (2020)*). Using this cluster analysis, we then explore how the morphology of several other glacier termini might fit into our classification scheme. This includes an additional twelve glaciers; eleven in the same region as the four that are the focus of this study (central west Greenland) and Helheim (HEL) in southeast Greenland (Fig. 4.1). For the q_m clustering analysis, we only use dates where q_m is greater than 0.5 m/day so we are observing times where there is active melt-undercutting occurring. For the H_{ab} clustering analysis, we take the closest terminus trace value for convex hull area and sinuosity for the dates where digital elevation models are available to provide estimates of H_{ab} . For the seasonality clustering analysis, we take the mean values of sinuosity and convex hull area for the years where seasonality can be calculated. Therefore, the H_{ab} and seasonality clustering analysis will have far fewer data points to the q_m clustering analysis.

4.3 Results

4.3.1 Terminus Flotation

Since 2016 (when the *Catania et al.* (2018) data set terminated), STR, KAS, and RNK have all remained largely unchanged while SIL has continued to retreat, though at a slower pace compared to ~ 2010 . In total, SIL has retreated an additional 0.5 km since 2016 (Fig. 4.3). Despite RNK experiencing a small retreat over the observational period, the flexure zone remains consistently in the same location over time (Fig. 4.3, Supp. Fig.4.15). Unlike RNK, KAS and STR remain fully grounded throughout the entire record with very small regions of the terminus that approach flotation close to the terminus edge where the glacier thins (Figs 4.4, 4.5). Neither of these glaciers develop a flexure zone during our time period. SIL is the only glacier that undergoes significant retreat and thinning in the observational period, making it susceptible to changing flotation conditions with time. Indeed, we observe that SIL experiences a shift in its H_{ab} from grounded prior to 2012 to near floating post ~ 2014 (Fig. 4.6), although there are only small differences between the mean H_{ab} over the pre- and post-retreat time periods (Table 4.1). This is largely because the SIL terminus did not enter the overdeepening that would promote flotation until ~ 2012 (*Catania et al.*, 2018). While SIL does not initially have a flexure zone, one develops in approximately 2014 and is in place intermittently to the end of the observational record (Fig.4.6, Supp. Fig 4.17).

4.3.2 Submarine Melt and Hydrology at Termini

For all glaciers, submarine melt (q_m) generally increases over the observational period until ~ 2008 and then begins to decrease as previously identified by (*Wood et al.*, 2021b). KAS experiences its peak melt rate earlier, in 2006 (1.5 m/day; Supp. Fig. 4.22) and STR has a peak in 2007 (2.5 m/day; Supp. Fig. 4.20), while RNK and SIL have melt peaks in 2011 (3.5 m/day for RNK; Supp. Fig. 4.19 and 2.1 m/day for SIL; Supp. Fig. 4.21). Overall values of submarine melt are lowest for KAS and highest for RNK. The hydraulic potential maps show that estimated locations of subglacial channels and we find that they follow low elevation paths in the bed topography (Figure 4.7). In addition, we find that the locations with the densest presence of sediment plumes are located where the hydraulic potential maps estimate outlets at the terminus (Fig. 4.7). We also find there are outlets located where subglacial discharge plumes do not breach the fjord surface (so no sediment plumes are visible). While there may be some melt-induced undercutting related to subglacial discharge in these regions, because they do not reach the fjord surface, undercutting may be limited, and the impact on terminus morphology would then also be limited.

4.3.3 Terminus Seasonality

Both STR and KAS have relatively low mean seasonality of 99 and 95 m respectively over the observational period (Fig. 4.8, Table 4.1). In contrast RNK has a mean seasonality of 234 m. The seasonality of SIL changes over

the observational period (Fig. 4.8). While the mean is 139 m, it has a pre-retreat seasonality of 80 m (close to STR and KAS) and a post-retreat onset seasonality of 165 m.

4.3.4 Sinuosity

We take the mean sinuosity across the observational time period for all four glaciers and find that typical sinuosity values range between 1.04-1.22 (Table 4.2, Fig. 4.9). RNK (1.04 ± 0.05) and STR (1.06 ± 0.04) are both low sinuosity termini that retain low sinuosity values over the observational time period. Contrasting this is KAS (1.15 ± 0.08), which is a high sinuosity terminus, which retains a relatively high sinuosity value over the observational time period (Fig. 4.9). Finally, SIL has a mean sinuosity that is similarly high to KAS (1.10 ± 0.08), but the SIL terminus experiences large changes in its sinuosity over time. Pre-retreat, SIL has high, and increasing sinuosity (1.13 ± 0.05) then decreases slightly after retreat onset (1.10 ± 0.09) but in 2010 SIL undergoes a rapid decrease in sinuosity to values more typical of RNK and STR (after 2010: 1.06 ± 0.04), where it remains relatively constant to the present day.

Using piece-wise sinuosity we are able to identify variations in sinuosity across individual terminus traces. We find that the regions of the termini with the highest piece-wise sinuosity values are typically co-located with predicted subglacial channel and sediment plume locations (Fig. 4.7). This is most obvious for KAS, which has piece-wise sinuosity values that are highest in the

central and northern part of the terminus (Fig. 4.7D). These parts of the KAS terminus are where subglacial channels are predicted to exist and where we see a high density of plumes breaching the fjord surface. The northern margin of KAS has very few plumes occurring there compared to in the central part of KAS. SIL also shows co-location of high piece-wise sinuosity regions of the terminus and the expected locations of subglacial channels, although plumes do not breach as readily as the terminus is much deeper (Figs. 4.7B, Supp. fig. 4.21). We also see a marked change in the piece-wise sinuosity of SIL post ~ 2012 when the piece-wise sinuosity decreases and there is no more correlation between subglacial channel locations and high piece-wise sinuosity values.

For STR, the relationship between piece-wise sinuosity and subglacial discharge is less apparent as there are portions of the terminus with very straight sections associated with sediment plume and subglacial discharge locations. There are also portions of the STR terminus with high piece-wise sinuosity that are also co-located with subglacial channel locations and sediment plumes (Fig. 4.7C). Higher piece-wise sinuosity values are evident in some of the RNK terminus traces, particularly when the glacier briefly advanced onto a shallower region of the bed in ~ 1993 (Fig. 4.7A).

4.3.5 Convex Hull Area

Convex hull area is heterogeneous over time and across all four glaciers ranging from ~ -4 to 4 km^2 (Fig. 4.10, Table 4.2). KAS has the highest positive convex hull area with a mean over the observational period of 3.43 ± 0.44

km². STR has a convex hull area that is lower than KAS and closest to zero (0.98 ± 0.71 km²) indicating that the STR terminus comes closest to a straight line. convex hull area for both STR and KAS remain positive for most of its record (there is a brief exception for STR between 1993-1996) suggesting that these termini typically exhibit convex morphologies. RNK has the lowest convex hull area with a mean of -2.13 ± 0.93 km². The persistent negative values for RNK indicate that its terminus is typically concave. The changes in convex hull area over time for RNK, STR, and KAS are all small ($\pm 1-2$ km²). In contrast, we observe large > 6 km² changes in the convex hull area for SIL over the observational time period. Pre-onset of retreat, SIL maintains a relatively high, positive convex hull area value (convex; 2.43 ± 0.41 km²), and then the morphology transitions to a high negative convex hull area value (concave; -2.05 ± 2.37 km²) after it retreats in 1998.

4.3.6 Cluster analyses

We perform a 3D cluster analyses using terminus morphology (convex hull area and sinuosity), seasonality, and environmental data (H_{ab} and q_m) in order to determine which variables are typically associated with each other. This is done first by comparing each of the morphology variables against H_{ab} (Fig. 4.11), q_m (Fig. 4.12), and then to yearly seasonality values (Fig. 4.13). We have considerably less data for H_{ab} and seasonality than for q_m because of less frequent digital elevation model data being available for the earlier part of our observational period and because of the yearly resolution of seasonality.

For all three of these cluster analyses, two dominant clusters fall out. The first cluster (labeled Cluster 0) represents termini with a negative mean convex hull area (concave), lower mean sinuosity, and higher seasonality (Table 4.4), although there is overlap in the sinuosity values with the other cluster. Cluster 0 also has higher mean q_m and a mean H_{ab} that implies that these termini are close to flotation (Table 4.4). We also find a group of termini, Cluster 1, with positive mean convex hull area, higher mean sinuosity, lower seasonality swings, and lower mean q_m (Table 4.4). While there are brief exceptions, we find that generally STR and KAS termini fall into Cluster 1, while RNK termini fall into Cluster 0. SIL transitions from being in Cluster 1 during the early part of its record to Cluster 0 after ~ 2010 (although we note that the transition to Cluster 0 occurs a few years later for the H_{ab} cluster analysis). From this analysis we can conclude that Cluster 0 type termini indicate calving via buoyant flexure producing concave and lower sinuosity termini on average while Cluster 1 type termini indicate calving via serac failure producing convex and higher sinuosity termini on average.

4.3.7 Application to other glaciers

Using the results of the cluster analysis, we extend our terminus morphology calculations to an additional twelve glaciers (Fig. 4.1). For many glaciers undergoing retreat during the observational period we see a trend from a positive convex hull area (convex) in the pre-retreat period to either a less positive or (more typically) a negative convex hull area (concave) after

retreat has begun (all glaciers except ING, which maintains a more constant convex hull area and AVA, which increases in convex hull area; (Fig. 4.14). However, there is quite a bit of variability in the change in terminus sinuosity pre- and post-retreat for these glaciers. KAN, EQI, and KUJ all undergo switches in convex hull area from positive to negative values and decreases in terminus sinuosity after retreating, similar to what we observed for SIL. HEL, the only glacier on the southeast coast in this study, remains highly concave and low sinuosity (Fig. 4.14). The mean seasonality for all glaciers except for HEL, UMI, ING, and KUJ are below 100 m (Table 4.3). HEL has the highest seasonality at 533 m and KNG has the lowest at 30 m.

4.4 Discussion

4.4.1 Correlation between terminus processes and morphology

We compare glacier morphological parameters to environmental forcing parameters in order to deduce the dominant processes acting on glacier termini as they undergo change over time. From our H_{ab} cluster analysis (Fig. 4.11), we find that the convex hull area may be the strongest indicator of buoyant flexure calving style. This is because negative values of convex hull area (concave termini) are found only in glaciers that are close to flotation. For example, we know from past work that RNK calves via full-thickness icebergs via buoyant flexure (*Medrzycka et al.*; *Fried et al.*, 2018; *Rignot et al.*, 2015; *Bartholomaus et al.*, 2016) and we demonstrate this through examination of map-view H_{ab} (Fig. 4.3), which shows that a relatively large portion of the

RNK terminus remains below flotation through the observational period. This is further supported by evidence of a stationary flexure zone in both digital elevation models for RNK (Figs. 4.3 and 4.15). Previous studies have indicated that the presence of such a flexure zone is highly indicative of calving via buoyant flexure (*James et al.*, 2014) with the terminus retreating in step-like fashion when large tabular icebergs calve (*Joughin et al.*, 2008; *Wagner et al.*). The terminus of RNK in both its pre and post-retreat phases is characterized by low sinuosity and a highly concave shape (negative convex hull area). The RNK terminus also undergoes high seasonal variations in position (>100 m), indicative of large seasonal calving events (*Fried et al.*, 2018). Although there are several subglacial channels located at the terminus, there is little evidence that localized undercutting at the front has an impact on the terminus morphology and thus the calving style for this glacier (Fig. 4.7A).

Conversely, we also see that termini with positive convex hull area (convex termini), which is a strong indicator of glaciers that calve via serac failure. This is because positive convex hull area values are found on glaciers with much higher H_{ab} values (they are well-grounded). For example, past work on KAS reveals that the dominant calving style there is serac failure due to undercutting of the terminus due to ocean-induced melt (*Fried et al.*, 2018; *Bartholomaus et al.*, 2016). KAS is also a thin glacier meaning that undercut parts of the terminus may easily connect with deep surface crevasses close to the terminus leading to serac failure. The terminus of KAS remains well-grounded for the entire observational period and thus is incapable of producing

icebergs that calve due to buoyant flexure. The highest segments of piece-wise sinuosity for KAS are located where subglacial discharge emerges to produce sediment plumes visible on the fjord surface (Fig. 4.7D). Higher sinuosity in these regions is related to increased melt and local undercutting where subglacial channels emerge (*Chauch et al.*, 2014; *Fried et al.*, 2015; *Rignot et al.*, 2016b). Despite this, sinuosity appears to be only weakly correlated to H_{ab} or q_m as there are similar values of sinuosity across both of the two clusters identified. This means that while the convex hull area for a single terminus trace might successfully predict buoyant conditions producing full-thickness icebergs, the sinuosity alone might not and the mean sinuosity over a much longer time period (coupled with the sign of the convex hull area) might be more predictive of the calving style.

4.4.2 Calving Style Exceptions

Based on the correlation between the morphology and forcing parameters in our cluster analysis and previous knowledge of calving styles for these glaciers, we propose two clusters that are representative of the two different calving styles previously identified (Figs. 4.11), 4.12). Cluster 0 is made up primarily of RNK and SIL post-2010, and we interpret this cluster to be indicative of termini that calve via buoyant flexure. Cluster 1 is made up of KAS, STR, and SIL pre-2010 and is indicative of glaciers that primarily calve via serac-failure from melt-induced undercutting. While RNK is primarily in Cluster 0, there are times when RNK terminus traces fall into Cluster 1

(slightly more sinuous, and more convex), primarily occurring when RNK was more advanced than present, possibly grounded on the moraine right in front of the present-day terminus (Figs. 4.10, 4.9).

Although both KAS and RNK fit neatly into the calving styles described above, STR and SIL do not for different reasons. STR is an example of a glacier that may calve via both styles described above (*Chauch et al.*, 2014; *Todd et al.*, 2018; *Cook et al.*, 2021), and the morphology supports this hybrid style. Although the H_{ab} for STR shows that this glacier is consistently grounded over the observational period, previous studies have indicated that STR may intermittently form a small, $\sim 200\text{m}$ floating tongue seasonally when it advances (*Rignot et al.*, 2015; *Walter et al.*, 2012). The growth of the tongue is likely balanced by submarine melting such that a tongue cannot persist year-round (*Todd et al.*, 2018). The morphology of the STR terminus also appears to be hybrid between both Cluster 0 and Cluster 1 with the majority of termini associated with Cluster 1, particularly since 2000. However, STR has a low sinuosity, similar to that found for Cluster 0 type glaciers. While small segments of the terminus experience high piece-wise sinuosity in locations where subglacial channels and sediment plumes emerge (Fig. 4.7C), the overall sinuosity remains low. STR also has a mean convex hull area that puts it close to being consistently a straight line however, the northwestern end of the terminus is where the terminus becomes more concave, similar to Cluster 0 type termini (Fig. 4.7C). The seasonal signal of STR is also low, similar to other Cluster 1 type termini, possibly because this glacier is quite stably

situated on its moraine (*Morlighem et al.*, 2016b). As a result of this morphological ambiguity, we define STR as one that may calve via both buoyant flexure and serac-failure, perhaps at different locations across the terminus.

SIL behaves in a similar manner to Cluster 1 termini in the pre-2010 period, then it switches to being more like Cluster 0 termini post-2010. Initially, the glacier had a high sinuosity, convex terminus that was grounded above flotation suggesting that it was primarily calving via serac failure. After ~ 2010 the glacier experiences an increase in both retreat rate and seasonal swings in the terminus position and the terminus morphology becomes less sinuous and more concave. Such conditions are more indicative of Cluster 0, with termini calving via buoyant flexure. Even when q_m is increasing for SIL during the retreat, we still see lower sinuosity termini and no embayments associated with subglacial channels in the termini post 2010 (Fig. 4.7B). This suggests that during retreat, SIL came into contact with deeper portions of the bed where it could begin to approach flotation and switch in calving styles to one dominated by full-thickness icebergs created via buoyant flexure.

4.4.3 Extending our Classification to Other Glaciers

Using our cluster analysis, we extend our characterization of calving styles to the other glaciers where we do not have detailed time series of H_{ab} or q_m . This is done by taking the range of the convex hull area and sinuosity values for each of Cluster 0 and 1 from all three clustering analyses (Table 4.4) and plotting the additional twelve glaciers within this range to identify

which cluster they might belong to (Fig. 4.14). Since sinuosity values for both clusters overlap significantly, we primarily use the convex hull area to define differences in calving styles for these glaciers. We further assign any convex hull area values found to be more positive/negative than our observed ranges to fall into either Cluster 1/0. When we apply the cluster analysis to other termini, we find a diversity in terminus behavior over time and space. HEL is almost entirely in Cluster 0, which is expected as it is glacier that is known to calve via buoyant flexure (*James et al.*, 2014; *Murray et al.*, 2015b; *Williams et al.*, 2021). Nearly all of the west Greenland glaciers are located primarily in Cluster 1 (EQI, KAN, AVA, LIL, LIK, KNG, KSS), with a few migrating into Cluster 0 later in the time series, potentially after a retreat event (KUJ, PRD, UMI). ING is the only glacier in west Greenland (apart from the original glaciers RNK and SIL) that remains primarily in Cluster 0 for the majority of observations. We also find that glaciers that cluster primarily in or migrate to Cluster 0 have slightly higher seasonality than those in Cluster 1 (Table 4.3). Glaciers in west Greenland are generally closer to having straight line terminus traces (convex hull area ~ 0 km²) and moderate sinuosity, but most are serac-failure calving glaciers (Fig. 4.14). This is consistent with the seasonal calving styles presented in *Fried et al.* (2018) between 2013-2016, as they found that most glaciers in this region (other than RNK, SIL, and STR) are likely to calve seasonally through serac failure in 2013-2017. However, the categorization of these types of glaciers were limited to seasonal signals and velocities, so they may also experience a combination of these end-member types. Additionally,

we see differences in terminus morphology, and thus calving style over time as many glaciers in this region retreat. This implies that the dominant style of calving may have been switched as the glacier enters into regions of the fjord that are overdeepened, promoting flotation.

4.4.4 Shortcomings and Future Directions

Shortcomings in this study are mainly related to limitations in temporal resolution of the bed topography, data reliability, and the limited number of glaciers used to develop the clusters. The availability of digital elevation models is limited prior to ~ 2010 in the Arctic due to difficulties related to detecting elevation changes over snow and ice (*Schenk and Csatho, 2012*). Recent work has been undertaken to improve temporal sampling of elevations through use of improved resolution ASTER digital elevation models, which are available from 2000-present (*Girod et al., 2017-07*). In order to improve the robustness of our cluster analysis, we plan to include additional digital elevation models from processing ASTER scenes in our study area to increase the availability of observations of H_{ab} over time. Additionally, there is variable uncertainty in the modeled bed topography (*Morlighem et al., 2017*) (see supp. table 4.5-4.8). Finally, while we find robust classification of calving style for our four glaciers of interest, calving styles may differ beyond the two types identified here. Thus, including more glaciers into the cluster analysis will provide an even more robust mechanism for identifying calving style across a larger population of glaciers using terminus morphology alone.

4.5 Conclusions

Here we present a simple methodology for categorizing glaciers by their morphology to determine calving styles. As it is likely that the relative contributions of calving via the two processes we have identified varies across and within glaciers, each glacier will not fit perfectly into our proposed end-member system. However, we provide a way forward to use simple calculations representing the terminus morphology might be used as a proxy for how the glacier calving style changes over time and space. Current model parameterizations are unable to reproduce frontal ablation processes that occur at Greenland glaciers (*Amaral et al.*, 2019), possibly as a result of attributing terminus change entirely to one style of calving over another. Advancements in 3D models of individual glaciers are able to reproduce variations in calving styles for single calving events, however these models are computationally expensive and are therefore not applicable to larger-scale ice sheet modeling (*Astrom et al.*, 2013; *Todd et al.*, 2018; *Benn et al.*, 2017b).

ID	Name	Period	Terminus Change (km)	Seasonality (m)	H_{ab} (m)
1	RNK	Mean	-1.20	234	36±7
		Pre-retreat	0.15	241	44*
		Post-retreat	-0.93	231	36± 7
288	SIL	Mean	-5.19	139	64±15
		Pre-retreat	0.21	80	72*
		Post-retreat	-5.52	165	76±15
284	STR	Mean	0.12	96	99±5
291	KAS	Mean	0.15	97	95±4

Table 4.1: Statistics for terminus change, seasonality, H_{ab} for bulk, pre- and post-retreat time epochs for the glaciers in this study. * indicates that only one digital elevation model was available for that period of time.

ID	Name	Period	Sinuosity		Convex Hull Area	
			Mean	STD	Mean (km ²)	STD
1	RNK	Mean	1.04	0.05	-2.13	0.93
		Pre-retreat	1.08	0.07	-0.84	1.66
		Post-retreat	1.04	0.05	-2.23	0.75
288	SIL	Mean	1.10	0.08	-1.60	2.63
		Pre-retreat	1.13	0.05	2.43	0.41
		Post-retreat	1.10	0.09	-2.05	2.37
284	STR	Mean	1.06	0.04	0.98	0.71
291	KAS	Mean	1.15	0.08	3.43	0.44

Table 4.2: Statistics for sinuosity, convex hull area, and submerged area for bulk, pre- and post-retreat time epochs for the glaciers in this study.

ID	Name	Onset	Seasonality (m)
2	UMI	2001.5	118
3	ING	2002.4	171
280	EQI	1998.6	50
281	KAN	1998.5	71
282	KUJ	1998.4	124
283	AVA	1998.5	33
285	LIL	1998.4	32
286	LIK	1995.5	46
287	KNG	1995	30
289	PRD	1998.5	62
290	KSS	1998.3	52
181	HEL	N/A	533

Table 4.3: The TermPicks glacier ID, name abbreviation, and timing of the onset of retreat from *Catania et al.* (2018) seasonality values for the additional twelve glaciers in this study. See Figure 4.1 for the locations of each glacier.

	Cluster 0				Cluster 1			
	Mean	STD	Min	Max	Mean	STD	Min	Max
H_{ab} Cluster analysis								
Convex Hull area (km ²)	-2.39	0.85	-5.3	-0.93	1.74	1.42	-2.46	3.88
Sinuosity	1.05	0.04	1.02	1.22	1.11	0.07	1.02	1.44
H_{ab} (m)	39	10	17	62	97	7	75	107
q_m Clusters analysis								
Convex Hull area (km ²)	-2.33	0.97	-5.85	-0.10	2.26	1.15	-0.36	5.42
Sinuosity	1.05	0.04	1.00	1.55	1.14	0.09	1.00	1.90
q_m (m/day)	2.39	0.74	0.39	3.53	1.26	0.48	0.38	3.37
Seasonality Clusters analysis								
Convex Hull area (km ²)	-1.81	1.46	-4.38	3.54	1.66	1.76	-3.01	4.52
Sinuosity	1.07	0.03	1.03	1.17	1.13	0.06	1.02	1.26
Seasonality	257	54	178	380	91	37	30	172
Cluster Means								
Convex Hull area (km ²)	-2.18	1.09	-5.18	0.84	1.89	1.44	-1.94	4.61
Sinuosity	1.06	0.04	1.02	1.31	1.13	0.07	1.01	1.53

Table 4.4: Statistics for clusters 0 and 1 for the analysis of clusters from the H_{ab} , q_m and seasonality k-means cluster analysis. Cluster means are the mean values for the convex hull area and the sinuosity for all three cluster analyses. These values are used in figure 4.14.

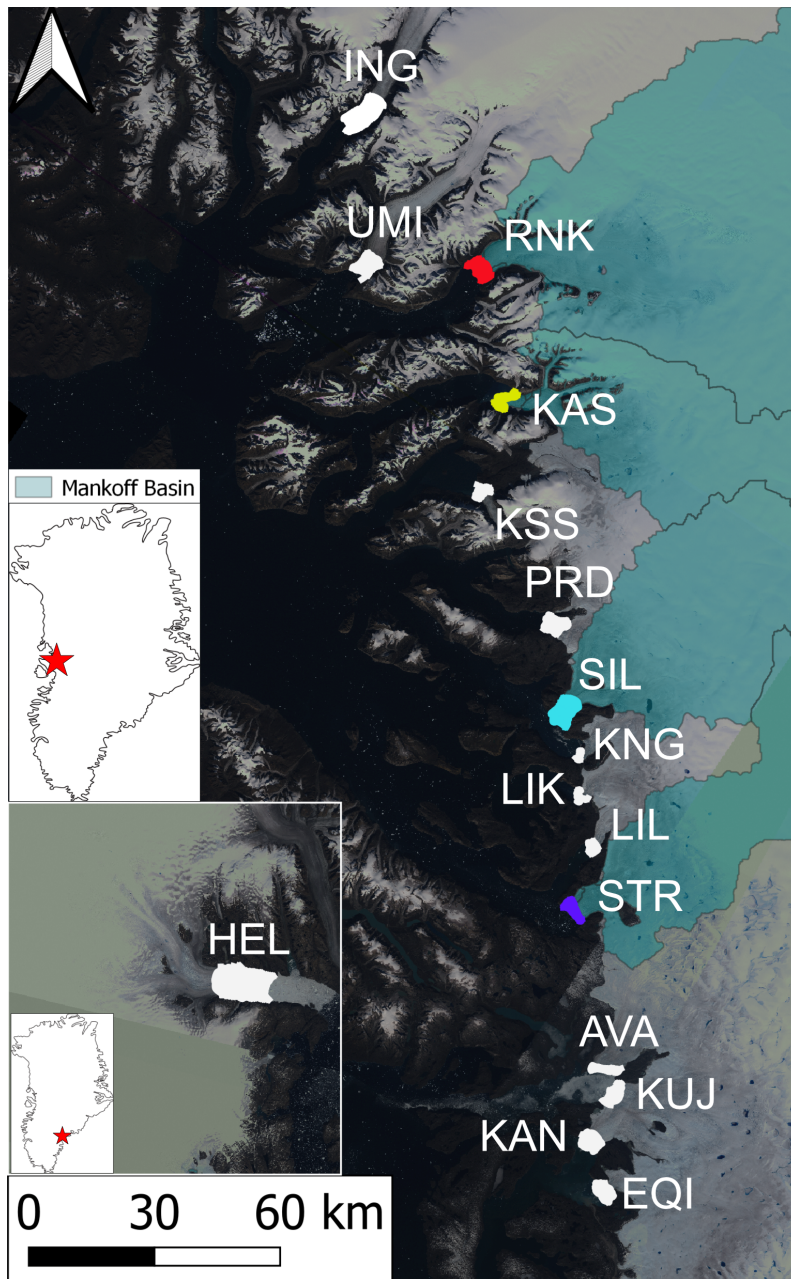


Figure 4.1: Locations of the four glaciers used in this study to develop morphological relationships (colors). Teal colored basins correspond to the basins used to determine runoff from *Mankoff et al.* (2020a). Locations of the supplemental glaciers (white) used to test the proxy developed in this study.

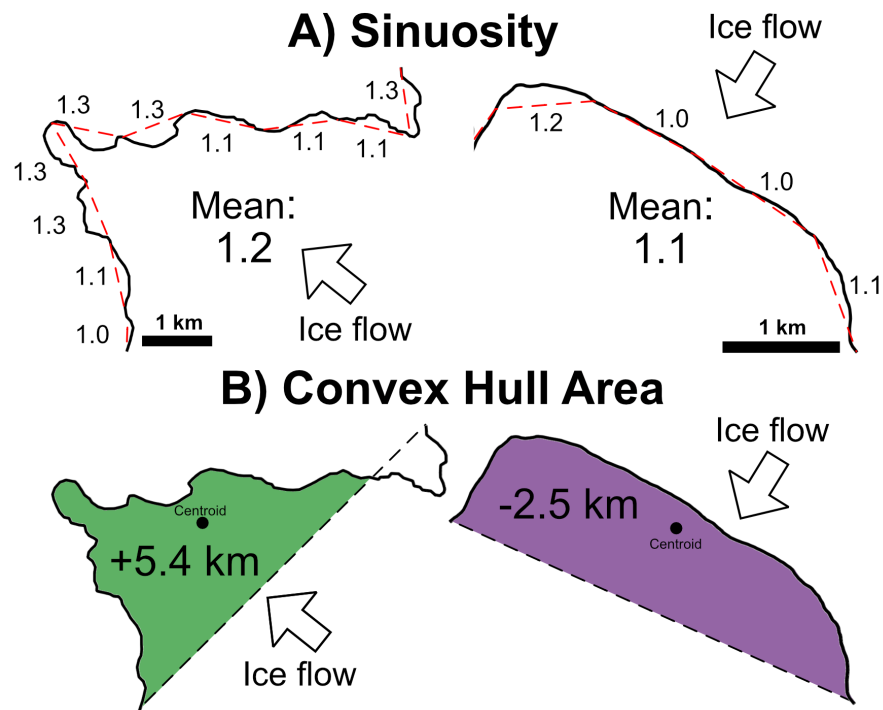


Figure 4.2: Examples of how piece-wise sinuosity and convexity are calculated. a) We compute piece-wise sinuosity for each terminus (red dashed lines) along 1 km segments and then take the mean of all of these to get mean sinuosity. b) Convex hull area is computed to identify termini that are either convex (green) or concave (purple).

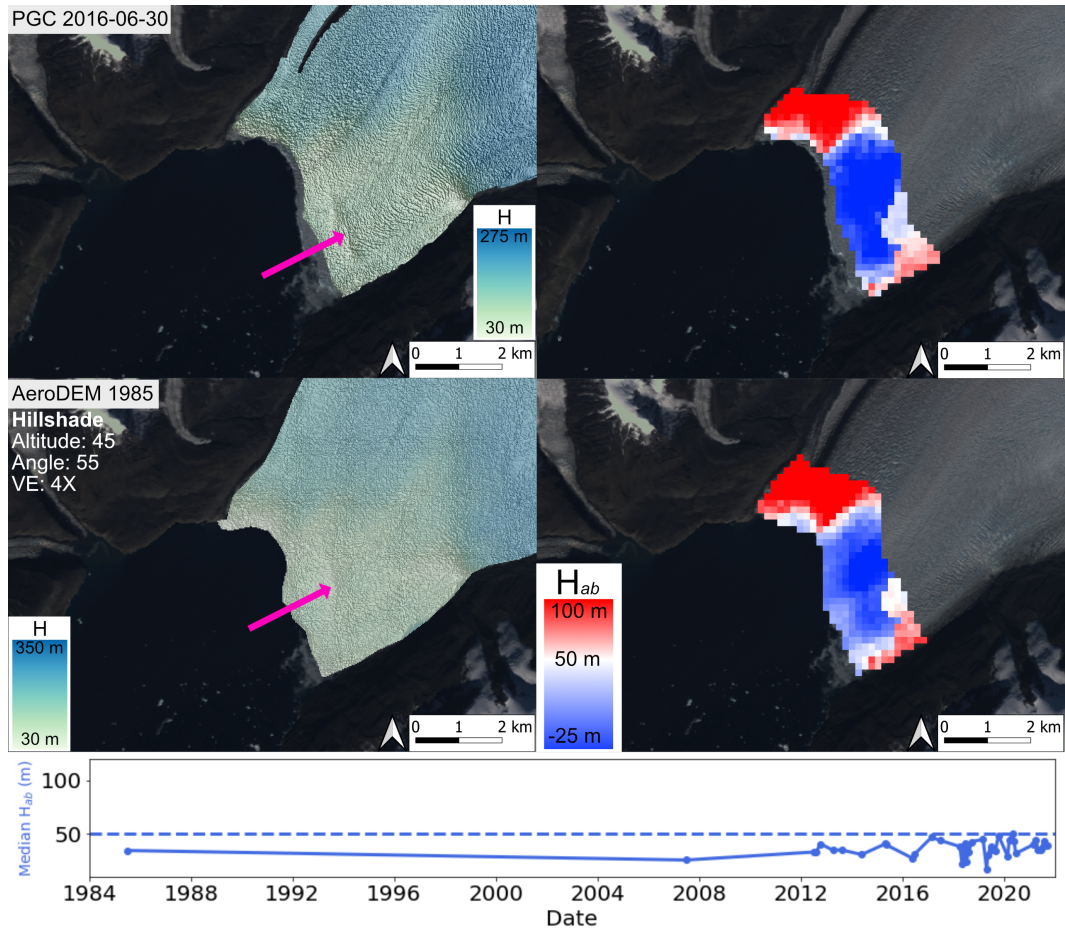


Figure 4.3: Map-view of both a selected PGC digital elevation model and the AeroDEM in 1985 for RNK. Left are hillshade with 4x vertical exaggeration with elevation data overlain and the right is the H_{ab} for the corresponding digital elevation model. The pink arrow points to the location of the flexure zones. The mapped plume locations are represented by the blue heat maps located on the terminus.

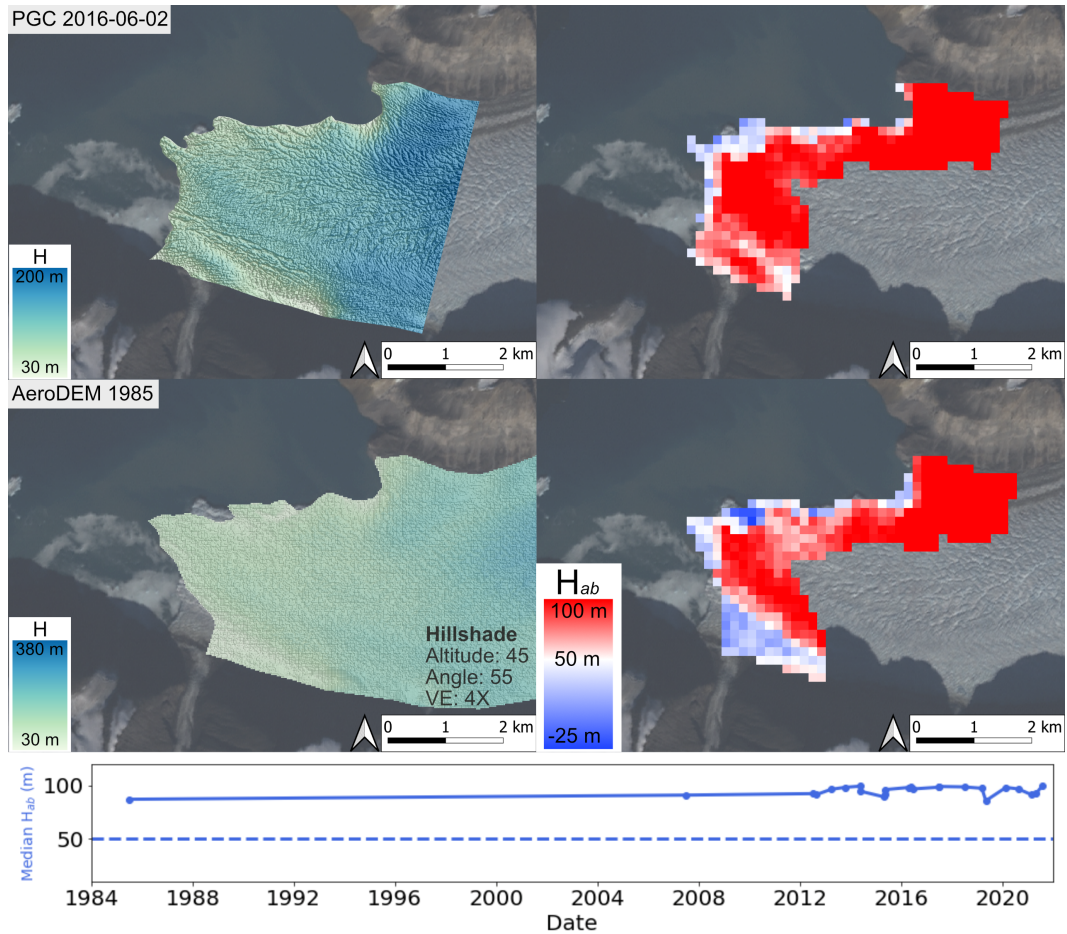


Figure 4.4: Map-view of both a selected PGC digital elevation model and the AeroDEM in 1985 for KAS. Left are hillshade with 4x vertical exaggeration with elevation data overlain and the right is the H_{ab} for the corresponding digital elevation model. The mapped plume locations are represented by the blue heat maps located on the terminus.

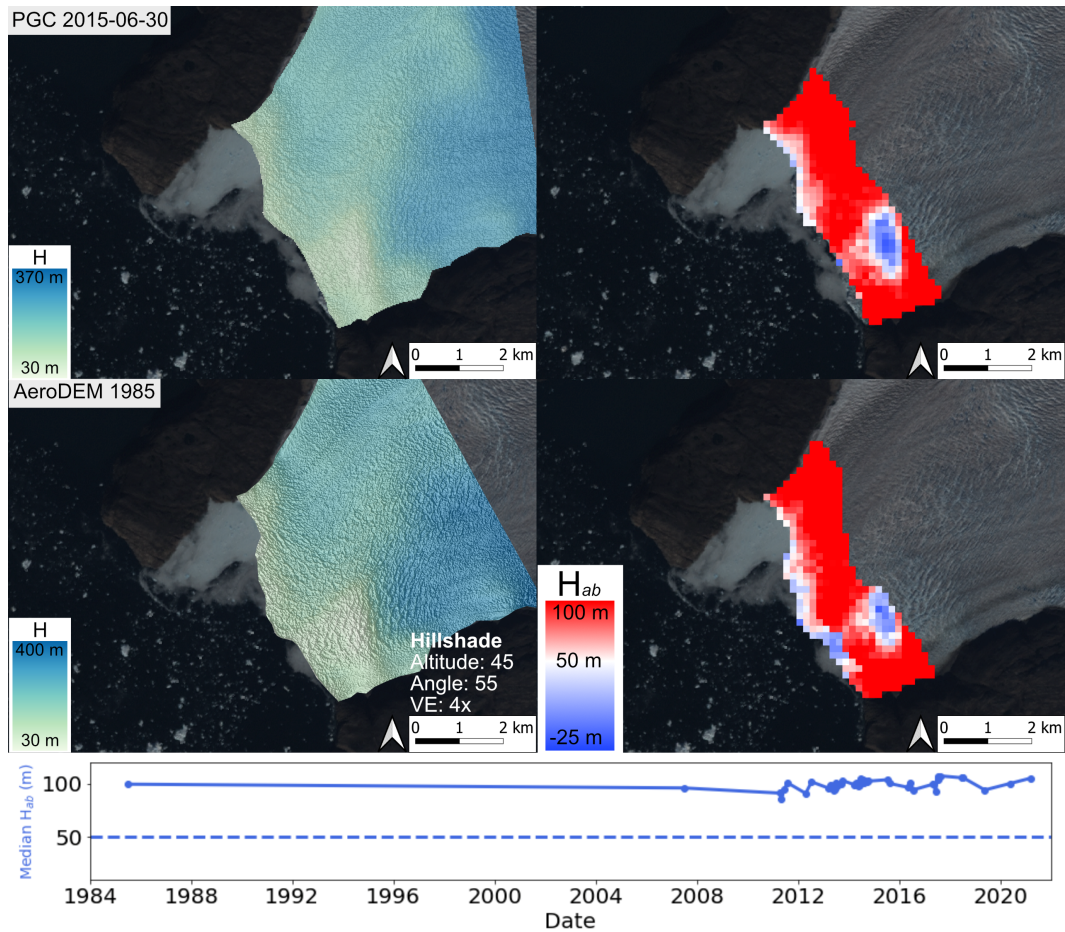


Figure 4.5: Map-view of both a selected PGC digital elevation model and the AeroDEM in 1985 for STR. Left are hillshade with 4x vertical exaggeration with elevation data overlain and the right is the H_{ab} for the corresponding digital elevation model. The mapped plume locations are represented by the blue heat maps located on the terminus.

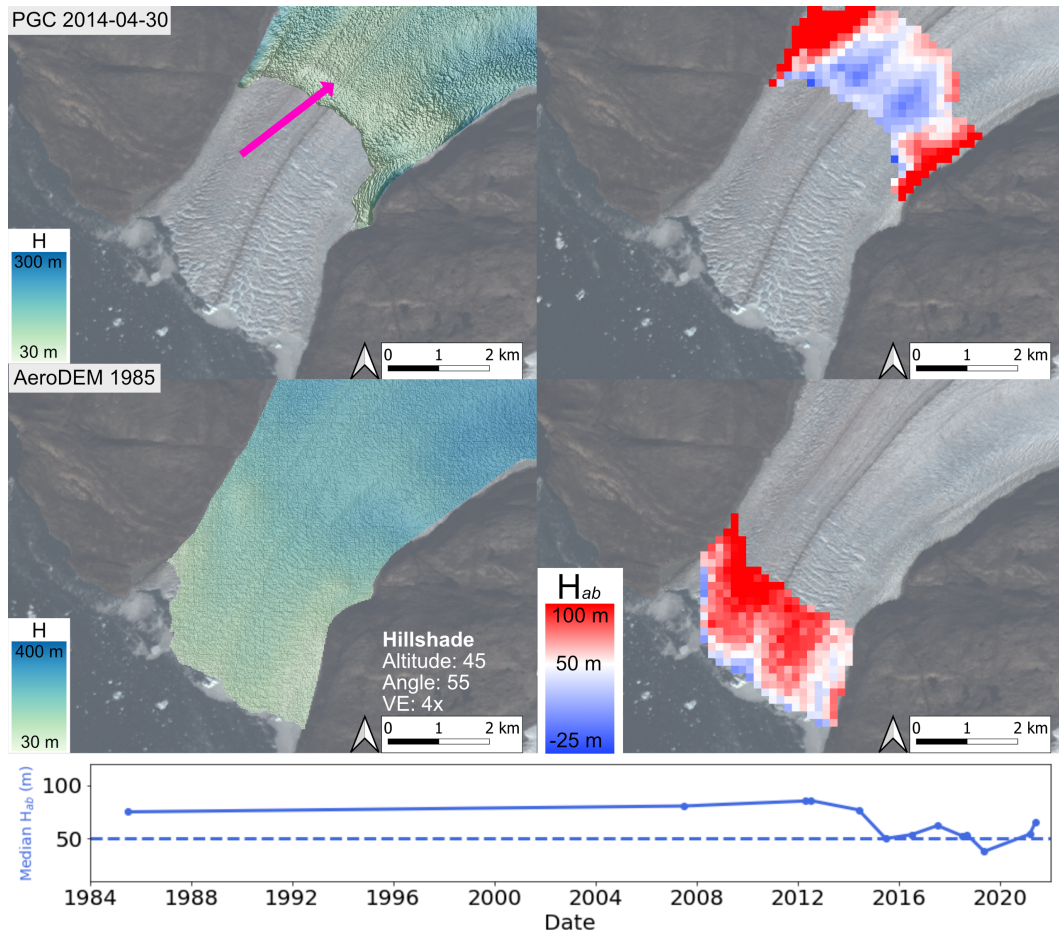


Figure 4.6: Map-view of both a selected PGC digital elevation model and the AeroDEM in 1985 for SIL. Left are hillshade with 4x vertical exaggeration and the right is the H_{ab} for the corresponding digital elevation model. The pink arrow points to the location of the flexure zone in 2014. The mapped plume locations are represented by the blue heat maps located on the terminus.

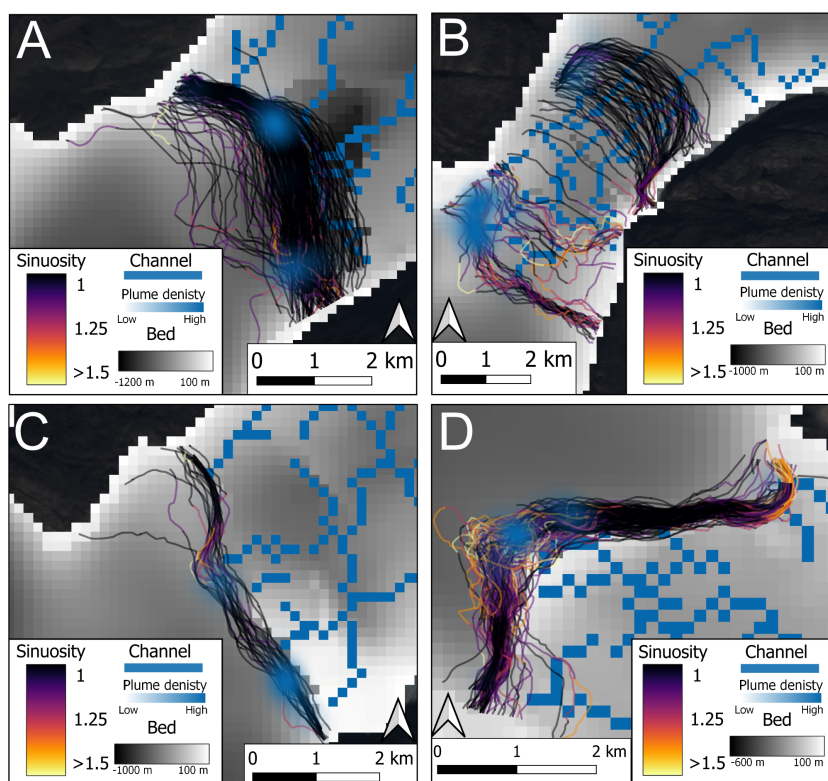


Figure 4.7: Map-view changes in sinuosity for every summertime terminus pick colored by piece-wise sinuosity for glaciers A) RNK, B) SIL, C) STR, and D) KAS. Blue heat maps on the terminus are occurrences of sediment plumes that have breached the surface between 1985-2021. The blue lines on the bed data below the terminus traces is the estimated locations of subglacial channels calculated using the hydraulic potential. The bed is BedMachineV4.

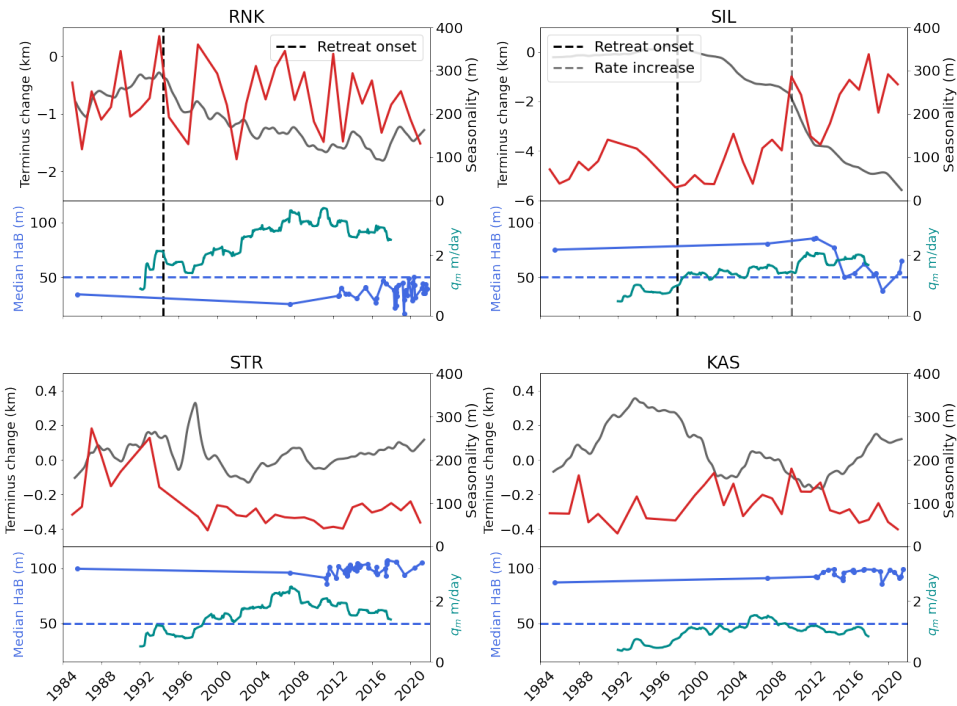


Figure 4.8: Seasonality (red lines) compared to terminus change (black line), parameterized submarine melting (teal line), height above buoyancy (H_{ab} ; blue line) for the four main glaciers used in this study. The H_{ab} value of 50 m reflects the local ellipsoid height. Thus, values above 50 m are interpreted as grounded and values below 50 m are interpreted as floating. Seasonality values for each year are given in red. For glaciers with a retreating terminus, we delineate the onset of retreat (black vertical dashed lines) and an acceleration in retreat for SIL (gray vertical dashed line).

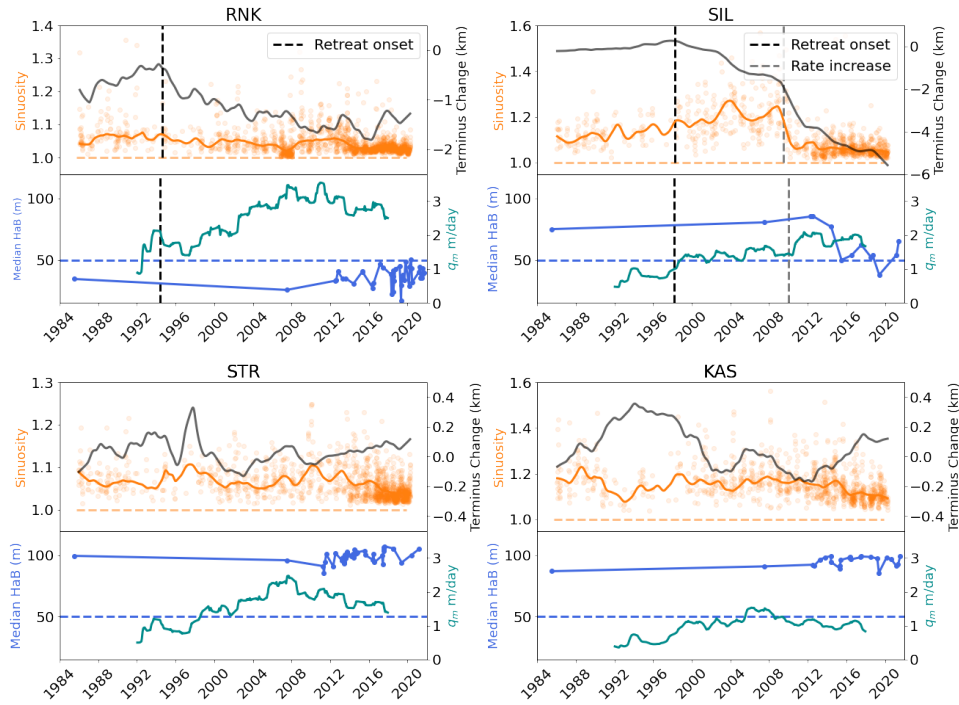


Figure 4.9: Sinuosity (orange lines/dots) compared to terminus change (black line) parameterized submarine melting (teal line), height above buoyancy (H_{ab} ; blue dots/line) for the four main glaciers used in this study. The H_{ab} value of 50 m reflects the local ellipsoid height. Thus, values above 50 m are interpreted as grounded and values below 50 m are interpreted as floating. Sinuosity values for each terminus trace are given as orange dots and the long-term smoothed sinuosity is provided as the solid orange line. Values closer to/further from 1 represent smooth/crenulated terminus morphologies. For glaciers with a retreating terminus, we delineate the onset of retreat (black vertical dashed lines) and an acceleration in retreat for SIL (gray vertical dashed line).

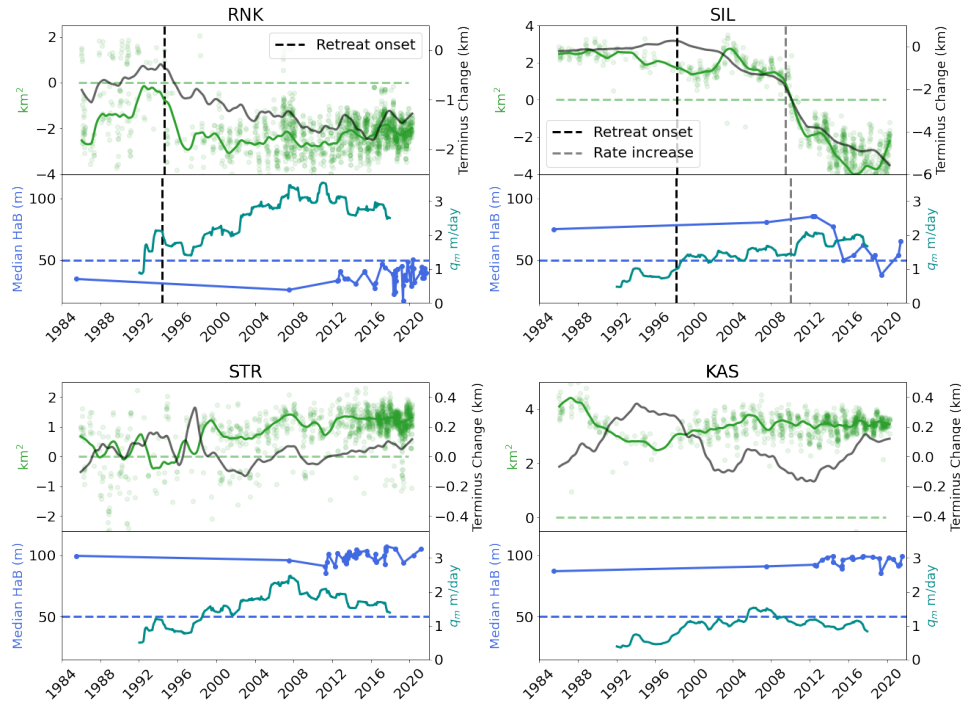


Figure 4.10: Convex hull area (green lines/dots) compared to terminus change (black line), parameterized submarine melting (teal line), height above buoyancy (H_{ab} ; blue line) for the four main glaciers used in this study. The H_{ab} value of 50 m reflects the local ellipsoid height. Thus, values above 50 m are interpreted as grounded and values below 50 m are interpreted as floating. convex values for each terminus trace are given as green dots and the long-term smoothed convex is provided as the solid green line. Positive/negative convex values represent convex/concave terminus morphologies. For glaciers with a retreating terminus, we delineate the onset of retreat (black vertical dashed lines) and an acceleration in retreat for SIL (gray vertical dashed line).

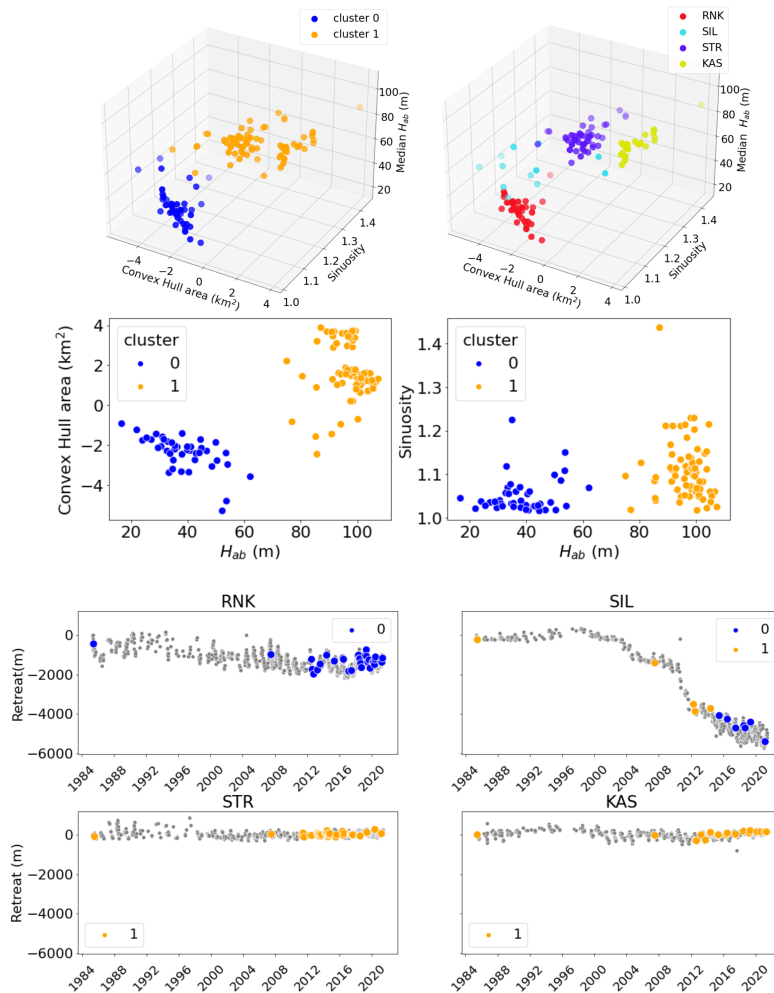


Figure 4.11: Top: 3D Results from the k-means clustering analysis for H_{ab} , convex hull area, and sinuosity. Top Left: Data points colored by assigned clusters 0 and 1. Top right: Data points colored by Glacier. Middle: Convex hull area and sinuosity vs. H_{ab} colored by clusters assigned from 3D cluster analysis. Bottom: Terminus change over time colored by assigned cluster for each glacier used in this study.

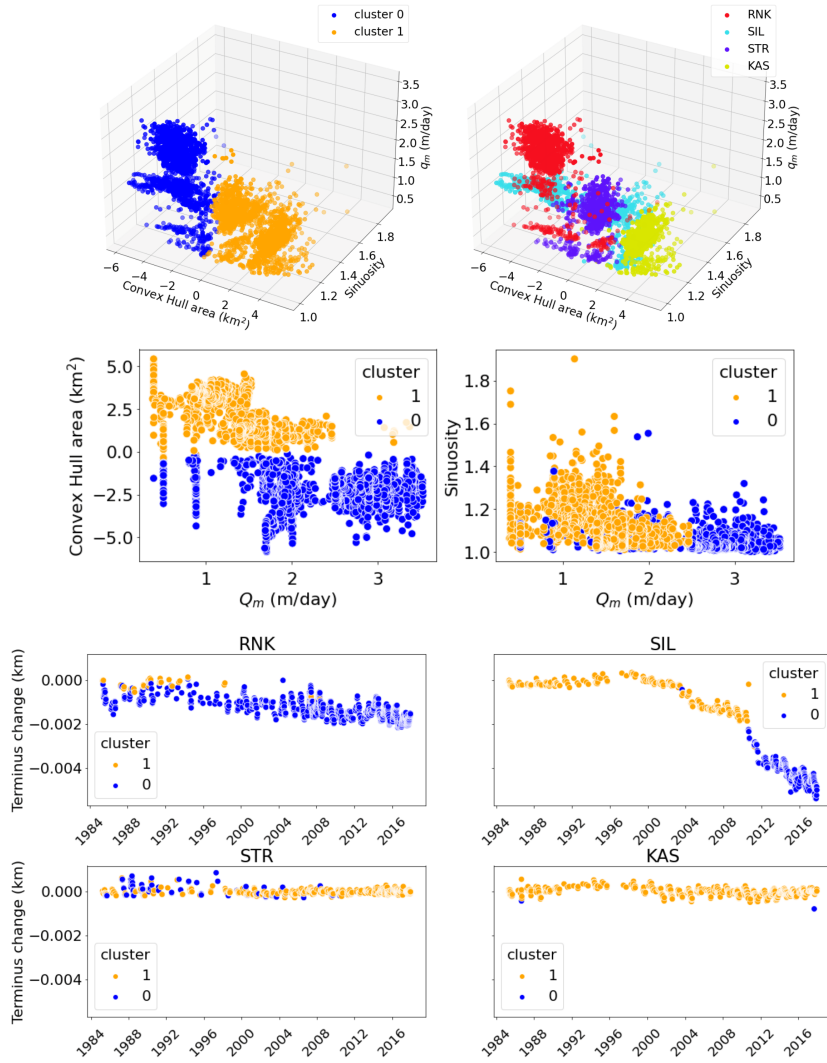


Figure 4.12: Top: 3D Results from the k-means clustering analysis for q_m , convex hull area, and sinuosity. Top Left: Data points colored by assigned clusters 0 and 1. Top right: Data points colored by Glacier. Middle: Convex hull area and sinuosity vs. q_m colored by clusters assigned from 3D cluster analysis. Bottom: Terminus change over time colored by assigned cluster for each glacier used in this study.

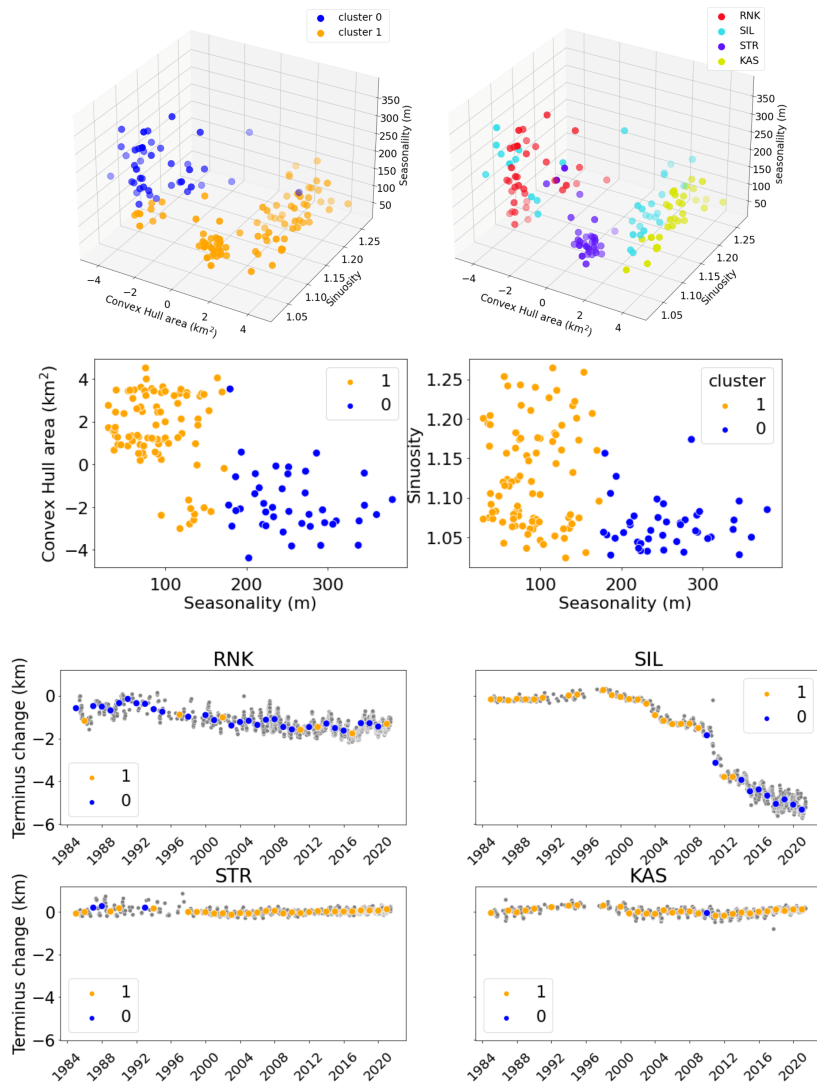


Figure 4.13: Top: 3D Results from the k-means clustering analysis for seasonality, convex hull area, and sinuosity. Top Left: Data points colored by assigned clusters 0 and 1. Top right: Data points colored by Glacier. Middle: Convex hull area and sinuosity vs. H_{ab} colored by clusters assigned from 3D cluster analysis. Bottom: Terminus change over time colored by assigned cluster for each glacier used in this study.

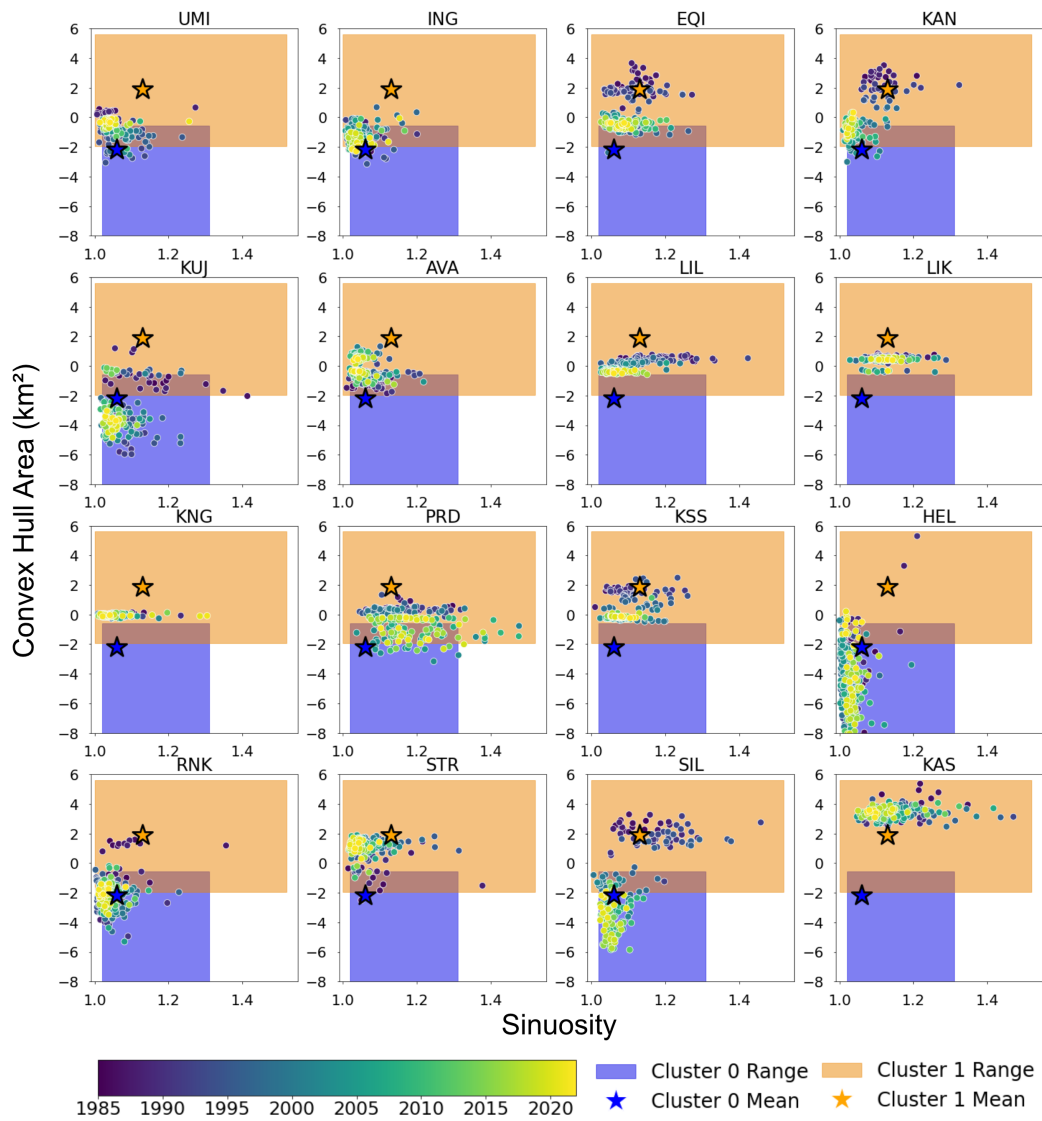


Figure 4.14: Convex Hull area vs. Sinuosity the supplemental glaciers and the original four glaciers used in the morphology analysis. The blue/orange shading are the mean ranges for Convex hull area and Sinuosity for cluster 0/1 determined from from all three cluster analyses. The blue/orange stars are the mean values for cluster 1/2 from all three cluster analyses(see Table 4.4).

4.6 Supplemental Materials

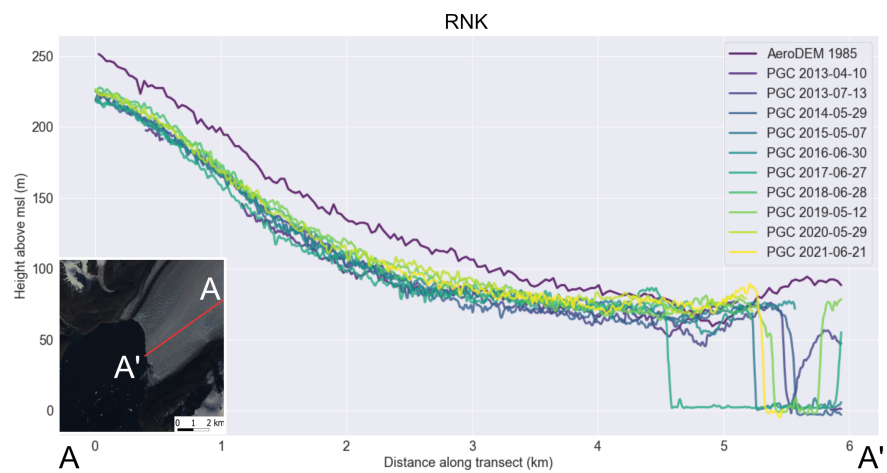


Figure 4.15: Select transects (~ 1 per year) for RNK Glacier.

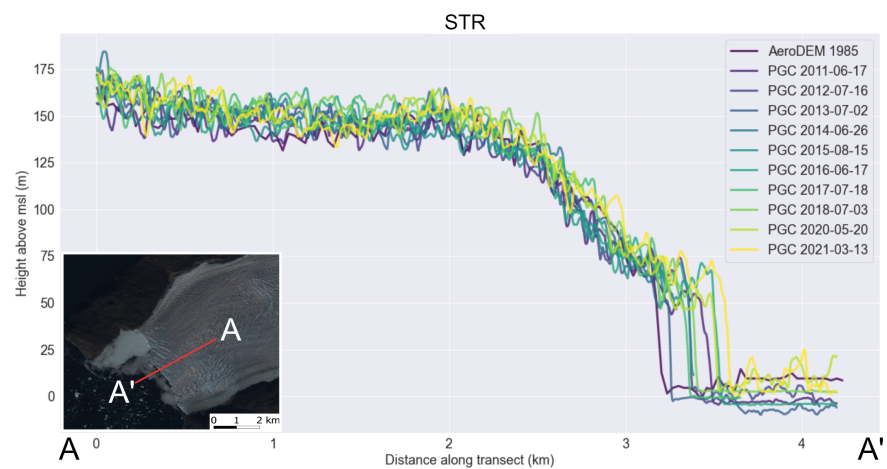


Figure 4.16: Select transects (~ 1 per year) for STR Glacier.

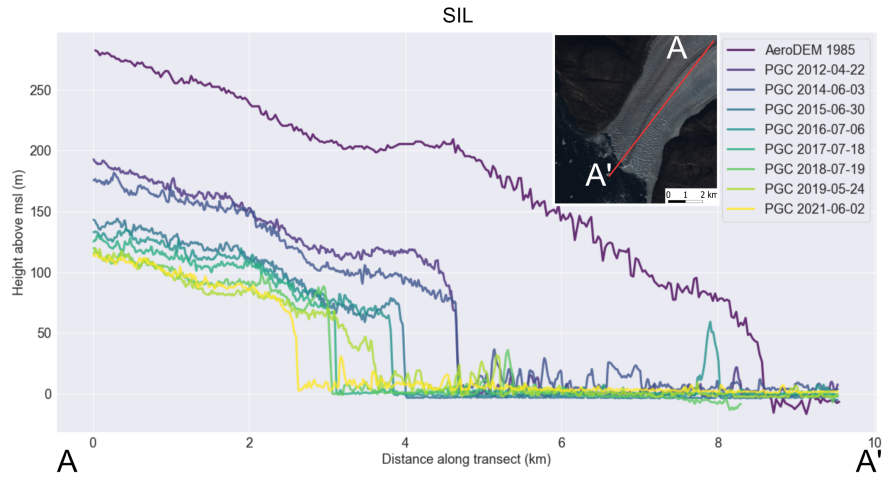


Figure 4.17: Select transects (~ 1 per year) for SIL Glacier.

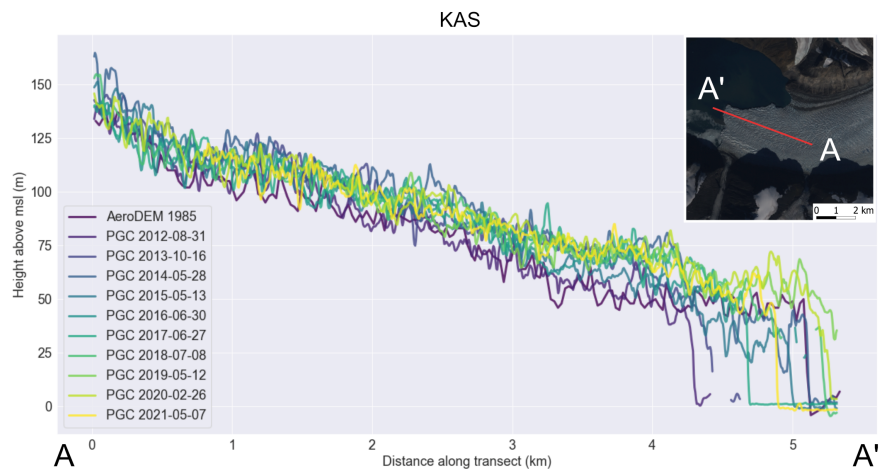


Figure 4.18: Select transects (~ 1 per year) for KAS Glacier.



Figure 4.19: Thermal forcing (TF) from *Wood et al.* (2021a), subglacial discharge from *Mankoff et al.* (2021), Terminus depth from (*Morlighem et al.*, 2017), and calculated Q_m for RNK glacier.

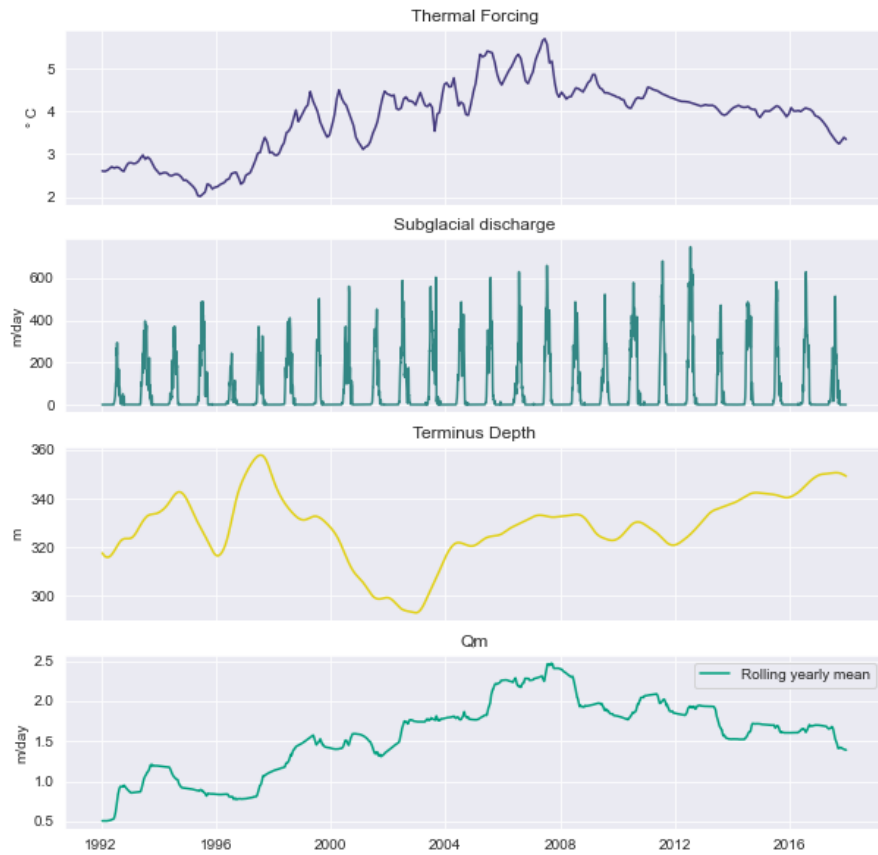


Figure 4.20: Thermal forcing (TF) from *Wood et al.* (2021a), subglacial discharge from *Mankoff et al.* (2021), Terminus depth from (*Morlighem et al.*, 2017), and calculated Q_m for STR glacier.

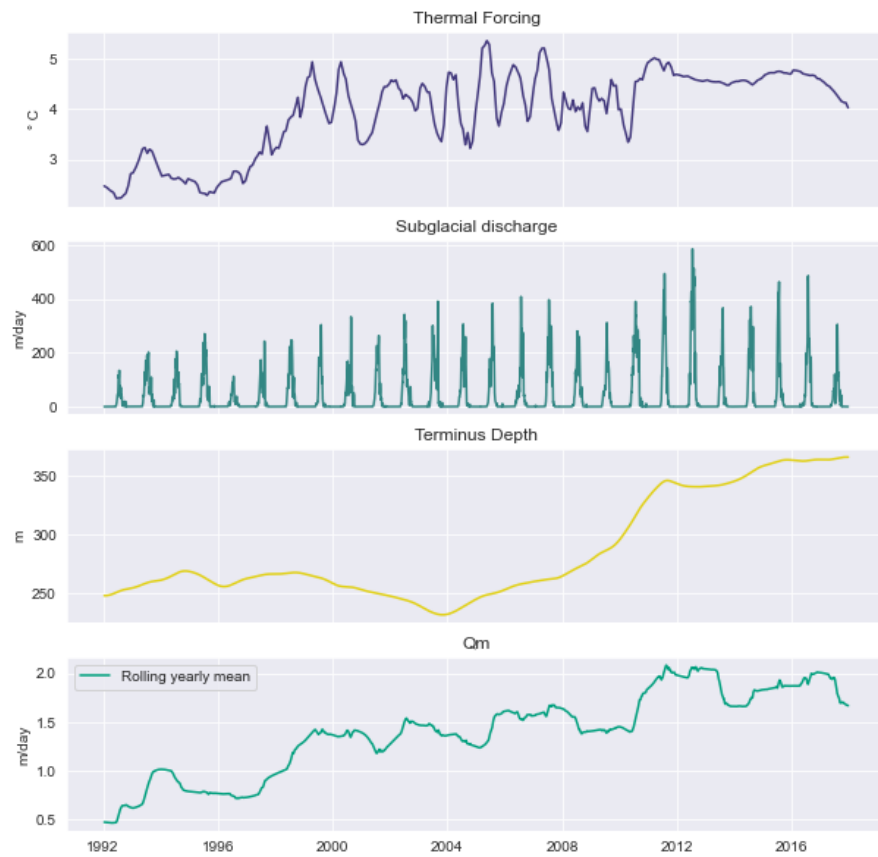


Figure 4.21: Thermal forcing (TF) from *Wood et al.* (2021a), subglacial discharge from *Mankoff et al.* (2021), Terminus depth from (*Morlighem et al.*, 2017), and calculated Q_m for SIL glacier.



Figure 4.22: Thermal forcing (TF) from *Wood et al.* (2021a), subglacial discharge from *Mankoff et al.* (2021), Terminus depth from (*Morlighem et al.*, 2017), and calculated Q_m for KAS glacier.

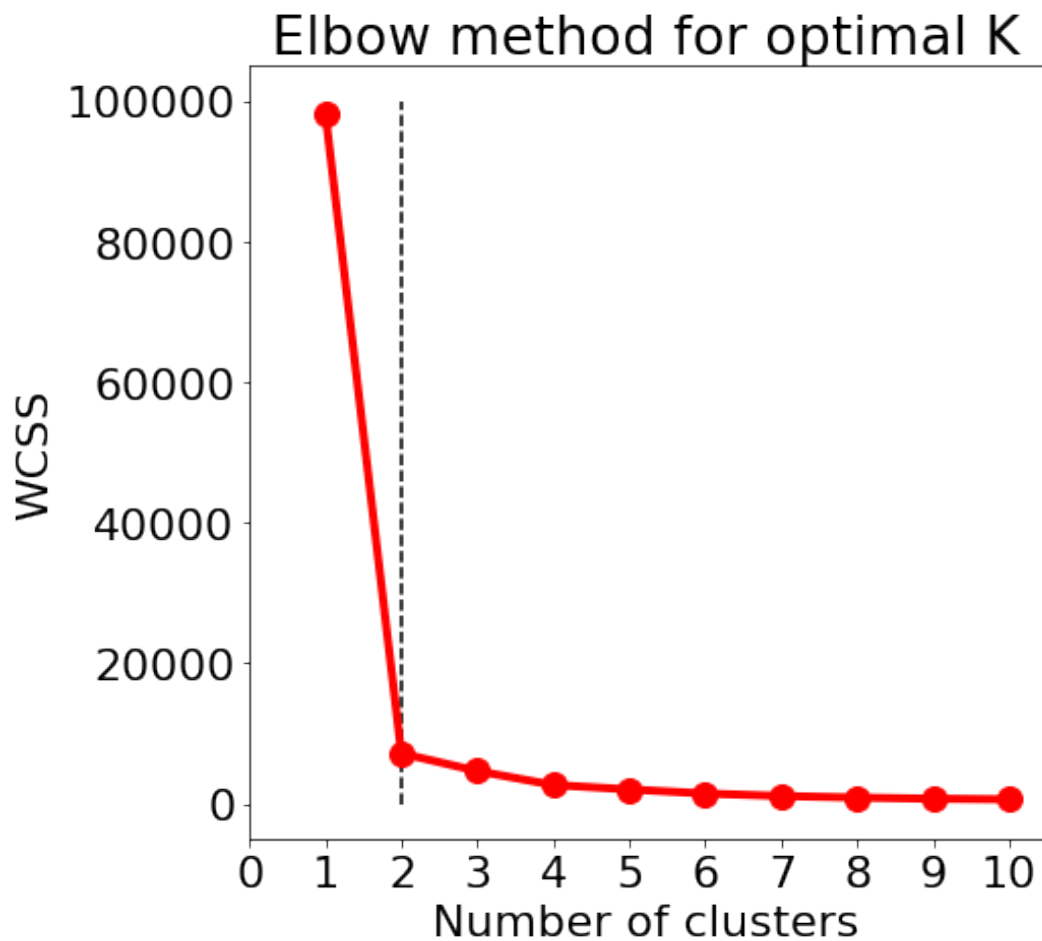


Figure 4.23: Within Cluster Sum of Squares (WCSS) for values 1-11 of k for our k-means clustering of convex hull area, sinuosity, and H_{ab} . A lower value indicates less variance within each cluster and better clustering of the data. We used the elbow method to choose our optimal cluster (black dashed line).

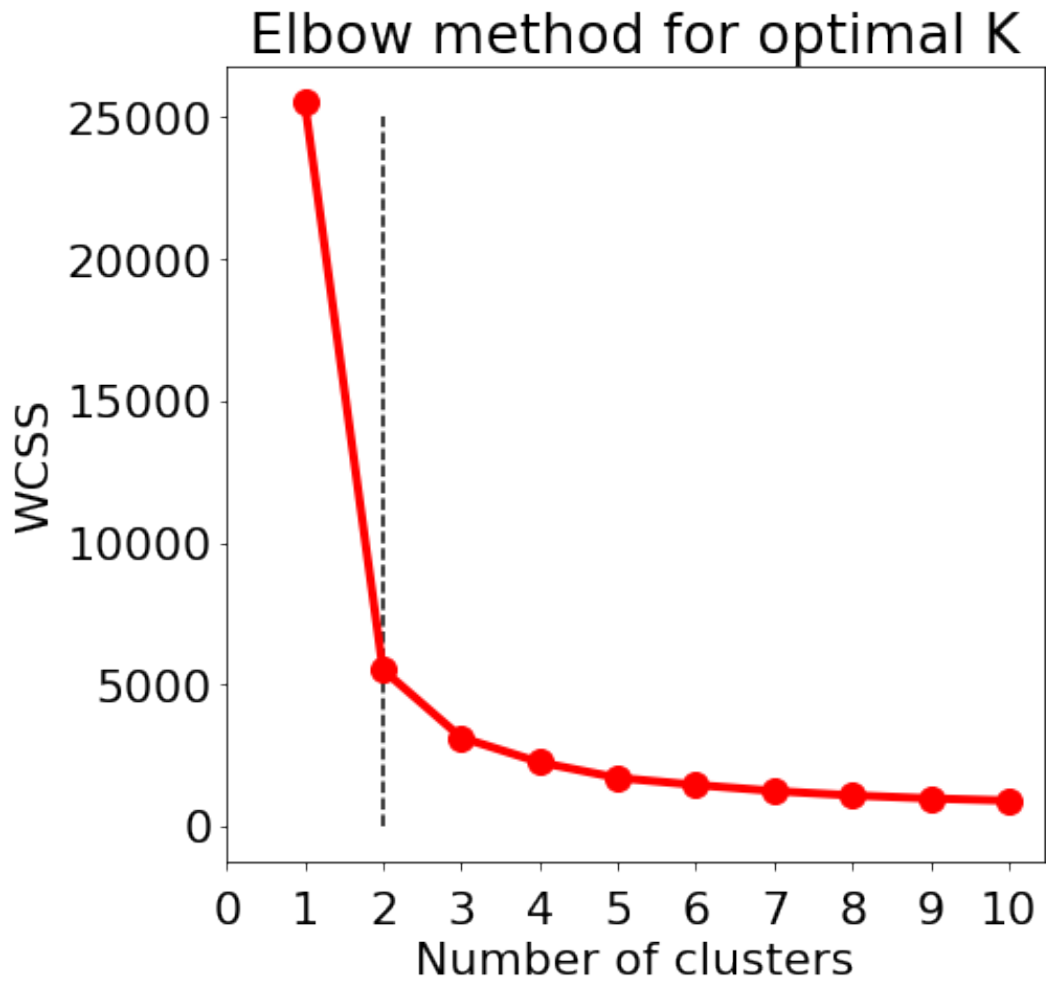


Figure 4.24: Within Cluster Sum of Squares (WCSS) for values 1-11 of k for our k-means clustering of convex hull area, sinuosity, and q_m . A lower value indicates less variance within each cluster and better clustering of the data. We used the elbow method to choose our optimal cluster (black dashed line).

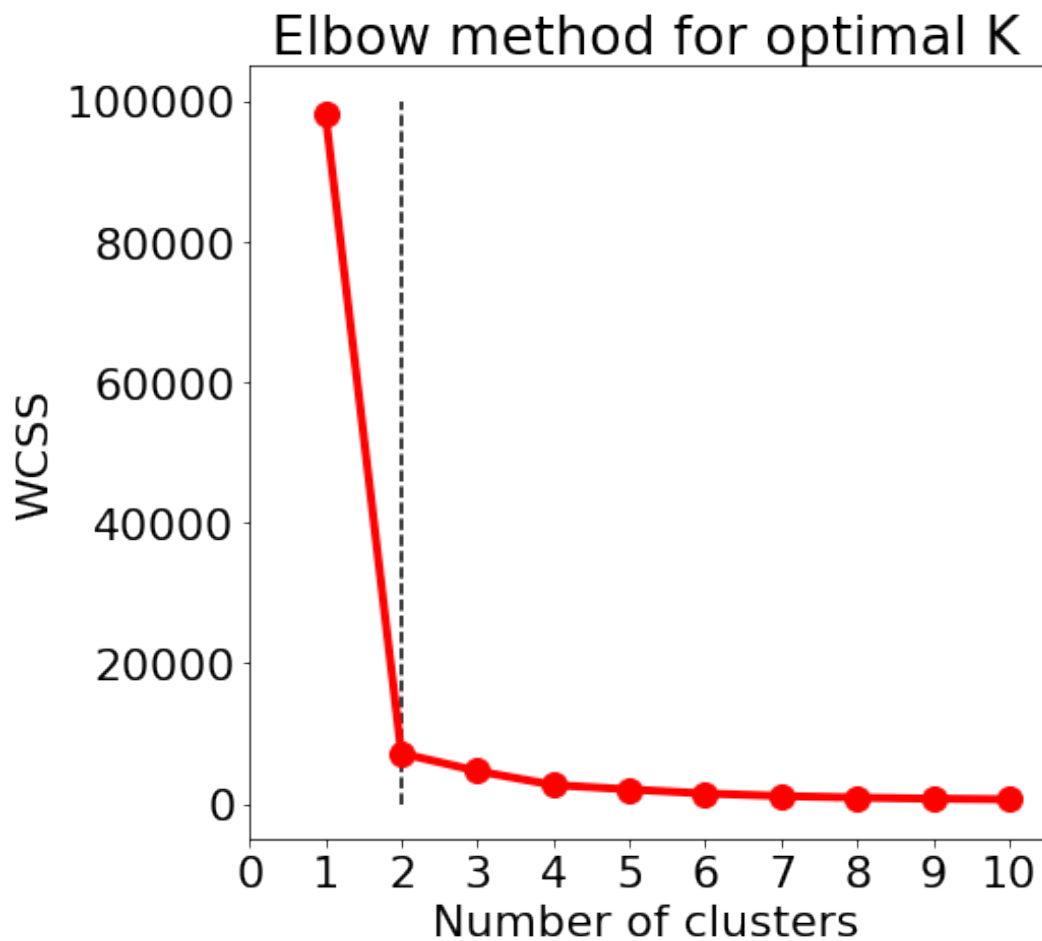


Figure 4.25: Within Cluster Sum of Squares (WCSS) for values 1-11 of k for our k-means clustering of convex hull area, sinuosity, and seasonality. A lower value indicates less variance within each cluster and better clustering of the data. We used the elbow method to choose our optimal cluster (black dashed line).

DEM Name	DEM Date	Median Hab	STD Hab	Mean Bed Error
SETSM_s2s041_WV02_20120713_103001001955A600_103001001A042600	2012-07-13	33	57	40
SETSM_s2s041_WV02_20120812_103001001A817700_103001001ABBE100	2012-08-12	33	52	55
SETSM_s2s041_WV01_20121017_102001001D504B00_102001001C5FD100	2012-10-17	40	48	61
SETSM_s2s041_WV01_20130410_1020010020E0A700_10200100210AC200	2013-04-10	34	57	45
SETSM_s2s041_WV01_20130811_10200100246F0C00_1020010026D4DA00	2013-08-11	34	52	47
SETSM_s2s041_WV01_20140529_102001002F49A500_102001002D10C500	2014-05-29	30	53	44
SETSM_s2s041_WV03_20150507_104001000BAA0C00_104001000BA42700	2015-05-07	40	57	37
SETSM_s2s041_WV01_20150513_102001003D230D00_102001003DEBD400	2015-05-13	39	56	42
SETSM_s2s041_WV02_20160529_103001005723FF00_1030010056D69300	2016-05-29	27	54	39
SETSM_s2s041_WV01_20160630_102001004E059E00_102001004F777F00	2016-06-30	31	54	35
SETSM_s2s041_WV03_20170225_10400100293C4200_1040010029248200	2017-02-25	46	51	48
SETSM_s2s041_WV02_20170627_103001006BA77A00_103001006D73DE00	2017-06-27	43	44	65
SETSM_s2s041_WV02_20180410_103001007B0D4E00_103001007C6AD100	2018-04-10	38	50	49
SETSM_s2s041_WV02_20180511_103001007D576F00_103001007E30CA00	2018-05-11	22	55	29
SETSM_s2s041_WV02_20180628_10300100802B6700_103001007F62A600	2018-06-28	41	56	32
SETSM_s2s041_WV02_20180628_1030010082538300_1030010081462B00	2018-06-28	36	54	38
SETSM_s2s041_WV02_20180708_103001007FA72500_103001008234BB00	2018-07-08	24	53	37
SETSM_s2s041_WV02_20180815_10300100835A9400_1030010080988600	2018-08-15	32	53	38
SETSM_s2s041_WV02_20180922_1030010084D75A00_1030010085722000	2018-09-22	42	53	50
SETSM_s2s041_WV02_20190309_103001008C691C00_103001008EB9BB00	2019-03-09	44	52	44
SETSM_s2s041_WV03_20190430_104001004B1BBD00_104001004A13B600	2019-04-30	16	52	27
SETSM_s2s041_WV03_20190512_104001004CC0E600_104001004B1CFD00	2019-05-12	29	54	29
SETSM_s2s041_WV01_20190701_102001008A9F5200_10200100868F5E00	2019-07-01	38	56	35
SETSM_s2s041_WV03_20190709_104001004FCBD100_104001004E11EA00	2019-07-09	35	56	31
SETSM_s2s041_WV03_20190901_104001004F77E900_104001004FBD6800	2019-09-01	33	52	42
SETSM_s2s041_WV02_20191016_103001009B73F700_1030010099D7C100	2019-10-16	48	52	48
SETSM_s2s041_WV03_20200226_10400100597B4500_10400100570C0E00	2020-02-26	28	52	40
SETSM_s2s041_WV01_20200320_102001009768F900_102001009837F000	2020-03-20	44	52	53
SETSM_s2s041_WV02_20200506_10300100A54F6B00_10300100A4B10900	2020-05-06	50	52	41
SETSM_s2s041_WV03_20200529_104001005BB5CD00_104001005CB3D000	2020-05-29	43	53	42
SETSM_s2s041_WV02_20200620_10300100A7970500_10300100A961B000	2020-06-20	31	51	41
SETSM_s2s041_WV03_20210228_1040010063D26B00_10400100669CDE00	2021-02-28	39	52	41
SETSM_s2s041_WV02_20210405_10300100BC1A8C00_10300100BC5ACE00	2021-04-05	44	53	34
SETSM_s2s041_WV03_20210507_1040010067101600_1040010068720100	2021-05-07	35	53	39
SETSM_s2s041_WV03_20210621_104001006939FD00_104001006A1C8800	2021-06-21	35	53	46
SETSM_s2s041_WV02_20210713_10300100C13DB000_10300100C2641200	2021-07-13	38	54	39
SETSM_s2s041_WV01_20210801_10200100B4457A00_10200100B45EDD00	2021-08-01	43	54	44
SETSM_s2s041_WV03_20210923_104001006E360D00_104001006F809600	2021-09-23	39	53	49
AeroDEM	1985	34	55	27
GIMP	2007	25	58	47

Table 4.5: DEMs used for the calculation of H_{ab} for RNK glacier. The median H_{ab} is the median of all values in the stress-coupling length defined by the terminus of the glacier in the DEM. The STD is the standard deviation of the values of H_{ab} within the stress-coupling length. The mean bed error is the mean of all error values defined in the error map of BedMachineV4 (*Morlighem et al.*, 2017) within the stress-coupling length.

DEM Name	DEM Date	Median Hab	STD Hab	Mean Bed Error
SETSM_s2s041_W1W1_20110410_1020010012ADDC00_1020010013D12000	2011-04-10	91	46	48
SETSM_s2s041_W1W2_20110508_1020010012308800_103001000A172900	2011-05-08	85	45	49
SETSM_s2s041_WV01_20110617_1020010012BFF0700_1020010014E01800	2011-06-17	94	47	47
SETSM_s2s041_WV01_20110802_10200100151E5600_1020010015A67800	2011-08-02	100	45	49
SETSM_s2s041_WV01_20120422_102001001B98DB00_102001001A22A600	2012-04-22	90	48	45
SETSM_s2s041_WV01_20120716_102001001CC9A400_102001001E05D900	2012-07-16	101	46	49
SETSM_s2s041_WV01_20130318_1020010021C6C800_1020010020362600	2013-03-18	95	49	45
SETSM_s2s041_WV01_20130415_1020010022209C00_102001002061B000	2013-04-15	98	46	47
SETSM_s2s041_WV02_20130415_103001002260B500_103001002174F900	2013-04-15	97	46	47
SETSM_s2s041_WV02_20130531_1030010023D67900_10300100240CC200	2013-05-31	93	46	44
SETSM_s2s041_WV02_20130614_1030010023D78500_1030010023A8A600	2013-06-14	94	51	43
SETSM_s2s041_WV01_20130702_102001002297C800_1020010022E82000	2013-07-02	100	48	48
SETSM_s2s041_WV01_20130722_1020010024DBA200_10200100246C5400	2013-07-22	97	47	46
SETSM_s2s041_WV02_20130915_103001002790CB00_1030010026660900	2013-09-15	100	47	49
SETSM_s2s041_WV02_20131006_1030010027278600_103001002865E000	2013-10-06	103	47	49
SETSM_s2s041_WV01_20140327_102001002C986700_102001002CA57300	2014-03-27	99	47	47
SETSM_s2s041_WV02_20140414_103001002F9FC100_103001002F05C100	2014-04-14	100	51	42
SETSM_s2s041_WV02_20140430_1030010030285E00_103001003030A800	2014-04-30	101	48	46
SETSM_s2s041_WV02_20140602_1030010032357100_103001003224CC00	2014-06-02	98	49	44
SETSM_s2s041_WV01_20140608_102001002FD32100_102001002FA41200	2014-06-08	99	50	44
SETSM_s2s041_WV01_20140626_1020010031EA9100_102001002F0DE800	2014-06-26	104	50	45
SETSM_s2s041_WV01_20140720_10200100315AFC00_102001003162A700	2014-07-20	103	47	48
SETSM_s2s041_WV01_20140811_1020010032A15E00_1020010033BF1A00	2014-08-11	101	45	49
SETSM_s2s041_WV02_20140828_10300100367DA600_103001003751AE00	2014-08-28	102	46	49
SETSM_s2s041_WV02_20140923_10300100387A6D00_1030010037B99800	2014-09-23	101	47	46
SETSM_s2s041_WV01_20141008_102001003469FB00_1020010032222200	2014-10-08	102	49	46
SETSM_s2s041_WV03_20150715_104001000E86DA00_104001000F76DE00	2015-07-15	103	44	48
SETSM_s2s041_WV02_20150815_1030010047D4D000_10300100479D5C00	2015-08-15	100	46	48
SETSM_s2s041_WV02_20160515_10300100565FE600_10300100553A6400	2016-05-15	96	49	43
SETSM_s2s041_WV01_20160617_1020010051943500_102001005112B900	2016-06-17	101	48	47
SETSM_s2s041_WV02_20160724_10300100591B8100_1030010058A66100	2016-07-24	94	48	47
SETSM_s2s041_WV02_20170510_1030010069734100_1030010068246100	2017-05-10	99	44	46
SETSM_s2s041_WV02_20170612_103001006A5E1800_103001006987C000	2017-06-12	92	49	40
SETSM_s2s041_WV02_20170714_103001006B93BE00_103001006C0DB500	2017-07-14	106	47	48
SETSM_s2s041_WV01_20170715_10200100632D3400_1020010064E30F00	2017-07-15	104	46	48
SETSM_s2s041_WV01_20170718_102001006248CF00_102001006472D600	2017-07-18	103	45	48
SETSM_s2s041_WV02_20170815_103001006E79A700_103001006F211800	2017-08-15	107	48	47
SETSM_s2s041_WV02_20180703_103001007F06F600_1030010080B93C00	2018-07-03	105	48	46
SETSM_s2s041_WV02_20180719_103001008002A200_10300100813FFB00	2018-07-19	105	45	48
SETSM_s2s041_WV01_20190524_1020010087C17900_1020010080686000	2019-05-24	94	49	41
SETSM_s2s041_WV02_20200520_10300100A6435700_10300100A7A3BC00	2020-05-20	100	48	43
SETSM_s2s041_WV01_20210313_10200100A6446C00_10200100A89C3600	2021-03-13	105	46	46
AeroDEM	1985-07-02	99	44	49
GIMP	2007-07-02	96	45	47

Table 4.6: DEMs used for the calculation of H_{ab} for STR glacier. The median H_{ab} is the median of all values in the stress-coupling length defined by the terminus of the glacier in the DEM. The STD is the standard deviation of the values of H_{ab} within the stress-coupling length. The mean bed error is the mean of all error values defined in the error map of BedMachineV4 (*Morlighem et al.*, 2017) within the stress-coupling length

DEM Name	DEM Date	Median Hab	STD Hab	Mean Bed Error
SETSM_s2s041_WV01_20120422_102001001B98DB00_102001001A22A600	2012-04-22	85	38	54
SETSM_s2s041_WV01_20120708_102001001C1FAD00_102001001C673B00	2012-07-08	85	37	52
SETSM_s2s041_WV02_20140603_10300100320C8F00_10300100326B3200	2014-06-03	76	40	53
SETSM_s2s041_WV01_20150630_102001003FDB1300_10200100410CAB00	2015-06-30	49	42	47
SETSM_s2s041_WV02_20160706_1030010058BBF200_1030010057179E00	2016-07-06	53	44	48
SETSM_s2s041_WV01_20170718_102001006248CF00_102001006472D600	2017-07-18	62	44	46
SETSM_s2s041_WV02_20180719_103001008002A200_10300100813FFB00	2018-07-19	52	40	43
SETSM_s2s041_WV01_20180917_1020010078DD9D00_1020010078486E00	2018-09-17	53	39	39
SETSM_s2s041_WV01_20190524_1020010087C17900_1020010080686000	2019-05-24	37	43	42
SETSM_s2s041_WV03_20210312_10400100653C2600_1040010065B14F00	2021-03-12	54	44	36
SETSM_s2s041_WV02_20210602_10300100BF179000_10300100BF4D2400	2021-06-02	65	44	36
AeroDEM	1985	75	23	72
GIMP	2007	80	41	85

Table 4.7: DEMs used for the calculation of H_{ab} for SIL glacier. The median H_{ab} is the median of all values in the stress-coupling length defined by the terminus of the glacier in the DEM. The STD is the standard deviation of the values of H_{ab} within the stress-coupling length. The mean bed error is the mean of all error values defined in the error map of BedMachineV4 (*Morlighem et al.*, 2017) within the stress-coupling length

DEM Name	DEM Date	Median Hab	STD Hab	Mean Bed Error
SETSM_s2s041_WV02_20120713_103001001A63A400_103001001A686F00	2012-07-13	92	38	38
SETSM_s2s041_WV01_20120831_102001001C999A00_102001001CC47600	2012-08-31	91	37	36
SETSM_s2s041_WV01_20130330_10200100209F7100_102001002177FA00	2013-03-30	96	42	39
SETSM_s2s041_WV02_20131016_10300100286EF100_1030010028CD9900	2013-10-16	98	40	40
SETSM_s2s041_WV02_20140528_103001003241D500_103001003105BD00	2014-05-28	99	45	36
SETSM_s2s041_WV01_20140529_102001002F49A500_102001002D10C500	2014-05-29	94	44	36
SETSM_s2s041_WV03_20150507_104001000BAA0C00_104001000BA42700	2015-05-07	89	36	37
SETSM_s2s041_WV03_20150513_104001000BD5B900_104001000BD16500	2015-05-13	91	46	37
SETSM_s2s041_WV02_20150522_1030010042BFD700_103001004219A000	2015-05-22	96	45	38
SETSM_s2s041_WV02_20160420_103001005499F200_103001005461B600	2016-04-20	98	46	35
SETSM_s2s041_WV02_20160602_103001005797AD00_103001005773DF00	2016-06-02	98	44	37
SETSM_s2s041_WV01_20160630_102001005011B200_1020010052116700	2016-06-30	96	43	37
SETSM_s2s041_WV02_20170627_103001006BA77A00_103001006D73DE00	2017-06-27	98	41	38
SETSM_s2s041_WV03_20170703_104001002E17FE00_104001002F875700	2017-07-03	99	41	37
SETSM_s2s041_WV02_20180708_103001007FA72500_103001008234BB00	2018-07-08	98	42	36
SETSM_s2s041_WV02_20190315_103001008E3CE600_103001008F4EEC00	2019-03-15	97	45	35
SETSM_s2s041_WV03_20190512_104001004CC0E600_104001004B1CFD00	2019-05-12	85	26	35
SETSM_s2s041_WV03_20200226_10400100597B4500_10400100570C0E00	2020-02-26	98	43	37
SETSM_s2s041_WV02_20200823_10300100ABB8CC00_10300100AC0CEB00	2020-08-23	96	39	38
SETSM_s2s041_WV03_20210228_1040010063D26B00_10400100669CDE00	2021-02-28	91	32	37
SETSM_s2s041_WV03_20210507_1040010067101600_1040010068720100	2021-05-07	92	34	36
SETSM_s2s041_WV01_20210801_10200100B4457A00_10200100B45EDD00	2021-08-01	99	40	38
AeroDEM	1985-07-02	87	47	33
GIMP	2007-07-02	91	39	35

Table 4.8: DEMs used for the calculation of H_{ab} for KAS glacier. The median H_{ab} is the median of all values in the stress-coupling length defined by the terminus of the glacier in the DEM. The STD is the standard deviation of the values of H_{ab} within the stress-coupling length. The mean bed error is the mean of all error values defined in the error map of BedMachineV4 (*Morlighem et al.*, 2017) within the stress-coupling length.

Chapter 5

Conclusions

Synthesis

This dissertation focuses on the importance of observing the terminus of Greenland glaciers over time and the utility of the remote sensing record for understanding heterogeneity in terminus change between glaciers. Terminus trace data will continue to be one of the most extensive and robust records of glacier change because we have access to daily satellite imagery over the ice sheet. At the same time, understanding why and how the terminus changes continues to be a challenging aspect of ice sheet models, with most parameterizations unable to capture the complexity of observed terminus change. In studying how the terminus changes over time compared to external forcing and internal glacier dynamics, we are able to move toward a better understanding of marine-terminating glaciers.

Although the importance of the terminus has been well studied in the literature, historically there was no effort to attempt to synthesize the state of terminus trace records and then, in turn, use the terminus data itself to classify glaciers using this extensive record. To this end, I have developed the largest known compilation of terminus data that has been collated, cleaned,

and associated with proper metadata for more efficient and practical use by the scientific community. In fact, this data set has been used as training data in recent work to identify calving fronts in Greenland using radar imagery and has improved this model (*Zhang et al.*, 2021). In examining the biases inherent in the terminus data digitized by hand, we have also presented the ideal methodology for tracing future termini. I will continue to curate and update this database to ensure continued usefulness of terminus data for both scientific and machine learning users.

The TermPicks data set was then used to examine the morphological variability across bed topographic features where glaciers have experienced standstills. I find that the bed features at standstills that eventually led to terminus retreat (termed transient standstills) were smaller, more heterogeneous in shape, and less steep than the bed features at persistent standstills. The heterogeneity in bed feature shape across the width of the fjord, the initial position of a glacier on the prograde or retrograde side, and the distance to a local bed peak may determine if a glacier may retreat given a climate perturbation. Although the sample size of this study is small due to data limitations, this study highlights the need for more high-resolution surveys of the glacier terminus region, particularly at persistent termini, to capture the complex geometries of bed features at standstills.

Finally, I use the distinctive morphology of glacier termini in map-view to categorize glaciers into different calving styles based on previous work (*Chauch et al.*, 2014; *Fried et al.*, 2018; *van Dongen et al.*, 2021). I find that

the convexity/concavity and the sinuosity of a glacier terminus are highly indicative of the flotation conditions and, therefore, its tendency to calve via buoyant flexure. This allows me to cluster glaciers with smooth, concave termini such as buoyant flexure-type glaciers and sinuous, convex termini as those that calve via serac failure related to melt-induced undercutting. I also find that some glaciers defy categorization into each of these end members and may switch calving styles over time, as reflected in the terminus morphology over time. This work highlights the usefulness of terminus observations in determining calving styles so that we may improve parameterizations of calving in ice sheet models.

Future work

Future work will be carried out to improve the robustness of our morphology proxy to develop a decision tree-type parameterization of calving laws for ice sheet models. A significant improvement to our study will be the inclusion of additional elevation data for the calculation of H_{ab} for additional glaciers. The University of Texas Glaciology group has begun to process ASTER digital elevation models in our study area, which will increase the data available to determine flotation conditions. Furthermore, we know that glaciers undergo a seasonal cycle of advance and retreat, and these short-term changes can impact glacier mass loss in the long term (*Moon and Joughin, 2008; Howat et al., 2010; Fried et al., 2018*). Therefore, I also plan to perform a morphology analysis that compares short-term changes in morphology

(subannually) with both parameterized submarine melt and flotation, as I did in Chapter 4. For this study, we will include analysis of the presence of ice melange (*Amundson et al.*, 2010), the presence of subglacial plumes from automated mapping (*McGrath et al.*, 2010; *Tedstone and Arnold*, 2012), and the improved routing of subglacial melt water (*Jenkins*, 2011; *Jackson et al.*, 2019; *Slater et al.*, 2022; *Fried et al.*, 2015) as these are known drivers of seasonal terminus melt, advance, and retreat (*Fried et al.*, 2018).

In Chapter 3, I have shown that the across- and along-fjord variation in bed geometry can impart changes in the morphology of termini and how those termini dynamically adjust over time. 3-D modeling of lateral heterogeneity in bed conditions can help confirm the impact of subglacial topography on calving style. Observations of Humboldt glacier, a large marine-terminating glacier in North Greenland, have shown that the calving style can vary across the terminus (*Carr et al.*, 2015). Furthermore, calving through buoyancy and melt-induced undercutting can arise from variations in buoyancy and undercut melting in 3-D simulations of a marine terminal glacier (*Benn et al.*, 2017b), however, the effect of lateral differences in bed topography on calving style has not been shown in models. Therefore, varying the lateral bed topography in simulations using HiDEM (Helsinki Discrete Element Model) and Elmer/Ice (continuum model) similar to those undertaken by *Benn et al.* (2017b) will further confirm the control of the bed topography in calving styles laterally along a terminus.

Bibliography

- Alberti, M. (2018), Qgis plugin for calculating directional slope, <https://github.com/mauroalberti/directionalslope>.
- Alley, R. B., K. M. Cuffey, E. B. Evenson, J. C. Strasser, D. E. Lawson, and G. J. Larson (1997), How glaciers entrain and transport basal sediment: Physical constraints, *Quaternary Science Reviews*, *16*(9), 1017–1038, doi: 10.1016/S0277-3791(97)00034-6.
- Amaral, T., T. C. Bartholomaeus, and E. M. Enderlin (2019), Evaluation of Iceberg Calving Models Against Observations From Greenland Outlet Glaciers, *Journal of Geophysical Research: Earth Surface*, *125*(6), doi: 10.1029/2019jf005444.
- Amundson, J. M., M. A. Fahnestock, M. Truffer, J. Brown, J. Brown, M. P. Lthi, and R. J. Motyka (2010), Ice mlange dynamics and implications for terminus stability, Jakobshavn Isbr, Greenland, *Journal of Geophysical Research*, *115*(F1), F01,005, doi:10.1029/2009jf001405.
- Andersen, J. K., R. S. Fausto, K. Hansen, J. E. Box, S. B. Andersen, A. Ahlstrom, D. v. As, M. Citterio, W. Colgan, N. B. Karlsson, K. K. Kjellerup, N. J. Korsgaard, S. H. Larsen, K. D. Mankoff, A. Pedersen, C. L. Shields, A. M. Solgaard, and B. Vandecrux (2019), Update of annual

- calving front lines for 47 marine terminating outlet glaciers in Greenland (19992018), *Geological Survey of Denmark and Greenland Bulletin*, 43, 1 – 6, doi:10.34194/geusb-201943-02-02.
- Arndt, J. E., W. Jokat, B. Dorschel, R. Myklebust, J. A. Dowdeswell, and J. Evans (2015), A new bathymetry of the northeast greenland continental shelf: Constraints on glacial and other processes, *Geochemistry, Geophysics, Geosystems*, 16(10), 3733–3753, doi:10.1002/2015GC005931, _eprint: <https://onlinelibrary.wiley.com/doi/pdf/10.1002/2015GC005931>.
- Aschwanden, A., M. A. Fahnestock, M. Truffer, D. J. Brinkerhoff, R. Hock, C. Khroulev, R. H. Mottram, and S. A. Khan (2019), Contribution of the Greenland Ice Sheet to sea level over the next millennium, *Science Advances*, 5(6), doi:10.1126/sciadv.aav9396.
- Astrom, J. A., T. I. Riikil, T. Tallinen, T. Zwinger, D. Benn, J. C. Moore, and J. Timonen (2013), A particle based simulation model for glacier dynamics, *The Cryosphere*, p. 12.
- Bartholomaus, T. C., C. F. Larsen, and S. O’Neel (2013), Does calving matter? Evidence for significant submarine melt, *Earth and Planetary Science Letters*, 380, 21 – 30, doi:10.1016/j.epsl.2013.08.014.
- Bartholomaus, T. C., L. A. Stearns, D. A. Sutherland, E. L. Shroyer, J. D. Nash, R. T. Walker, G. A. Catania, D. Felikson, D. Carroll, M. J. Fried, B. P. Y. Nol, and M. R. v. d. Broeke (2016), Contrasts in the response of

- adjacent fjords and glaciers to ice-sheet surface melt in West Greenland, *Annals of Glaciology*, pp. 1 – 14, doi:10.1017/aog.2016.19.
- Bassis, J. N., and S. Jacobs (2013), Diverse calving patterns linked to glacier geometry, *Nature Geoscience*, *6*(10), 833 – 836, doi:10.1038/ngeo1887.
- Batchelor, C. L., J. A. Dowdeswell, E. Rignot, and R. Millan (2019), Submarine moraines in southeast greenland fjords reveal contrasting outlet-glacier behavior since the last glacial maximum, *Geophysical Research Letters*, *46*(6), 3279–3286, doi:10.1029/2019GL082556, eprint: <https://onlinelibrary.wiley.com/doi/pdf/10.1029/2019GL082556>.
- Baumhoer, C. A., A. J. Dietz, C. Kneisel, and C. Kuenzer (2019), Automated Extraction of Antarctic Glacier and Ice Shelf Fronts from Sentinel-1 Imagery Using Deep Learning, *Remote Sensing*, *11*(21), 2529 – 22, doi: 10.3390/rs11212529.
- Benn, D. I., N. R. J. Hulton, and R. H. Mottram (2007), 'Calving laws', 'sliding laws' and the stability of tidewater glaciers, *Annals of Glaciology*, *46*, 123 – 130.
- Benn, D. I., J. A. Strm, T. Zwinger, J. Todd, F. M. Nick, S. Cook, N. R. J. Hulton, and A. J. Luckman (2017a), Melt-under-cutting and buoyancy-driven calving from tidewater glaciers: new insights from discrete element and continuum model simulations, *Journal of Glaciology*, *63*(240), 691 – 702, doi:10.1017/jog.2017.41.

- Benn, D. I., T. R. Cowton, J. Todd, and A. J. Luckman (2017b), Glacier Calving in Greenland, *Current Climate Change Reports*, 3(4), 1–9, doi:10.1007/s40641-017-0070-1.
- Bevan, S. L., A. J. Luckman, and T. Murray (2012), Glacier dynamics over the last quarter of a century at Helheim, Kangerdlugssuaq and 14 other major Greenland outlet glaciers, *The Cryosphere*, 6(5), 923 – 937, doi:10.5194/tc-6-923-2012.
- Bevan, S. L., A. J. Luckman, D. I. Benn, T. Cowton, and J. Todd (2019), Impact of warming shelf waters on ice mélange and terminus retreat at a large SE Greenland glacier, *The Cryosphere*, 13(9), 2303–2315, doi:10.5194/tc-13-2303-2019.
- Bierman, P. R., J. D. Shakun, L. B. Corbett, S. R. H. Zimmerman, and D. H. Rood (2016), A persistent and dynamic East Greenland Ice Sheet over the past 7.5 million years, *Nature Communications*, 540(7632), 256 – 260, doi:10.1038/nature20147.
- Bjørk, A. A., K. H. Kjær, N. J. Korsgaard, S. A. Khan, K. K. Kjellerup, C. S. Andresen, J. E. Box, N. K. Larsen, and S. Funder (2012), An aerial view of 80 years of climate-related glacier fluctuations in southeast Greenland, *Nature Geoscience*, 5(6), 427 – 432, doi:10.1038/ngeo1481.
- Bjørk, A. A., L. M. Kruse, and P. B. Michaelsen (2015), Brief communication: Getting Greenland’s glaciers right – a new data set of all offi-

- cial Greenlandic glacier names, *The Cryosphere*, 9(6), 2215 – 2218, doi: 10.5194/tc-9-2215-2015-supplement.
- Black, T. E., and I. Joughin (), Multi-decadal retreat of marine-terminating outlet glaciers in northwest and central-west greenland, *The Cryosphere*, 16(3), 807–824, doi:10.5194/tc-16-807-2022.
- Briner, J. P., A. C. Bini, and R. S. Anderson (2009), Rapid early Holocene retreat of a Laurentide outlet glacier through an Arctic fjord, *Nature Geoscience*, 2(7), 496 – 499, doi:10.1038/ngeo556.
- Brinkerhoff, D. J., M. Truffer, and A. Aschwanden (2017), Sediment transport drives tidewater glacier periodicity, *Nature Communications*, 8(1), 91, doi: 10.1038/s41467-017-00095-5.
- Broeke, M. R. v. d., E. M. Enderlin, I. M. Howat, P. K. Munneke, B. P. Y. Nol, W. J. v. D. Berg, E. v. Meijgaard, and B. Wouters (2016), On the recent contribution of the Greenland ice sheet to sea level change, *The Cryosphere*, 10(5), 1933 – 1946, doi:10.5194/tc-10-1933-2016.
- Brough, S., J. R. Carr, N. Ross, and J. M. Lea (2019), Exceptional Retreat of Kangerlussuaq Glacier, East Greenland, Between 2016 and 2018, *Frontiers in Earth Science*, 7(123), 123, doi:10.3389/feart.2019.00123.
- Bunce, C., J. R. Carr, P. W. Nienow, N. Ross, and R. Killick (2018), Ice front change of marine-terminating outlet glaciers in northwest and southeast

- Greenland during the 21st century, *Journal of Glaciology*, 64(246), 523 – 535, doi:10.1017/jog.2018.44.
- Bunce, C., P. Nienow, A. Sole, T. Cowton, and B. Davison (2022), Influence of glacier runoff and near-terminus subglacial hydrology on frontal ablation at a large greenlandic tidewater glacier, *Journal of Glaciology*, p. 11, doi: <https://doi.org/10.1017/jog.2020.109>.
- Carr, J. R., A. Vieli, and C. R. Stokes (2013), Influence of sea ice decline, atmospheric warming, and glacier width on marine-terminating outlet glacier behavior in northwest Greenland at seasonal to interannual timescales, *Journal of Geophysical Research: Earth Surface*, 118(3), 1210 – 1226, doi: 10.1002/jgrf.20088.
- Carr, J. R., C. R. Stokes, and A. Vieli (2014), Recent retreat of major outlet glaciers on Novaya Zemlya, Russian Arctic, influenced by fjord geometry and sea-ice conditions, *Journal of Glaciology*, 60(219), 155 – 170, doi:10.3189/2014jog13j122.
- Carr, J. R., A. Vieli, C. R. Stokes, S. S. R. Jamieson, S. J. Palmer, P. Christoffersen, J. A. Dowdeswell, F. M. Nick, D. D. Blankenship, and D. A. Young (2015), Basal topographic controls on rapid retreat of Humboldt Glacier, northern Greenland, *Journal of Glaciology*, 61(225), 137 – 150, doi:10.3189/2015jog14j128.
- Carr, J. R., C. R. Stokes, and A. Vieli (2017), Threefold increase in marine-

- terminating outlet glacier retreat rates across the Atlantic Arctic: 19922010, *Annals of Glaciology*, 58(74), 72–91, doi:10.1017/aog.2017.3.
- Carroll, D., D. A. Sutherland, E. L. Shroyer, J. D. Nash, G. A. Catania, and L. A. Stearns (2015), Modeling Turbulent Subglacial Meltwater Plumes: Implications for Fjord-Scale Buoyancy-Driven Circulation, *Journal of Physical Oceanography*, 45(8), 2169 – 2185, doi:10.1175/jpo-d-15-0033.1.
- Carroll, D., D. A. Sutherland, B. Hudson, T. Moon, G. A. Catania, E. L. Shroyer, J. D. Nash, T. C. Bartholomaeus, D. Felikson, L. A. Stearns, B. P. Y. Nol, and M. R. Broeke (2016), The impact of glacier geometry on meltwater plume structure and submarine melt in Greenland fjords, *Geophysical Research Letters*, 43(18), 9739–9748, doi:10.1002/2016gl070170.
- Cassotto, R., M. A. Fahnestock, J. M. Amundson, M. Truffer, and I. R. Joughin (2015), Seasonal and interannual variations in ice melange and its impact on terminus stability, Jakobshavn Isbr, Greenland, *Journal of Glaciology*, 61(225), 76 – 88, doi:10.3189/2015jog13j235.
- Castleman, B. A., N.-J. Schlegel, L. Caron, E. Larour, and A. Khazendar (2022), Derivation of bedrock topography measurement requirements for the reduction of uncertainty in ice-sheet model projections of thwaites glacier, *The Cryosphere*, 16(3), 761–778, doi:10.5194/tc-16-761-2022.
- Catania, G. A., L. A. Stearns, D. A. Sutherland, M. J. Fried, T. C. Bartholomaeus, M. Morlighem, E. L. Shroyer, and J. D. Nash (2018), Geometric Controls on Tidewater Glacier Retreat in Central Western Greenland,

Journal of Geophysical Research: Earth Surface, 123, 2024 – 2038, doi:10.1029/2017jf004499.

Chauch, N., A. L. Hubbard, J. C. Gascard, J. E. Box, R. Bates, M. N. Koppes, A. J. Sole, P. Christoffersen, and H. Patton (2014), Iceocean interaction and calving front morphology at two west Greenland tidewater outlet glaciers, *The Cryosphere*, 8(4), 1457 – 1468, doi:10.5194/tc-8-1457-2014.

Cheng, D., W. Hayes, E. Larour, Y. Mohajerani, M. Wood, I. Velicogna, and E. Rignot (2020), Calving Front Machine (CALFIN): Glacial Termini Dataset and Automated Deep Learning Extraction Method for Greenland, 1972-2019, *The Cryosphere*, 2020, 1–17, doi:10.5194/tc-2020-231.

Choi, Y., M. Morlighem, E. Rignot, and M. Wood (2021), Ice dynamics will remain a primary driver of Greenland ice sheet mass loss over the next century, *Nature Communications Earth & Environment*, 2(1), 26, doi:10.1038/s43247-021-00092-z.

Christian, J. E., A. A. Robel, and G. Catania (2022), A probabilistic framework for quantifying the role of anthropogenic climate change in marine-terminating glacier retreats, *The Cryosphere*, doi:10.5194/tc-2021-394.

Christoffersen, P., R. I. Mugford, K. J. Heywood, I. R. Joughin, J. A. Dowdeswell, J. P. Syvitski, A. J. Luckman, and T. J. Benham (2011), Warming of waters in an East Greenland fjord prior to glacier retreat: mechanisms and connection to large-scale atmospheric conditions, *The Cryosphere*, 5(3), 701 – 714, doi:10.5194/tc-5-701-2011.

- Cook, A. J., A. J. Fox, D. G. Vaughan, and J. G. Ferrigno (2005), Retreating Glacier Fronts on the Antarctic Peninsula over the Past Half-Century, *Science*, *308*(5721), 541 – 544.
- Cook, S. J., P. Christoffersen, M. Truffer, T. R. Chudley, and A. Abelln (2021), Calving of a Large Greenlandic Tidewater Glacier has Complex Links to Meltwater Plumes and Mlange, *Journal of Geophysical Research: Earth Surface*, *126*(4), doi:10.1029/2020jf006051.
- Cowton, T. R., P. W. Nienow, I. D. Bartholomew, A. J. Sole, and D. W. F. Mair (2012), Rapid erosion beneath the Greenland ice sheet, *Geology*, *40*(4), 343 – 346, doi:10.1130/g32687.1.
- Cowton, T. R., A. J. Sole, P. W. Nienow, D. A. Slater, and P. Christoffersen (2018), Linear response of east Greenlands tidewater glaciers to ocean/atmosphere warming, *Proceedings of the National Academy of Sciences*, *115*(31), 7907 – 7912, doi:10.1073/pnas.1801769115.
- Csatho, B. M., A. F. Schenk, C. J. v. d. Veen, G. S. Babonis, K. Duncan, S. Rezvanbehbahani, M. R. v. d. Broeke, S. B. Simonsen, S. Nagarajan, and J. H. v. Angelen (2014), Laser altimetry reveals complex pattern of Greenland Ice Sheet dynamics, *Proceedings of the National Academy of Sciences*, *111*(52), 18,478 – 18,483, doi:10.1073/pnas.1411680112.
- Cui, M. (2020), Introduction to the k-means clustering algorithm based on the elbow method, *Accounting, Auditing and Finance*, *1*(1), 5–8, doi:10.23977/accaf.2020.010102, publisher: Clausius Scientific Press.

- Enderlin, E. M., I. M. Howat, and A. Vieli (2013), High sensitivity of tidewater outlet glacier dynamics to shape, *The Cryosphere*, 7(3), 1007 – 1015, doi: 10.5194/tc-7-1007-2013.
- Enderlin, E. M., I. M. Howat, S. Jeong, M.-J. Noh, J. H. v. Angelen, and M. R. v. d. Broeke (2014), An improved mass budget for the Greenland ice sheet, *Geophysical Research Letters*, 41(3), 866 – 872, doi:10.1002/2013gl059010.
- Enderlin, E. M., G. S. Hamilton, F. Straneo, and D. A. Sutherland (2016), Iceberg meltwater fluxes dominate the freshwater budget in Greenland’s icebergcongested glacial fjords, *Geophysical Research Letters*, 43(21), 11,287 – 11,294, doi:10.1002/2016gl070718.
- Fahrner, D., J. M. Lea, S. Brough, D. W. F. Mair, and J. Abermann (2021), Linear response of the Greenland ice sheet’s tidewater glacier terminus positions to climate, *Journal of Glaciology*, 67(262), 193–203, doi: 10.1017/jog.2021.13.
- Felikson, D., T. C. Bartholomaus, G. A. Catania, N. J. Korsgaard, K. H. Kjr, M. Morlighem, B. P. Y. Nol, M. R. v. d. Broeke, L. A. Stearns, E. L. Shroyer, D. A. Sutherland, and J. D. Nash (2017), Inland thinning on the Greenland ice sheet controlled by outlet glacier geometry, *Nature Geoscience*, 10(5), 366 – 369, doi:10.1038/ngeo2934.
- Felikson, D., G. Catania, T. C. Bartholomaus, M. Morlighem, and B. P. Y. Nol (2021), Steep Glacier Bed Knickpoints Mitigate Inland Thinning in

- Greenland, *Geophysical Research Letters*, 48(2), e2020GL090112, doi:10.1029/2020gl090112.
- Fettweis, X., J. E. Box, C. Agosta, C. Amory, C. Kittel, C. Lang, D. v. As, H. Machguth, and H. Galle (2017), Reconstructions of the 1900–2015 Greenland ice sheet surface mass balance using the regional climate MAR model, *The Cryosphere*, 11(2), 1015 – 1033, doi:10.5194/tc-11-1015-2017.
- Frank, T., H. Kesson, B. de Fleurian, M. Morlighem, and K. H. Nisancioglu (2022), Geometric controls of tidewater glacier dynamics, *The Cryosphere*, 16(2), 581–601, doi:10.5194/tc-16-581-2022, publisher: Copernicus GmbH.
- Frasson, R. P. d. M., T. M. Pavelsky, M. A. Fonstad, M. T. Durand, G. H. Allen, G. Schumann, C. Lion, R. E. Beighley, and X. Yang (2019), Global relationships between river width, slope, catchment area, meander wavelength, sinuosity, and discharge, *Geophysical Research Letters*, 46(6), 3252–3262, doi:10.1029/2019GL082027.
- Fried, M. J., G. A. Catania, T. C. Bartholomaeus, D. Duncan, M. Davis, L. A. Stearns, J. D. Nash, E. L. Shroyer, and D. A. Sutherland (2015), Distributed subglacial discharge drives significant submarine melt at a Greenland tidewater glacier, *Geophysical Research Letters*, 42(21), 9328 – 9336, doi:10.1002/2015gl065806.
- Fried, M. J., G. A. Catania, L. A. Stearns, D. A. Sutherland, T. C. Bartholomaeus, E. L. Shroyer, and J. D. Nash (2018), Reconciling Drivers of Seasonal

- Terminus Advance and Retreat at 13 Central West Greenland Tidewater Glaciers, *Journal of Geophysical Research: Earth Surface*, 115(73), doi: 10.1029/2018jf004628.
- Fried, M. J., D. Carroll, G. A. Catania, D. A. Sutherland, L. A. Stearns, E. L. Shroyer, and J. D. Nash (2019), Distinct frontal ablation processes drive heterogeneous submarine terminus morphology, *Geophysical Research Letters*, doi:10.1029/2019gl083980.
- Gagliardini, O., G. Durand, T. Zwinger, R. C. A. Hindmarsh, and E. LeMeur (2010), Coupling of ice-shelf melting and buttressing is a key process in ice-sheet dynamics, *Geophysical Research Letters*, 37(L14501), 10.1029/2010GL043,334.
- Gillies, S. (2013), The shapely user manual.
- Girod, L., C. Nuth, A. Kb, R. McNabb, and O. Galland (2017-07), MMAS-TER: Improved ASTER DEMs for Elevation Change Monitoring, *Remote Sensing*, 9(7), 704 – 25, doi:10.3390/rs9070704.
- Goelzer, H., S. M. J. Nowicki, A. Payne, and e. al (2020), The future sea-level contribution of the Greenland ice sheet: a multi-model ensemble study of ISMIP6, *The Cryosphere*, doi:10.5194/tc-2019-319.
- Goliber, S., T. Black, G. Catania, J. M. Lea, H. Olsen, D. Cheng, S. Bevan, A. Bjrk, C. Bunce, S. Brough, J. R. Carr, T. Cowton, A. Gardner, D. Fahrner, E. Hill, I. Joughin, N. Korsgaard, A. Luckman, T. Moon,

- T. Murray, A. Sole, M. Wood, and E. Zhang (2022), TermPicks: A century of Greenland glacier terminus data for use in machine learning applications, *The Cryosphere*, 2021, 1–41, doi:10.5194/tc-2021-311.
- Gorelick, N., M. Hancher, M. Dixon, S. Ilyushchenko, D. Thau, and R. Moore (2017), Google Earth Engine: Planetary-scale geospatial analysis for everyone, *Remote Sensing of Environment*, 202(C), 18 – 27, doi:10.1016/j.rse.2017.06.031.
- Greenwood, S. L., L. M. Simkins, M. C. M. Winsborrow, and L. R. Bjarnadttir (2021), Exceptions to bed-controlled ice sheet flow and retreat from glaciated continental margins worldwide, *Science Advances*, 7(3), eabb6291, doi:10.1126/sciadv.abb6291.
- Harrison, C., M. St-Onge, O. Petrov, S. Strelnikov, B. Lopatin, F. Wilson, S. Tella, D. Paul, T. Lynds, S. Shokalsky, C. Hulst, S. Bergman, and A. Solli (2011), Geological map of the arctic / carte gologique de l’arctique, doi: <https://doi.org/10.4095/287868>.
- Higgins, A. (1990), North Greenland Glacier Velocities and Calf Ice Production, *Polarforschung*, 1(60), 1–23.
- Hill, E., J. R. Carr, and C. R. Stokes (2017), A Review of Recent Changes in Major Marine-Terminating Outlet Glaciers in Northern Greenland, *Frontiers in Earth Science*, 4, 111, doi:10.3389/feart.2016.00111.

- Hill, E. A., J. R. Carr, C. R. Stokes, and G. H. Gudmundsson (2018), Dynamic changes in outlet glaciers in northern Greenland from 1948 to 2015, *The Cryosphere*, pp. 1 – 39, doi:10.5194/tc-2018-17.
- Holland, D. M., R. H. Thomas, B. D. Young, M. H. Ribergaard, and B. Lyberth (2008), Acceleration of Jakobshavn Isbr triggered by warm subsurface ocean waters, *Nature Geoscience*, *1*, 659 – 664, doi:10.1038/ngeo316.
- How, P., K. M. Schild, D. I. Benn, R. Noormets, N. Kirchner, A. J. Luckman, D. Vallot, N. R. J. Hulton, and C. P. Borstad (2019), Calving controlled by melt-under-cutting: detailed calving styles revealed through time-lapse observations, *Annals of Glaciology*, *60*(78), 20 – 31, doi:10.1017/aog.2018.28.
- Howat, I. M. (2018), Howat, I. 2017, updated 2018. MEaSURES Greenland Ice Mapping Project (GIMP) 2000 Image Mosaic, Version 1., *NASA National Snow and Ice Data Center Distributed Active Archive Center*, doi:10.5067/4RNTRRE4JCYD.
- Howat, I. M., and A. Eddy (2011), Multi-decadal retreat of Greenland’s marine-terminating glaciers, *Journal of Glaciology*, *57*(203), 1 – 8.
- Howat, I. M., I. R. Joughin, M. A. Fahnestock, B. E. Smith, and T. A. Scambos (2008), Synchronous retreat and acceleration of southeast Greenland outlet glaciers 200006: Ice dynamics and coupling to climate, *Journal of Glaciology*, *54*(187), 646 – 660.

- Howat, I. M., J. E. Box, Y. Ahn, A. Herrington, and E. M. McFadden (2010), Seasonal variability in the dynamics of marine-terminating outlet glaciers in Greenland, *Journal of Glaciology*, *56*(198), 601 – 613.
- Howat, I. M., A. Negrete, and B. E. Smith (2014), The Greenland Ice Mapping Project (GIMP) land classification and surface elevation data sets, *The Cryosphere*, *8*(4), 1509 – 1518, doi:10.5194/tc-8-1509-2014.
- Howat, I., S., Negrete, A. (2015), Measures greenland ice mapping project (gimp) digital elevation model, version 1, doi:https://doi.org/10.5067/NV34YUIXLP9W, dataset.
- Huttenlocher, D., G. Klanderma, and W. Rucklidge (1993), Comparing images using the Hausdorff Distance, *IEEE Transactions on Pattern Analysis and Machine Intelligence*, *15*, 850–863.
- Jackson, R. H., E. L. Shroyer, J. D. Nash, D. A. Sutherland, D. Carroll, M. J. Fried, G. A. Catania, T. C. Bartholomaus, and L. A. Stearns (2017), Nearglacier surveying of a subglacial discharge plume: Implications for plume parameterizations, *Geophysical Research Letters*, *44*, 6886 – 6894, doi:10.1002/2017gl073602.
- Jackson, R. H., J. D. Nash, C. Kienholz, D. A. Sutherland, J. M. Amundson, R. J. Motyka, D. Winters, E. Skillingstad, and E. C. Pettit (2019), Meltwater intrusions reveal mechanisms for rapid submarine melt at a tide-water glacier, *Geophysical Research Letters*, pp. 2019GL085,335 – 24, doi:10.1029/2019gl085335.

- James, T. D., T. Murray, N. Selmes, K. Scharrer, and M. O’Leary (2014), Buoyant flexure and basal crevassing in dynamic mass loss at Helheim Glacier, *Nature Geoscience*, 7(8), 593 – 596, doi:10.1038/ngeo2204.
- Jenkins, A. (2011), Convection-driven melting near the grounding lines of ice shelves and tidewater glaciers, *Journal of Physical Oceanography*, 41(12), 2279 – 2294, doi:10.1175/jpo-d-11-03.1.
- Joughin, I. R., I. M. Howat, R. B. Alley, G. Ekstrom, M. A. Fahnestock, T. Moon, M. Nettles, M. Truffer, and V. C. Tsai (2008), Ice-front variation and tidewater behavior on Helheim and Kangerdlugssuaq Glaciers, Greenland, *Journal of Geophysical Research - Earth Surface*, 113(F1), F01,004, doi:doi:10.1029/2007JF000837.
- Kehrl, L. M., I. R. Joughin, D. E. Shean, D. Floricioiu, and L. Krieger (2017), Seasonal and interannual variabilities in terminus position, glacier velocity, and surface elevation at Helheim and Kangerlussuaq Glaciers from 2008 to 2016, *Journal of Geophysical Research: Earth Surface*, 322(231), 1344 – 18, doi:10.1002/2016jf004133.
- King, M. D., I. M. Howat, S. G. Candela, M. J. Noh, S. Jeong, B. P. Y. Nol, M. R. v. d. Broeke, B. Wouters, and A. Negrete (2020), Dynamic ice loss from the Greenland Ice Sheet driven by sustained glacier retreat, *Nature Communications Earth & Environment*, 1(1), 1, doi:10.1038/s43247-020-0001-2.

- Koppes, M. N., and B. Hallet (2006), Erosion rates during rapid deglaciation in {Icy Bay, Alaska}, *Journal of Geophysical Research*, *111*(F02023), 10.1029/2005JF000,349.
- Korsgaard, N. (2021), Greenland Ice Sheet outlet glacier terminus positions 1978-1987 from aero-photogrammetric map data, *Tech. rep.*
- Korsgaard, N. J., C. Nuth, S. A. Khan, K. K. Kjellerup, A. A. Bjrk, A. Schomacker, and K. H. Kjr (2016), Digital elevation model and orthophotographs of Greenland based on aerial photographs from 19781987, *Nature Scientific Data*, *3*, 160,032 – 160,015, doi:10.1038/sdata.2016.32.
- Lea, J. M. (2018), The Google Earth Engine Digitisation Tool (GEEDiT) and the Margin change Quantification Tool (MaQiT) – simple tools for the rapid mapping and quantification of changing Earth surface margins, *Earth Surface Dynamics*, *6*(3), 551 – 561, doi:10.5194/esurf-6-551-2018.
- Lea, J. M., D. W. F. Mair, and B. R. Rea (2014), Evaluation of existing and new methods of tracking glacier terminus change, *Journal of Glaciology*, *60*(220), 323 – 332, doi:10.3189/2014jog13j061.
- Lthi, M. P., A. Vieli, L. Moreau, I. R. Joughin, M. Reisser, D. Small, and M. Stober (2016), A century of geometry and velocity evolution at Equip Sermia, West Greenland, *Journal of Glaciology*, *62*(234), 640 – 654, doi: 10.1017/jog.2016.38.

- Mankoff, K. D., W. Colgan, A. M. Solgaard, N. B. Karlsson, A. P. Ahlstrm, D. v. As, J. Box, S. A. Khan, K. K. Kjellerup, J. Mouginot, and R. S. Fausto (2019), Greenland Ice Sheet solid ice discharge from 1986 through 2017, *Earth System Science Data*, *11*, 769 – 786, doi:doi.org/10.5194/essd-11-769-2019.
- Mankoff, K. D., B. P. Y. Nol, X. Fettweis, A. P. Ahlstrm, W. Colgan, K. Kondo, K. Langley, S. Sugiyama, D. v. As, and R. S. Fausto (2020a), Greenland liquid water discharge from 1958 through 2019, *Earth System Science Data*, *12*(4), 2811 – 2841, doi:10.5194/essd-12-2811-2020.
- Mankoff, K. D., A. Solgaard, W. Colgan, A. P. Ahlstrm, S. A. Khan, and R. S. Fausto (2020b), Greenland Ice Sheet solid ice discharge from 1986 through March 2020, *Earth System Science Data*, *12*(2), 1367–1383, doi:10.5194/essd-12-1367-2020.
- Mankoff, K. D., X. Fettweis, P. L. Langen, M. Stendel, K. K. Kjledsen, N. B. Karlsson, B. Nol, M. R. v. d. Broeke, W. Colgan, S. B. Simonsen, J. E. Box, A. Solgaard, A. P. Ahlstrm, S. B. Andersen, and R. S. Fausto (2021), Greenland ice sheet mass balance from 1840 through next week, *Earth System Science Data*, doi:10.5194/essd-2021-131.
- McGrath, D., K. Steffen, I. Overeem, S. H. Mernild, B. Hasholt, and M. R. v. d. Broeke (2010), Sediment plumes as a proxy for local ice-sheet runoff in {Kangerlussuaq Fjord, West Greenland}, *Journal of Glaciology*, *56*(199), 813 – 821.

- McNabb, R. W., and R. Hock (2014), Alaska tidewater glacier terminus positions, 1948-2012, *Journal of Geophysical Research: Earth Surface*, *119*(2), 153 – 167, doi:10.1002/2013jf002915.
- Medrzycka, D., D. I. Benn, J. E. Box, L. Copeland, and J. Balog (), Calving behavior at rink isbr, west greenland, from time-lapse photos, *Arctic, Antarctic, and Alpine Research*, *48*(2), 263 – 277, doi:10.1657/aaar0015-059.
- Meier, M. F., and A. Post (1987), Fast Tidewater Glaciers, *Journal of Geophysical Research*, *92*(B9), 9051 – 9058.
- Meinshausen, M., S. J. Smith, K. Calvin, J. S. Daniel, M. L. T. Kainuma, J.-F. Lamarque, K. Matsumoto, S. A. Montzka, S. C. B. Raper, K. Riahi, A. Thomson, G. J. M. Velders, and D. P. van Vuuren (2011), The RCP greenhouse gas concentrations and their extensions from 1765 to 2300, *Climatic Change*, *109*(1), 213–241, doi:10.1007/s10584-011-0156-z.
- Millan, R., E. J. Rignot, J. Mouginot, M. H. Wood, A. A. Bjrk, and M. Morlighem (2018), Vulnerability of Southeast Greenland Glaciers to Warm Atlantic Water From Operation IceBridge and Ocean Melting Greenland Data, *Geophysical Research Letters*, *45*, 2688 – 2696, doi:10.1002/2017gl076561.
- Mohajerani, Y., M. H. Wood, I. Velicogna, and E. J. Rignot (2019), Detection of Glacier Calving Margins with Convolutional Neural Networks: A Case Study, *Remote Sensing*, *11*(1), 74 – 13, doi:10.3390/rs11010074.

- Moon, T., and I. R. Joughin (2008), Changes in ice front position on Greenland's outlet glaciers from 1992 to 2007, *Journal of Geophysical Research: Earth Surface*, *113*(F02022), doi:10.1029/2007jf000927.
- Moon, T., I. R. Joughin, B. E. Smith, M. R. v. d. Broeke, W. J. v. D. Berg, B. P. Y. Nol, and M. Usher (2014), Distinct patterns of seasonal Greenland glacier velocity, *Geophysical Research Letters*, *41*(20), 7209 – 7216, doi:10.1002/2014gl061836.
- Moon, T., I. R. Joughin, and B. E. Smith (2015), Seasonal to multiyear variability of glacier surface velocity, terminus position, and sea ice/ice mlange in northwest Greenland, *Journal of Geophysical Research: Earth Surface*, *120*(5), 818 – 833, doi:10.1002/2015jf003494.
- Moon, T., A. Gardner, B. Csatho, I. Parmuzin, and M. Fahnestock (2020), Rapid reconfiguration of the Greenland Ice Sheet coastal margin, *Journal of Geophysical Research: Earth Surface*, *in press*.
- Moon, T., M. Fisher, M. Harden, H. Simonoko, and T. Stafford (2022), QGreenland.
- Morlighem, M., E. J. Rignot, and J. Willis (2016a), Improving Bed Topography Mapping of Greenland Glaciers Using NASAs Oceans Melting Greenland (OMG) Data, *Oceanography*, *29*(4), 62 – 71, doi:10.5670/oceanog.2016.99.

- Morlighem, M., J. H. Bondzio, H. Seroussi, E. J. Rignot, E. Y. Larour, A. Humbert, and S. Rebuffi (2016b), Modeling of store gletscher's calving dynamics, west greenland, in response to ocean thermal forcing, *Geophysical Research Letters*, *43*, 2659 – 2666, doi:10.1002/2016gl067695.
- Morlighem, M., C. N. Williams, E. J. Rignot, L. An, J. E. Arndt, J. L. Bamber, G. A. Catania, N. Chauch, J. A. Dowdeswell, B. Dorschel, I. G. Fenty, K. A. Hogan, I. M. Howat, A. L. Hubbard, M. Jakobsson, T. M. Jordan, K. K. Kjellerup, R. Millan, L. A. Mayer, J. Mouginot, B. P. Y. Nol, C. O'Cofaigh, S. J. Palmer, S. Rysgaard, H. Seroussi, M. J. Siegert, P. Slabon, F. Straneo, M. R. v. d. Broeke, W. Weinrebe, M. H. Wood, and K. B. Zinglensen (2017), BedMachine v3: Complete Bed Topography and Ocean Bathymetry Mapping of Greenland From Multibeam Echo Sounding Combined With Mass Conservation, *Geophysical Research Letters*, *44*, 11,051 – 11,061, doi: 10.1002/2017gl074954.
- Motyka, R. J., L. E. Hunter, K. A. Echelmeyer, and C. Connor (2003), Submarine melting at the terminus of a temperate tidewater glacier, LeConte Glacier, Alaska, U.S.A., *Annals of Glaciology*, *36*, 57–65.
- Motyka, R. J., R. Cassotto, M. Truffer, K. K. Kjellerup, D. v. As, N. J. Korsgaard, M. A. Fahnestock, I. M. Howat, P. L. Langen, J. Mortensen, K. Lennert, and S. Rysgaard (2017), Asynchronous behavior of outlet glaciers feeding Godthbsfjord (Nuup Kangerlua) and the triggering of

- Narsap Sermia's retreat in SW Greenland, *Journal of Glaciology*, 63(238), 288 – 308, doi:10.1017/jog.2016.138.
- Mouginot, J., E. J. Rignot, A. A. Björk, M. R. v. d. Broeke, R. Millan, M. Morlighem, B. P. Y. Nol, B. Scheuchl, and M. H. Wood (2019), Forty-six years of Greenland Ice Sheet mass balance from 1972 to 2018, *Proceedings of the National Academy of Sciences*, 116(19), 9239 – 9244, doi:10.7280/d1mm37.
- Murray, T., K. Scharrer, N. Selmes, A. D. Booth, T. D. James, S. L. Bevan, J. A. Bradley, S. Cook, L. C. Llana, Y. Drocourt, L. M. Dyke, A. Goldsack, A. L. C. Hughes, A. J. Luckman, and J. McGovern (2015a), Extensive Retreat of Greenland Tidewater Glaciers, 2000–2010, *Arctic, Antarctic, and Alpine Research*, 47(3), 427 – 447, doi:10.1657/aaar0014-049.
- Murray, T., N. Selmes, T. D. James, S. Edwards, I. Martin, T. O'Farrell, R. Aspey, I. C. Rutt, M. Nettles, and T. Bauge (2015b), Dynamics of glacier calving at the ungrounded margin of Helheim Glacier, southeast Greenland, *Journal of Geophysical Research: Earth Surface*, 120, doi:10.1002/2015jf003531.
- Neteler, M., and H. Mitasova (2013), *Open source GIS: a GRASS GIS approach*, vol. 689, Springer Science & Business Media.
- Noel, B. P. Y., I. M. Howat, M. Citterio, and J. T. M. Lenaerts (2017), A tipping point in refreezing accelerates mass loss of Greenland's glaciers and ice caps, *Nature Communications*, 8(1), 875, doi:10.1038/ncomms14730.

- O’Leary, M., and P. Christoffersen (2013), Calving on tidewater glaciers amplified by submarine frontal melting, *The Cryosphere*, 7(1), 119 – 128, doi:10.5194/tc-7-119-2013.
- Pfeffer, W. T. (2007), A simple mechanism for irreversible tidewater glacier retreat, *Journal of Geophysical Research*, 112(F03S25), 119, doi:10.1029/2006jf000590.
- Porter, D. F., K. Tinto, A. Boghosian, B. M. Csatho, R. E. Bell, and J. R. Cochran (2018), Identifying Spatial Variability in Greenland’s Outlet Glacier Response to Ocean Heat, *Frontiers in Earth Science*, 6(90), doi:10.3389/feart.2018.00090.
- QGIS Development Team (2022), *QGIS Geographic Information System*, QGIS Association.
- Raup, B., A. Racoviteanu, S. J. S. Khalsa, C. Helm, R. Armstrong, and Y. Arnaud (2007), The GLIMS geospatial glacier database: A new tool for studying glacier change, *Global and Planetary Change*, 56(1-2), 101–110, doi:10.1016/j.gloplacha.2006.07.018.
- Rignot, E., Y. Xu, D. Menemenlis, J. Mouginot, B. Scheuchl, X. Li, M. Morlighem, H. Seroussi, M. v. d. Broeke, I. Fenty, C. Cai, L. An, and B. d. Fleurian (2016a), Modeling of oceaninduced ice melt rates of five west Greenland glaciers over the past two decades, *Geophysical Research Letters*, 43(12), 6374–6382, doi:10.1002/2016gl068784.

- Rignot, E. J., and J. Mouginot (2012), Ice flow in Greenland for the International Polar Year 20082009, *Geophysical Research Letters*, *39*(11), doi:10.1029/2012gl051634.
- Rignot, E. J., I. Velicogna, M. R. v. d. Broeke, A. Monaghan, and J. T. M. Lenaerts (2011), Acceleration of the contribution of the Greenland and Antarctic ice sheets to sea level rise, *Geophysical Research Letters*, *38*(5), n/a – n/a, doi:10.1029/2011gl046583.
- Rignot, E. J., I. G. Fenty, Y. Xu, C. Cai, and C. Kemp (2015), Undercutting of marinerterminating glaciers in West Greenland, *Geophysical Research Letters*, *42*(14), 5909 – 5917, doi:10.1002/2015gl064236.
- Rignot, E. J., I. G. Fenty, Y. Xu, C. Cai, I. Velicogna, C. O’Cofaigh, J. A. Dowdeswell, W. Weinrebe, G. A. Catania, and D. Duncan (2016b), Bathymetry data reveal glaciers vulnerable to ice-ocean interaction in Uummannaq and Vaigat glacial fjords, west Greenland, *Geophysical Research Letters*, *43*(6), 2667 – 2674, doi:10.1002/2016gl067832.
- Ritchie, J. B., C. S. Lingle, R. J. Motyka, and M. Truffer (2008), {Seasonal fluctuations in the advance of a tidewater glacier and potential causes: Hubbard Glacier, Alaska, USA}, *Journal of Glaciology*, *54*(186), 401 – 411.
- Robel, A. A. (2017), Thinning sea ice weakens buttressing force of icebergmange and promotes calving, *Nature Communications*, *8*(1), 14,596, doi:10.1038/ncomms14596.

- Robel, A. A., S. S. Pegler, G. Catania, D. Felikson, and L. M. Simkins (2022), Ambiguous stability of glaciers at bed peaks, *Journal of Glaciology*, pp. 1–8, doi:10.1017/jog.2022.31.
- Schenk, A. F., and B. M. Csatho (2012), A New Methodology for Detecting Ice Sheet Surface Elevation Changes From Laser Altimetry Data, *IEEE Transactions on Geoscience and Remote Sensing*, *50*(9), 3302 – 3316, doi: 10.1109/tgrs.2011.2182357.
- Schild, K. M., and G. S. Hamilton (2013), Seasonal variations of outlet glacier terminus position in Greenland, *Journal of Glaciology*, *59*(216), 759 – 770, doi:10.3189/2013jog12j238.
- Schild, K. M., C. E. Renshaw, D. I. Benn, A. Luckman, R. L. Hawley, P. How, L. Trusel, F. R. Cottier, A. Pramanik, and N. R. J. Hulton (2018), Glacier calving rates due to subglacial discharge, fjord circulation, and free convection, *Journal of Geophysical Research: Earth Surface*, *123*(9), 2189–2204, doi:10.1029/2017JF004520.
- Schoof, C. G. (2007), Ice sheet grounding line dynamics: Steady states, stability, and hysteresis, *Journal of Geophysical Research*, *112*(F3), 1720, doi: 10.1029/2006jf000664.
- Schumm, S. A. (), Patterns of alluvial rivers, *Annual Review of Earth and Planetary Sciences*, *13*(1), 5–27, doi:10.1146/annurev.ea.13.050185.000253, _eprint: <https://doi.org/10.1146/annurev.ea.13.050185.000253>.

Shepherd, A., E. R. Ivins, G. A. V. R. Barletta, M. J. Bentley, S. Bettadpur, K. H. Briggs, D. H. Bromwich, R. Forsberg, N. Galin, M. Horwath, S. Jacobs, I. Joughin, M. A. King, J. T. M. Lenaerts, J. Li, S. R. M. Ligtenberg, A. Luckman, S. B. Luthcke, M. McMillan, R. Meister, G. Milne, J. Mouginot, A. Muir, J. P. Nicolas, J. Paden, A. J. Payne, H. Pritchard, E. Rignot, H. Rott, L. S. Srensen, T. A. Scambos, B. Scheuchl, E. J. O. Schrama, B. Smith, A. V. Sundal, J. H. v. Angelen, W. J. v. d. Berg, M. R. v. d. Broeke, D. G. Vaughan, I. Velicogna, J. Wahr, P. L. Whitehouse, D. J. Wingham, D. Yi, D. Young, and H. J. Zwally (), A reconciled estimate of ice-sheet mass balance, *Science*, *338*(6111), 1183–1189, doi:10.1126/science.1228102, publisher: American Association for the Advancement of Science Section: Research Article.

Shreve, R. L. (1972), Movement of Water in Glaciers, *Journal of Glaciology*, *11*(62), 205 – 214.

Slater, D. A., P. W. Nienow, D. N. Goldberg, T. R. Cowton, and A. J. Sole (2017), A model for tidewater glacier undercutting by submarine melting, *Geophysical Research Letters*, *380*(3-4), doi:10.1002/2016gl072374.

Slater, D. A., F. Straneo, S. B. Das, C. G. Richards, T. J. W. Wagner, and P. W. Nienow (2018), Localized Plumes Drive FrontWide Ocean Melting of A Greenlandic Tidewater Glacier, *Geophysical Research Letters*, *45*, 12,350 – 12,358, doi:10.1029/2018gl080763.

- Slater, D. A., F. Straneo, D. Felikson, C. M. Little, H. Goelzer, X. Fettweis, and J. Holte (2019), Estimating Greenland tidewater glacier retreat driven by submarine melting, *The Cryosphere*, *13*(9), 2489 – 2509, doi:10.5194/tc-13-2489-2019.
- Slater, D. A., D. Carroll, H. Oliver, M. J. Hopwood, F. Straneo, M. Wood, J. K. Willis, and M. Morlighem (2022), Characteristic depths, fluxes and timescales for greenland’s tidewater glacier fjords from subglacial discharge-driven upwelling during summer, *Geophysical Research Letters*, *n/a*, e2021GL097,081, doi:10.1029/2021GL097081, _eprint: <https://onlinelibrary.wiley.com/doi/pdf/10.1029/2021GL097081>.
- Smith, L. C., V. W. Chu, K. Yang, C. J. Gleason, L. H. Pitcher, A. K. Rennermalm, C. J. Legleiter, A. E. Behar, B. T. Overstreet, S. E. Moustafa, M. Tedesco, R. R. Forster, A. L. LeWinter, D. C. Finnegan, Y. Sheng, and J. Balog (2015), Efficient meltwater drainage through supraglacial streams and rivers on the southwest Greenland ice sheet, *Proceedings of the National Academy of Sciences*, *112*(4), 1001 – 1006, doi:10.1073/pnas.1413024112.
- Straneo, F., and C. Cenedese (2015), The Dynamics of Greenland’s Glacial Fjords and Their Role in Climate, *Annual Review of Marine Sciences*, *7*(1), 89 – 112, doi:10.1146/annurev-marine-010213-135133.
- Straneo, F., and P. Heimbach (2013), North Atlantic warming and the retreat of Greenland’s outlet glaciers, *Nature Communications*, *504*(7478), 36 – 43, doi:10.1038/nature12854.

- Straneo, F., G. S. Hamilton, D. A. Sutherland, L. A. Stearns, F. J. M. Davidson, M. O. Hammill, G. B. Stenson, and A. Rosing-Asvid (2010), Rapid circulation of warm subtropical waters in a major glacial fjord in East Greenland, *Nature Geoscience*, *3*, 182 – 186, doi:10.1038/ngeo764.
- Sutherland, D. A., R. H. Jackson, C. Kienholz, J. M. Amundson, W. P. Dryer, D. Duncan, E. F. Eidam, R. J. Motyka, and J. D. Nash (2019), Direct observations of submarine melt and subsurface geometry at a tidewater glacier, *Science*, *365*(6451), 369 – 374, doi:10.1126/science.aax3528.
- Tedstone, A. J., and N. S. Arnold (2012), Automated remote sensing of sediment plumes for identification of runoff from the greenland ice sheet, *Journal of Glaciology*, *58*(210), 699–712, doi:10.3189/2012JoG11J204.
- Todd, J., P. Christoffersen, T. Zwinger, P. Rback, N. Chauch, D. I. Benn, A. J. Luckman, J. C. Ryan, N. Toberg, D. A. Slater, and A. L. Hubbard (2018), A Full-Stokes 3-D Calving Model Applied to a Large Greenlandic Glacier, *Journal of Geophysical Research: Earth Surface*, *308*(5906), 1 – 23, doi:10.1002/2017jf004349.
- van der Veen, C. (1996), Calving glaciers, *Journal of Glaciology*, *42*(141), 375–385, doi:https://doi.org/10.1191/0309133302pp327ra.
- van Dongen, E. C. H., G. Jouviet, S. Sugiyama, E. A. Podolskiy, M. Funk, D. I. Benn, F. Lindner, A. Bauder, J. Seguinot, S. Leinss, and F. Walter (2021), Thinning leads to calving-style changes at bowdoin glacier, greenland, *The Cryosphere*, *15*(2), 485–500, doi:10.5194/tc-15-485-2021.

Virtanen, P., R. Gommers, T. E. Oliphant, M. Haberland, T. Reddy, D. Cournapeau, E. Burovski, P. Peterson, W. Weckesser, J. Bright, S. J. van der Walt, M. Brett, J. Wilson, K. J. Millman, N. Mayorov, A. R. J. Nelson, E. Jones, R. Kern, E. Larson, C. J. Carey, . Polat, Y. Feng, E. W. Moore, J. VanderPlas, D. Laxalde, J. Perktold, R. Cimrman, I. Henriksen, E. A. Quintero, C. R. Harris, A. M. Archibald, A. H. Ribeiro, F. Pedregosa, and P. van Mulbregt (2020), SciPy 1.0: fundamental algorithms for scientific computing in python, *Nature Methods*, *17*(3), 261–272, doi:10.1038/s41592-019-0686-2, number: 3 Publisher: Nature Publishing Group.

Wagner, T. J. W., T. D. James, T. Murray, and D. Vella (), On the role of buoyant flexure in glacier calving, *Geophysical Research Letters*, *43*(1), 232–240A, doi:10.1002/2015GL067247.

Walter, J. I., J. E. Box, S. M. Tulaczyk, E. E. Brodsky, I. M. Howat, Y. Ahn, and A. A. Brown (2012), Oceanic mechanical forcing of a marine-terminating Greenland glacier, *Annals of Glaciology*, *53*(60), 181 – 192, doi:10.3189/2012aog60a083.

Warren, C. R. (1991), Terminal environment, topographic control and fluctuations of West Greenland glaciers, *Boreas*, *20*(1), 1 – 15, doi:10.1111/j.1502-3885.1991.tb00453.x.

Warren, C. R., and N. F. Glasser (1992), Contrasting Response of South

- Greenland Glaciers to Recent Climatic Change, *Arctic and Alpine Research*, 24(2), 124 – 132.
- Weertman, J. (1974), Stability of the junction of an ice sheet and an ice shelf, *Journal of Glaciology*, 13(67), 3 – 11.
- Weidick, A. (1958), Frontal Variations at Upernaviks Isstrom in the Last 100 Years, *Medd. fra Dansk Geol. Forening*, (14), 52–60.
- Williams, J. J., N. Gourmelen, P. Nienow, C. Bunce, and D. Slater (2021), Helheim glacier poised for dramatic retreat, *Geophysical Research Letters*, 48(23), e2021GL094,546, doi:10.1029/2021GL094546.
- Winkelmann, D., W. Jokat, L. Jensen, and H.-W. Schenke (2010), Submarine end moraines on the continental shelf off NE greenland implications for lateglacial dynamics, *Quaternary Science Reviews*, 29(9), 1069–1077, doi: 10.1016/j.quascirev.2010.02.002.
- Wood, M., E. Rignot, I. Fenty, L. An, A. Bjrck, M. v. d. Broeke, C. Cai, E. Kane, D. Menemenlis, R. Millan, M. Morlighem, J. Mouginot, B. Nol, B. Scheuchl, I. Velicogna, J. K. Willis, and H. Zhang (2021a), Ocean forcing drives glacier retreat in Greenland, *Science Advances*, 7(1), eaba7282, doi: 10.1126/sciadv.aba7282.
- Wood, M. H., E. J. Rignot, I. G. Fenty, L. An, A. Bjrck, M. R. v. d. Broeke, C. Cai, E. Kane, D. Menemenlis, R. Millan, M. Morlighem, J. Mouginot, B. P. Y. Nol, B. Scheuchl, I. Velicogna, J. K. Willis, and H. Zhang (2021b),

- Ocean forcing drives glacier retreat in Greenland., *Science Advances*, 7(1), doi:10.1126/sciadv.aba7282.
- Wulder, M. A., J. C. White, T. R. Loveland, C. E. Woodcock, A. S. Belward, W. B. Cohen, E. A. Fosnight, J. Shaw, J. G. Masek, and D. P. Roy (2016), The global Landsat archive: Status, consolidation, and direction, *Remote Sensing of Environment*, 185, 271–283, doi:10.1016/j.rse.2015.11.032.
- Xu, Y., E. J. Rignot, I. G. Fenty, D. Menemenlis, and M. M. Flexas (2013-08), Subaqueous melting of Store Glacier, West Greenland from three-dimensional, high-resolution numerical modeling and ocean observations, *Geophysical Research Letters*, 40(1-6), doi:10.1002/grl.50825.
- Zevenbergen, L. W., and C. R. Thorne (1987), Quantitative analysis of land surface topography, *Earth Surface Processes and Landforms*, 12(1), 47–56, doi:10.1002/esp.3290120107, eprint: <https://onlinelibrary.wiley.com/doi/pdf/10.1002/esp.3290120107>.
- Zhang, E., L. Liu, and L. Huang (2019), Automatically delineating the calving front of Jakobshavn Isbr from multitemporal TerraSAR-X images: a deep learning approach, *The Cryosphere*, 13(6), 1729 – 1741, doi: 10.5194/tc-13-1729-2019.
- Zhang, E., L. Liu, L. Huang, and K. S. Ng (2021), An automated, generalized, deep-learning-based method for delineating the calving fronts of Greenland glaciers from multi-sensor remote sensing imagery, *Remote Sensing of Environment*, 254, 112,265, doi:10.1016/j.rse.2020.112265.

Vita

Sophie Goliber received a B.S. in Geology from the University of Buffalo in Buffalo, NY, before coming to the University of Texas at Austin to pursue her PhD. She is continuing as a postdoctoral researcher at the University of Buffalo in Buffalo, NY. Contact information can be found on her website: sophieice.com

Permanent address: Institute for Geophysics, J.J. Pickle Research
Campus, Bldg. 196 10100 Burnet Road (R2200)
Austin, TX 78758-4445

This dissertation was typeset with \LaTeX^\dagger by the author.

[†] \LaTeX is a document preparation system developed by Leslie Lamport as a special version of Donald Knuth's \TeX Program.